# Semiconductor Mode-Locked Lasers: Modeling, Characterization and Applications

Thesis by

Roger Gérard Matthias Paul Koumans

In Partial Fulfillment of the Requirements

for the Degree of

Doctor of Philosophy


California Institute of Technology

Pasadena, California

2001

(Defended December 19, 2000)

*To my parents*

*(Bedankt pap en mam)*

# Acknowledgements

First and out-most, I would like to express my gratitude to my advisor Prof. Amnon Yariv for giving me the opportunity to study in his group surrounded by an extremely large amount of resources and support. I have gained a lot of knowledge and experience in the optics area during my challenging years at Caltech. I remain very grateful to him and Caltech for providing me with financial support, without which it would have been impossible for me to pursue my graduate studies at one of the best and most renown schools in the country.

I would further like to thank Prof. Yaakov Shevy for the encouragement and motivation he has given me during the last year towards the completion of my studies. I also owe many thanks to Prof. Kerry Vahala for making his laboratory and time available to me. He has proven to be an excellent teacher and a valuable source of information.

In addition I would like to show my appreciation to the current and previous group members who have supported me during my study here, especially my colleagues Dan Provenzano and George Paloczi with whom I still have many valuable interactions and with whom I have become close friends.

I would like to express my thanks to Randal Salvatore for his scientific and social help during my first few months and who got me started in the laboratory and to Reginald Lee, Bill Marshall and Danny Eliyahu for the many fruitful discussions we have had. I also want to acknowledge Ashish Bhardwaj for his help and assistance in a number of experiments.

I would like to thank the staff members of our group who have provided me with technical assistance: Ali Ghaffari, Larry Begay, T.R. Chen and Kevin Cooper. Special

thanks go to the late Jana Mercado, Connie Rodriguez and Linda Dozsa who have always shown their caring side.

I would also like to express my appreciation to Al Preston and James Gleeson for being my roommates throughout my years at Caltech and for making my time at home an enjoyable one.

And most importantly, I will always appreciate the continuous support, encouragement and love that my parents, my beloved twin sister and my brother have given me throughout my life. Thanks for being there for me.

# Abstract

This thesis describes the modeling and characterization of mode-locked semiconductor lasers. An enhanced dynamic model is developed to describe the startup and steady-state behavior of mode-locked lasers. Two new applications for mode-locked lasers are given and their potential is discussed. A new technique to characterize the optical pulses emitted from a mode-locked laser is analyzed and demonstrated.

A combined time and frequency-domain dynamic model is introduced for semiconductor mode-locked lasers. The model includes both linear mode-coupling effects through carrier density modulation at harmonics of the mode-spacing as well as nonlinear effects like gain saturation and additional mode-coupling through four wave mixing. The model is used to study the behavior of a 2 mm long mode-locked semiconductor laser with a gain section of 1900 $\mu$m and an absorber section of 100 $\mu$m. Without the inclusion of spontaneous emission, steady state mode-locking is achieved after a few tens of nanoseconds producing chirped picosecond pulses. The inclusion of spontaneous emission disturbs the steady state mode-locking solution into a quasi-steady state which causes timing and amplitude jitter of the pulse train.

The potential of a semiconductor mode-locked laser with a dense mode spacing ($\sim$ 25 GHz) as an optical source for wavelength division multiplexing is studied. One of the locked modes is filtered out by a narrow band fiber Bragg grating and its use as a single wavelength source is examined. The bit error rate (BER) performance of the source is measured but no "error free" transmission is achieved due to mode competition noise. The laser is next used in an external feedback configuration where the feedback is provided by a fiber Bragg grating. Lasing only occurs when the fiber Bragg grating is tuned to one of the monolithic cavity modes leading to a discretely

tunable single wavelength source whose channel spacing is determined by the mode spacing of the semiconductor laser. Single mode operation of the laser with more than 40 dB side mode suppression is obtained. The BER performance of several channels is examined by stretching the fiber Bragg grating. "Error free" performance is obtained for all channels.

As another new application, the use of semiconductor mode-locked lasers in a photonic analog to digital (A/D) converter is proposed. The method uses wavelength multiplicity to increase the sampling rate of A/D converters. The optical output of a number of semiconductor lasers each mode-locked at a different center wavelength is spectrally stitched and time-interleaved into a high repetition rate multi-wavelength sampling pulse train (MW-SPT) which can be used in a photonic A/D converter to sample a high-end microwave signal. The amplitude modulated high repetition rate MW-SPT is next wavelength demultiplexed into parallel pulse streams with a lower sampling rate which can be processed by conventional electronic state-of-the-art A/D converters in a parallel fashion.

Finally, a new method for the characterization of ultrashort pulses called time resolved optical gating based on dispersive propagation (DP-TROG) is introduced and demonstrated. The DP-TROG technique is a new non-interferometric method for characterizing ultra-short optical pulses in amplitude and phase without the need for a short optical gating pulse. An algorithm is developed for the reconstruction of the pulse amplitude and phase from the measurements. The pulse train emitted from a mode-locked semiconductor laser at $1.5\mu$m is characterized using this new technique and excellent pulse retrieval is achieved.

# Contents

# List of Figures

# List of Tables

# CHAPTER 1

# *Introduction to the thesis*

## 1.1 Historical background

The technique of laser mode-locking has been around for more than 35 years. The first mode-locking was demonstrated in 1964 [1] and has since then developed into a very active research area. Mode-locking theory was first described by DiDomenico [2] and by Yariv [3]. In a mode-locked laser many equally-spaced longitudinal modes oscillate simultaneously. Their phases are locked to each other by an intra-cavity gain, loss or phase element resulting in an ultra-short pulsed optical output. A recent simplified but very intuitive description and explanation of the process of mode-locking is given in [4]. Over the years many models have emerged to explain the mode-locking process varying from time-domain [5, 6] and frequency-domain models [7] to traveling wave [8] and transmission line models [9]. This work develops an enhanced combined time and frequency-domain model [10, 11] for semiconductor mode-locked which can describe the mode-locking process in detail.

There are various ways to achieve mode-locking in semiconductor lasers. In active mode-locking, the gain section of the laser is modulated with electrical pulses that have a repetition period equal to the round-trip time of an optical pulse in the laser cavity. Only during the peak of the electrical pulse, the gain section provides enough gain to overcome the losses in the cavity. During this short period of positive net gain, an optical pulse will be generated. Short optical pulses have been generated at various repetition rates with different pulse durations [12–15]. Passive mode-locking provides an alternative approach to generating ultra-short pulses which is more easily achieved

than active mode-locking as it needs no electrical pulses to mode-lock the laser. This type of mode-locking is, however, more difficult to control, particularly if one wishes to obtain stable and reliable mode-locked operation [16, 17]. Passive mode-locking techniques are used in many laser systems to generate short optical pulses. The key component necessary for passive mode-locking is a saturable absorber, which locks the longitudinal cavity modes in phase, leading to a short optical pulse [18, 19]. In contrast to active mode-locking, passive mode-locking provides no synchronization between the generated optical pulses and electrical signals but mode-locking at ultra-high repetition rates can be achieved [20]. Hybrid mode-locking combines the advantages of passive mode-locking together with the electrical synchronization of the optical pulses in active mode-locking [21–23]. Note that for active and hybrid mode-locking electrical restrictions remain present.

Mode-locked lasers are now used in many science areas. Most importantly of course in the optical communications field but they are also widely used in other fields like femtosecond chemistry, high speed photonics, solid-state physics and spectroscopy [24]. Some applications use the frequency-domain properties of a mode-locked laser, i.e., they make use of the fact that a mode-locked laser emits multiple equally spaced oscillating modes [25, 26]. Most other applications use the time-domain properties of the laser [27], i.e., the fact that it emits an optical pulse train.

For most time-domain applications it is important that the optical pulses can be characterized in amplitude and phase. Characterization methods have been developed for this purpose over the course of years as well. Most of the early methods are limited. They assume a certain pulse shape in order to give an estimate for the pulse duration. These methods do not provide any insight in the phase characteristics of the pulse. As a rising need for these phase characteristics has occurred in over the years, especially in today's age of optical fiber communication, a steep increase in pulse characterization methods has been noticed over the last decade. All of these newly developed methods are able to fully characterize the optical pulse in amplitude and phase by combining measurements of both time-domain and frequency-domain properties of the pulse [28, 29].

## 1.2 Thesis outline

This thesis describes the modeling and characterization of semiconductor mode-locked lasers. In addition a number of new applications for mode-locked lasers and their potential in the field of optical communications and the photonics area is discussed as well.

In Chapter 2 a multi-mode semiconductor laser model is introduced that covers both the dynamic as well as the spectral properties of a semiconductor laser. The first half of Chapter 2 analyzes the spectral dependence of the complex susceptibility. The dependence of the susceptibility on frequency and carrier density is calculated and both the linear and nonlinear part of the susceptibility is considered. The second half of Chapter 2 develops a dynamic multi-mode laser model. This model combines both a time and frequency-domain approach. The dynamic properties of the model express themselves through a set of coupled time-dependent mode equations which describe how the amplitude and phase of each mode develop in time. The spectral properties enter the picture through the spectral dependence of the complex susceptibility which is present in each of the modal rate equations. The linear susceptibility provides both linear gain and index change for each mode but can also provide mode coupling through carrier modulation caused by the beating of modes or by modulation of the injection current. The nonlinear susceptibility causes saturation of the linear gain and index and also causes nonlinear gain and index change due to four wave mixing (FWM). This FWM process provides additional coupling between the oscillating modes. The complete dynamic model is applied to a semiconductor mode-locked laser and the startup and steady-state behavior is analyzed. Chapter 2 concludes with the inclusion of spontaneous emission into each mode equation, and the influence of spontaneous emission on the mode-locking process is studied.

Chapter 3 discusses two new applications of mode-locked lasers. The first half covers a new frequency-domain application and studies the potential of a mode-locked laser as an optical source for wavelength division multiplexing (WDM). The second half of Chapter 3 discusses a new time-domain application for mode-locked lasers.

A theoretical scheme is introduced for a photonic analog to digital (A/D) converter utilizing a multi-wavelength sampling pulse train (MW-SPT) generated by a number of mode-locked lasers and an optical modulator that is driven by the microwave signal to be digitized. This scheme is able to enhance the maximum achievable sampling rate in an A/D converter from the low gigahertz range to the high gigahertz range so that it becomes possible to sample microwave signals. The potential of this application and its advantages compared with other photonic A/D converter technologies are discussed. Recommendations are given for pulse properties like pulse width, pulse spacing and methods for pulse synchronization and equalization.

The second part of this thesis specializes in the area of characterization of ultrashort optical pulses emitted by mode-locked lasers. Chapter 4 reviews a number of basic and commonly used measurement setups for characterizing optical pulses. The basic principles of the recently introduced method of frequency resolved optical gating (FROG) are discussed in detail as this method has been the inspiration for the development of its time-domain counterpart time resolved optical gating (TROG) which is introduced in the first half of Chapter 5. A new measurement setup for TROG based on dispersive propagation (DP-TROG) is next introduced and theoretically analyzed. An algorithm is developed to reconstruct the pulse amplitude and phase from the measurements taken. Chapter 6 concludes with the experimental demonstration of the DP-TROG technique and characterizes a picosecond optical pulse train emitted from a mode-locked semiconductor laser. General guidelines for the measurement are provided. The pulse reconstruction process is applied and noise reduction techniques for additive measurement noise are discussed.

## References

[1] L. Hargrove, R. Fork, and M. Pollack, "Locking of He-Ne laser modes induced by synchronous intracavity modulation," *Appl. Phys. Lett.*, vol. 5, no. 1, pp. 4–5, 1964.

[2] M. DiDomenico, "Small-signal analysis of internal (coupling-type) modulation of lasers," *J. Appl. Phys.*, vol. 35, no. 10, pp. 2870–2876, 1964.

[3] A. Yariv, "Internal modulation in multimode laser oscillators," *J. Appl. Phys.*, vol. 36, no. 2, pp. 388–391, 1965.

[4] J. Hopkins and W. Sibbett, "Ultrashort-pulse lasers: big payoffs in a flash," *Scientific American*, Sept. 2000.

[5] H. Haus, "Theory of mode locking with a slow saturable absorber," *IEEE J. Quantum Electron.*, vol. 11, pp. 736–746, Sept. 1975.

[6] H. Haus, "Modelocking of semiconductor laser diodes," *Jap. J. Appl. Phys.*, vol. 20, pp. 1007–1020, June 1981.

[7] H. Haus, "A theory of forced mode locking," *IEEE J. Quantum Electron.*, vol. 11, pp. 323–330, July 1975.

[8] D. Jones, L. Zhang, J. Carroll, and D. Marcenac, "Dynamics of monolithic passively mode-locked semiconductor-lasers," *IEEE J. Quantum Electron.*, vol. 31, no. 6, pp. 1051–1058, 1995.

[9] A. Lowery and I. Marshall, "Numerical simulations of 1.5 $\mu$m actively mode-locked semiconductor-lasers including dispersive elements and chirp," *IEEE J. Quantum Electron.*, vol. 27, no. 8, pp. 1981–1989, 1991.

[10] K. Lau, "Narrow-band modulation of semiconductor-lasers at millimeter wave frequencies ($>$ 100 GHz) by mode-locking," *IEEE J. Quantum Electron.*, vol. 26, no. 2, pp. 250–261, 1990.

[11] R. Salvatore, S. Sanders, T. Schrans, and A. Yariv, "Supermodes of high-repetition-rate passively mode- locked semiconductor lasers," *IEEE J. Quantum Electron.*, vol. 32, no. 6, pp. 941–952, 1996.

[12] J. Bowers, P. Morton, A. Mar, and S. Corzine, "Actively mode-locked semiconductor-lasers," *IEEE J. Quantum Electron.*, vol. 25, no. 6, pp. 1426–1439, 1989.

[13] M. Schell, A. Weber, E. Scholl, and D. Bimberg, "Fundamental limits of sub-ps pulse generation by active-mode locking of semiconductor-lasers - the spectral gain width and the facet reflectivities," *IEEE J. Quantum Electron.*, vol. 27, no. 6, pp. 1661–1668, 1991.

[14] J. Werner, H. Melchior, and G. Guekos, "Stable optical picosecond pulses from actively mode-locked twin-section diode-lasers," *Electron. Lett.*, vol. 24, no. 3, pp. 140–141, 1988.

[15] P. Hansen, G. Raybon, U. Koren, B. Miller, M. Young, M. Newkirk, M. Chien, B. Tell, and C. Burrus, "2-cm long monolithic multisection laser for active mode-locking at 2.2 GHZ," *Electron. Lett.*, vol. 29, no. 9, pp. 739–741, 1993.

[16] D. Eliyahu, R. Salvatore, and A. Yariv, "Effect of noise on the power spectrum of passively mode-locked lasers," *J. Opt. Soc. Amer. B*, vol. 14, no. 1, pp. 167–174, 1997.

[17] D. Eliyahu, R. Salvatore, and A. Yariv, "Noise characterization of a pulse train generated by actively mode-locked lasers," *J. Opt. Soc. Amer. B*, vol. 13, no. 7, pp. 1619–1626, 1996.

[18] S. Arahire, Y. Matsui, T. Kunii, S. Oshiba, and Y. Ogawa, "Optical short-pulse generation at high-repetition- rate over 80 GHZ from a monolithic passively modelocked DBR laser-diode," *Electron. Lett.*, vol. 29, no. 11, pp. 1013–1015, 1993.

[19] J. Hohimer and G. Vawter, "Passive-mode locking of monolithic semiconductor ring lasers at 86 GHZ," *Appl. Phys. Lett.*, vol. 63, no. 12, pp. 1598–1600, 1993.

[20] R. Salvatore, *Ultrashort and ultra-high repetition rate pulses from passively mode-locked semiconductor lasers.* PhD thesis, California Institute of Technology, 1996.

[21] P. Hansen, G. Raybon, U. Koren, P. Iannone, B. Miller, G. Young, M. Newkirk, and C. Burrus, "InGAAsP monolithic extended-cavity lasers with integrated saturable absorbers for active, passive, and hybrid mode-locking at 8.6 GHZ," *Appl. Phys. Lett.*, vol. 62, no. 13, pp. 1445–1447, 1993.

[22] A. Weber, M. Schell, G. Fischbeck, and D. Bimberg, "Generation of single femtosecond pulses by hybrid mode-locking of a semiconductor-laser," *IEEE J. Quantum Electron.*, vol. 28, no. 10, pp. 2220–2229, 1992.

[23] D. Derickson, R. Helkey, A. Mar, J. Karin, J. Bowers, and R. Thornton, "Suppression of multiple pulse formation in external-cavity mode-locked semiconductor-lasers using intrawaveguide saturable absorbers," *IEEE Photon. Technol. Lett.*, vol. 4, no. 4, pp. 333–335, 1992.

[24] W. Kaiser, ed., *Ultrashort laser pulses and applications.* Springer-Verlag, 1988.

[25] D. Eliyahu, A. Yariv, and R. Salvatore, "Broader, flatter optical spectra of passively mode- locked semiconductor lasers for a wavelength- division multiplexing source," *Appl. Opt.*, vol. 36, no. 15, pp. 3430–3434, 1997.

[26] H. Sanjoh, H. Yasaka, Y. Sakai, K. Sato, H. Ishii, and Y. Yoshikuni, "Multiwavelength light source with precise frequency spacing using a mode-locked semiconductor laser and an arrayed waveguide grating filter," *IEEE Photon. Technol. Lett.*, vol. 9, no. 6, pp. 818–820, 1997.

[27] A. Yariv and R. Koumans, "Time interleaved optical sampling for ultrahigh speed A/D conversion," *Electron. Lett.*, vol. 34, no. 21, pp. 2012–2013, 1998.

[28] R. Trebino, K. DeLong, D. Fittinghoff, J. Sweetser, M. Krumbugel, B. Richman, and D. Kane, "Measuring ultrashort laser pulses in the time-frequency domain using frequency-resolved optical gating," *Rev. Scientific Instruments*, vol. 68, no. 9, pp. 3277–3295, 1997.

[29] R. Koumans and A. Yariv, "Time-resolved optical gating based on dispersive propagation: A new method to characterize optical pulses," *IEEE J. Quantum Electron.*, vol. 36, no. 2, pp. 137–144, 2000.

# CHAPTER 2

# *A dynamic multi-mode semiconductor laser model*

## 2.1 Introduction

In this chapter we develop a multi-mode laser model which can be used to calculate the transient dynamic behavior of multi-mode semiconductor lasers like Fabry-Pérot (FP) lasers and mode-locked lasers. The model considers a number of longitudinal cavity modes and calculates their time-dependence by simultaneously integrating a set of modal rate equations and carrier density equations. Each modal rate equation is driven by a complex polarization term which takes into account both linear and non-linear effects of the laser medium. Linear effects include both linear gain and linear index changes in the medium and non-linear effects include mode-coupling through carrier modulation, self and cross-gain saturation and mode coupling through four wave mixing. The mode-competition and phase locking process during start-up is analyzed and the effects of spontaneous emission on the dynamic and steady-state behavior of the laser are investigated.

## 2.2 Complex susceptibility of a semiconductor laser material

### *2.2.1 Linear part of the complex susceptibility*

In order to calculate the linear gain in the semiconductor laser material it is necessary to find an expression for the complex linear susceptibility of the semiconductor material. In this chapter we consider an InGaAsP semiconductor bulk material at

an emission wavelength of 1.5$\mu$m with a complex Lorentzian lineshape. We assume a three band model consisting of one conduction band and two valence bands (heavy and light holes). The bands are assumed to be parabolic. Two different transitions can occur in the semiconductor: a transition from the conduction band to the heavy hole band, indicated by c→hh, and a transition from the conduction band to the light hole band, indicated by c→lh. Using the density-matrix formalism [1] we can calculate the linear part of the complex susceptibility of the semiconductor material. The linear susceptibility $\chi^{\mathrm{L}}(\mathcal{E}_m, N)$ for a longitudinal mode $m$ induced at an optical energy $\mathcal{E}_m$ for a given carrier density $N$ is given by

$$\chi_m^{\mathrm{L}} \equiv \chi^{\mathrm{L}}(\mathcal{E}_m, N) = \frac{1}{2\pi^2 \varepsilon_0 \hbar} \int_{\mathcal{E}_g}^{\infty} \frac{f(\mathcal{E}, N)}{(\mathcal{E}_m - \mathcal{E})/\hbar - i/T_2} \, \mathrm{d}\mathcal{E} \tag{2.1}$$

where $\mathcal{E}_g$ is the bandgap of the semiconductor material, $T_2$ is the polarization relaxation time and $f(\mathcal{E}, N)$ is defined as

$$\begin{aligned} f(\mathcal{E}, N) = \mathcal{M}^{\mathrm{c}\to\mathrm{hh}} \left\{ \mathcal{F}_{\mathrm{c}}^{\mathrm{c}\to\mathrm{hh}}(\mathcal{E}, N) - \mathcal{F}_{\mathrm{v}}^{\mathrm{c}\to\mathrm{hh}}(\mathcal{E}, N) \right\} \sqrt{(\mathcal{E} - \mathcal{E}_g)/\hbar} \\ + \mathcal{M}^{\mathrm{c}\to\mathrm{lh}} \left\{ \mathcal{F}_{\mathrm{c}}^{\mathrm{c}\to\mathrm{lh}}(\mathcal{E}, N) - \mathcal{F}_{\mathrm{v}}^{\mathrm{c}\to\mathrm{lh}}(\mathcal{E}, N) \right\} \sqrt{(\mathcal{E} - \mathcal{E}_g)/\hbar} \end{aligned} \tag{2.2}$$

Here $\mathcal{M}$ is the transition matrix element and $\mathcal{F}_{\mathrm{c}}$ and $\mathcal{F}_{\mathrm{v}}$ are the Fermi functions for the conduction and valence band respectively for a certain transition. The Fermi-levels are calculated from the quasi-equilibrium of the carriers in the semiconductor material. The transition matrix elements are given by

$$\mathcal{M}^{\mathrm{c}\to\mathrm{hh}} = \left( \frac{2m_r^{\mathrm{c}\to\mathrm{hh}}}{\hbar^2} \right)^{3/2} |\mu^{\mathrm{c}\to\mathrm{hh}}|^2 \tag{2.3a}$$

$$\mathcal{M}^{\mathrm{c}\to\mathrm{lh}} = \left( \frac{2m_r^{\mathrm{c}\to\mathrm{lh}}}{\hbar^2} \right)^{3/2} |\mu^{\mathrm{c}\to\mathrm{lh}}|^2 \tag{2.3b}$$

where $m_r$ is the reduced mass and $\mu$ is the dipole matrix element for a certain transition (c→hh or c→lh). The reduced masses for each transition are given by

$$\frac{1}{m_r^{\mathrm{c}\to\mathrm{hh}}} = \frac{1}{m_c} + \frac{1}{m_{hh}} \tag{2.4a}$$

$$\frac{1}{m_r^{\mathrm{c}\to\mathrm{lh}}} = \frac{1}{m_c} + \frac{1}{m_{lh}} \tag{2.4b}$$

The linear gain $g_m^{\mathrm{L}}$ and refractive index change $\Delta n_m^{\mathrm{L}}/n_0$ for a mode $m$ with energy $\mathcal{E}_m$ can be calculated from the susceptibility through the following relations:

$$\begin{aligned} g_m^{\mathrm{L}} &\equiv g^{\mathrm{L}}(\mathcal{E}_m, N) \\ &= \frac{\mathcal{E}_m}{\hbar}\,\frac{\chi_m^{\mathrm{L},I}}{n_0^2} \\ &= \frac{\mathcal{E}_m}{2\pi^2\varepsilon_0 n_0^2\hbar^2}\int_{\mathcal{E}_g}^{\infty}\frac{1/T_2}{(\mathcal{E}_m-\mathcal{E})^2/\hbar^2+1/T_2^2}f(\mathcal{E},N)\,\mathrm{d}\mathcal{E} \end{aligned} \tag{2.5a}$$

$$\begin{aligned} \frac{\Delta n_m^{\mathrm{L}}}{n_0} &\equiv \frac{\Delta n_m^{\mathrm{L}}(\mathcal{E}_m, N)}{n_0} \\ &= \frac{\chi_m^{\mathrm{L},R}}{2n_0^2} \\ &= \frac{1}{4\pi^2\varepsilon_0 n_0^2\hbar^2}\int_{\mathcal{E}_g}^{\infty}\frac{\mathcal{E}_m-\mathcal{E}}{(\mathcal{E}_m-\mathcal{E})^2/\hbar^2+1/T_2^2}f'(\mathcal{E},N)\,\mathrm{d}\mathcal{E} \end{aligned} \tag{2.5b}$$

where $\chi_m^{\mathrm{L},R}$ and $\chi_m^{\mathrm{L},I}$ indicate the real and imaginary part of the linear susceptibility respectively. It is noted that in order to calculate the linear refractive index change, the function $f(\mathcal{E}, N)$ has been replaced by $f'(\mathcal{E}, N)$ defined by

$$\begin{aligned} f'(\mathcal{E},N) = {} & \mathcal{M}^{\mathrm{c}\to\mathrm{hh}}\left\{\mathcal{F}_{\mathrm{c}}^{\mathrm{c}\to\mathrm{hh}}(\mathcal{E},N)-\mathcal{F}_{\mathrm{v}}^{\mathrm{c}\to\mathrm{hh}}(\mathcal{E},N)+1\right\}\sqrt{(\mathcal{E}-\mathcal{E}_g)/\hbar} \\ & + \mathcal{M}^{\mathrm{c}\to\mathrm{lh}}\left\{\mathcal{F}_{\mathrm{c}}^{\mathrm{c}\to\mathrm{lh}}(\mathcal{E},N)-\mathcal{F}_{\mathrm{v}}^{\mathrm{c}\to\mathrm{lh}}(\mathcal{E},N)+1\right\}\sqrt{(\mathcal{E}-\mathcal{E}_g)/\hbar} \end{aligned} \tag{2.6}$$

The factor $\mathcal{F}_{\mathrm{c}} - \mathcal{F}_{\mathrm{v}} + 1$ in (2.6) instead of $\mathcal{F}_{\mathrm{c}} - \mathcal{F}_{\mathrm{v}}$ in (2.2) avoids the problem that the integral does not converge due to the simple Lorentzian lineshape and due to the limitations of the assumed parabolic band structure [1]. If other complex factors enter

| Symbol | Name | Value | Units |
|---|---|---|---|
| $T$ | temperature | 300 | K |
| $n_0$ | refractive index | 3.5 | – |
| $\mathcal{E}_g$ | bandgap | 0.782 | eV |
| $T_2$ | polarization relaxation time | 120 | fs |
| $T_c$ | electron relaxation time | 300 | fs |
| $T_v$ | hole relaxation time | 70 | fs |
| $m_0$ | free electron mass | $9.11 \cdot 10^{-31}$ | kg |
| $m_c$ | conduction band electron mass | $0.0455 \cdot m_0$ | kg |
| $m_{hh}$ | valence band heavy hole mass | $0.4566 \cdot m_0$ | kg |
| $m_{lh}$ | valence band light hole mass | $0.0951 \cdot m_0$ | kg |
| $\mu^{\mathrm{c}\rightarrow\mathrm{hh}}$ | dipole matrix element c→hh | $1.04 \cdot 10^{-28}$ | Cm |
| $\mu^{\mathrm{c}\rightarrow\mathrm{lh}}$ | dipole matrix element c→lh | $1.04 \cdot 10^{-28}$ | Cm |

Table 2.1: Material parameters used in the gain and index calculations for the InGaAsP material.

the integral in (2.1), which is for example the case when we include gain saturation, then the factor $\mathcal{F}_\mathrm{c} - \mathcal{F}_\mathrm{v}$ must be kept in order to avoid that the real and imaginary parts get mixed up.

The various material parameters that have been used in the calculation of the linear gain and refractive index change are shown in Table 2.1. In Fig. 2.1 and Fig. 2.2 we have shown the linear gain and index change as a function of the photon energy with the carrier density as a parameter. In Fig. 2.3 and Fig. 2.4 we have shown the same quantities but now as a function of the carrier density with the photon energy as a parameter.

The photon energy range has been chosen such that the corresponding wavelength range covers the 1520–1560 nm region. This range is used for the dynamic multi-mode simulations later on in this chapter. Calculations of the gain have been performed in the carrier density range from $1.0 \cdot 10^{24}$ m$^{-3}$ to $2.5 \cdot 10^{24}$ m$^{-3}$. We have also performed calculations for carrier densities for which the medium is absorbing. The absorption and index change for that case has been calculated in the carrier density range from $1.0 \cdot 10^{22}$ m$^{-3}$ to $1.0 \cdot 10^{24}$ m$^{-3}$. Besides the calculation of the linear gain and linear index change for the given carrier density ranges we have also calculated

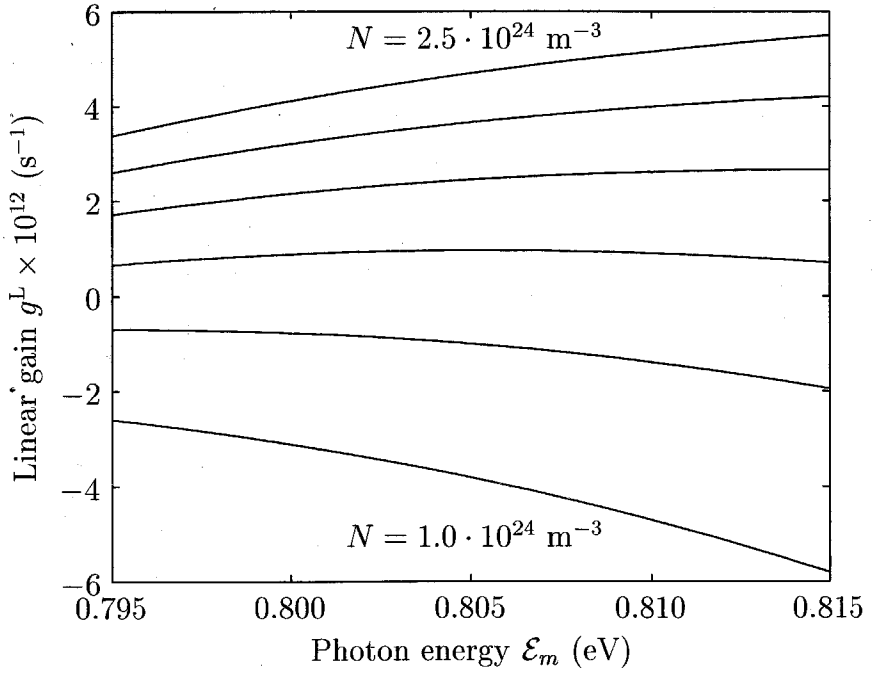


Figure 2.1: Linear gain $g^{\mathrm{L}}$ as a function of the photon energy $\mathcal{E}_m$ with the carrier density $N$ as a parameter. $N$ linearly increases from $1.0 \cdot 10^{24}$ m$^{-3}$ to $2.5 \cdot 10^{24}$ m$^{-3}$ in steps of $3.0 \cdot 10^{23}$ m$^{-3}$.

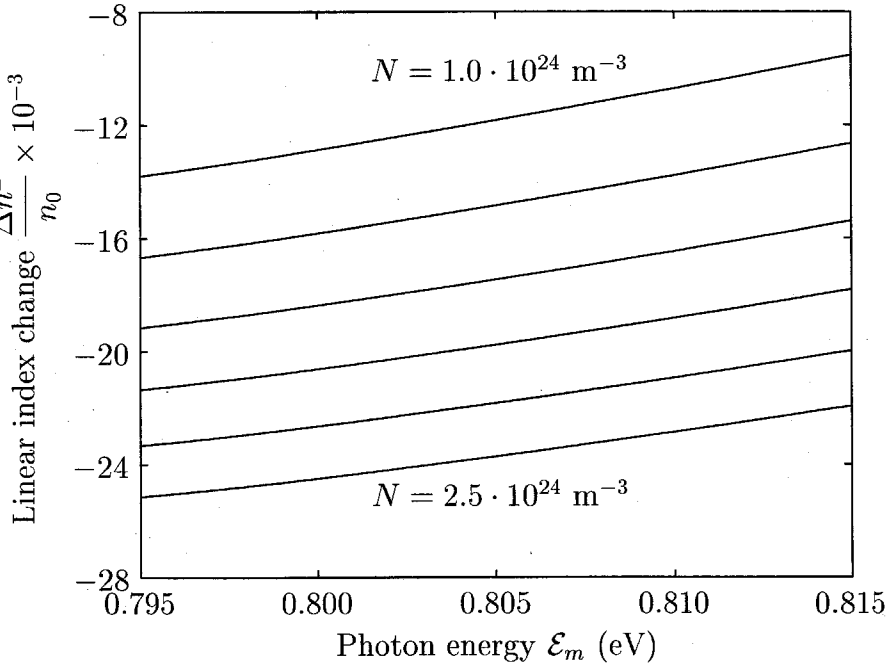


Figure 2.2: Linear index change $\Delta n^{\mathrm{L}}/n_0$ as a function of the photon energy $\mathcal{E}_m$ with the carrier density $N$ as a parameter. $N$ linearly increases from $1.0 \cdot 10^{24}$ m$^{-3}$ to $2.5 \cdot 10^{24}$ m$^{-3}$ in steps of $3.0 \cdot 10^{23}$ m$^{-3}$.

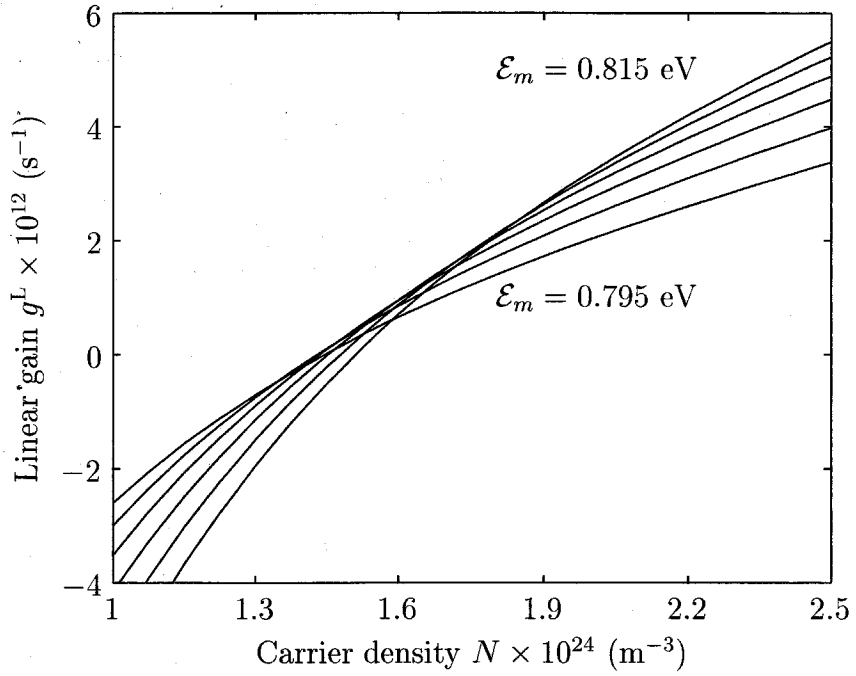


Figure 2.3: Linear gain $g^{\mathrm{L}}$ as a function of the carrier density $N$ with the photon energy $\mathcal{E}_m$ as a parameter. $\mathcal{E}_m$ linearly increases from 0.795 eV to 0.815 eV in steps of 0.004 eV.

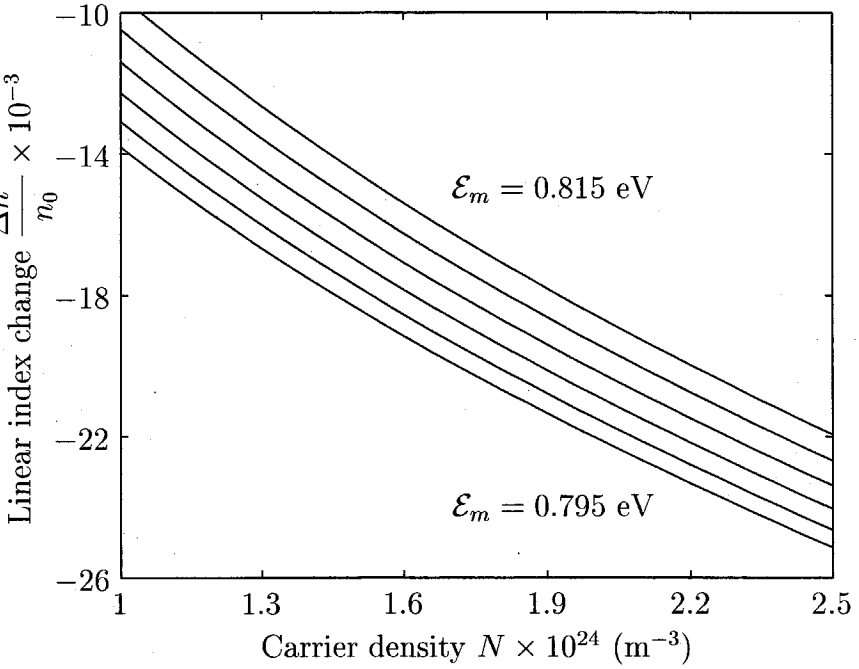


Figure 2.4: Linear index change $\Delta n^{\mathrm{L}}/n_0$ as a function of the carrier density $N$ with the photon energy $\mathcal{E}_m$ as a parameter. $\mathcal{E}_m$ linearly increases from 0.795 eV to 0.815 eV in steps of 0.004 eV.

the spontaneous emission as a function of the photon energy and carrier density. The spontaneous emission rate $W_{sp}(\mathcal{E}_m, N)$ at a certain photon energy $\mathcal{E}_m$ and for a given carrier density $N$ is given by

$$W_{sp}(\mathcal{E}_m, N) = \frac{\mathcal{E}_m}{2\pi^2 \varepsilon_0 n_0^2 \hbar^2} \int_{\mathcal{E}_g}^{\infty} \frac{1/T_2}{(\mathcal{E}_m - \mathcal{E})^2/\hbar^2 + 1/T_2^2} f''(\mathcal{E}, N)\, \mathrm{d}\mathcal{E} \tag{2.7}$$

Here the function $f''(\mathcal{E}, N)$ is defined by

$$\begin{aligned} f''(\mathcal{E}, N) = \mathcal{M}^{\mathrm{c}\to\mathrm{hh}} \left\{ \mathcal{F}_{\mathrm{c}}^{\mathrm{c}\to\mathrm{hh}}(\mathcal{E}, N) \left[1 - \mathcal{F}_{\mathrm{v}}^{\mathrm{c}\to\mathrm{hh}}(\mathcal{E}, N)\right] \right\} \sqrt{(\mathcal{E} - \mathcal{E}_g)/\hbar} \\ + \mathcal{M}^{\mathrm{c}\to\mathrm{lh}} \left\{ \mathcal{F}_{\mathrm{c}}^{\mathrm{c}\to\mathrm{lh}}(\mathcal{E}, N) \left[1 - \mathcal{F}_{\mathrm{v}}^{\mathrm{c}\to\mathrm{lh}}(\mathcal{E}, N)\right] \right\} \sqrt{(\mathcal{E} - \mathcal{E}_g)/\hbar} \end{aligned} \tag{2.8}$$

We can further calculate the spontaneous carrier recombination rate using (2.7) as

$$R_{sp}(N) = \frac{n_0^3}{c^3 \pi^2 \hbar^3} \int_{\mathcal{E}_g}^{\infty} \mathcal{E}^2 W_{sp}(\mathcal{E}, N)\, \mathrm{d}\mathcal{E} \tag{2.9}$$

### 2.2.2 *Nonlinear part of the complex susceptibility*

In a semiconductor the gain spectrum and gain dynamics are affected by intensity dependent non-linear effects due to a finite intraband relaxation time of both the conduction and valence band. Gain nonlinearities have been studied extensively in the past [2–5]. In order to calculate the gain nonlinearities we follow Herzog's density matrix approach [2]. The nonlinear susceptibility is given by

$$\begin{aligned} \chi_{p,q,r}^{\mathrm{NL}} \equiv \chi^{\mathrm{NL}}(\mathcal{E}_p, \mathcal{E}_q, \mathcal{E}_r, N) = \frac{1}{2\pi^2 \varepsilon_0 \hbar} \int_{\mathcal{E}_g}^{\infty} \frac{f(\mathcal{E}, N)}{(\mathcal{E}_r - \mathcal{E})/\hbar - i/T_2} \\ \cdot \left\{ \frac{1/T_2}{(\mathcal{E}_p - \mathcal{E})/\hbar - i/T_2} - \frac{1/T_2}{(\mathcal{E}_q - \mathcal{E})/\hbar + i/T_2} \right\} \\ \cdot \left\{ \frac{1/\overline{T}}{(\mathcal{E}_p - \mathcal{E}_q)/\hbar - i/T_c} + \frac{1/\overline{T}}{(\mathcal{E}_p - \mathcal{E}_q)/\hbar - i/T_v} \right\} \mathrm{d}\mathcal{E} \end{aligned} \tag{2.10}$$

where the band relaxation $\overline{T}$ is given by

$$\overline{T} = T_c + T_v \tag{2.11}$$

where $T_c$ and $T_v$ are the conduction and valence band relaxation time respectively.

For mode $m$ we define the nonlinear gain $g^{\mathrm{NL}}_{m,p,r}$ and the nonlinear index change $\Delta n^{\mathrm{NL}}_{m,p,r}/n_0$ induced by the mixing of three modes by

$$g^{\mathrm{NL}}_{m,p,q} \equiv g^{\mathrm{NL}}(\mathcal{E}_m, \mathcal{E}_p, \mathcal{E}_q, N) = \frac{\mathcal{E}_m}{\hbar} \frac{\chi^{\mathrm{NL},I}_{p,q,m+q-p}}{n_0^2} \tag{2.12a}$$

$$\frac{\Delta n^{\mathrm{NL}}_{m,p,q}}{n_0} \equiv \frac{\Delta n^{\mathrm{NL}}(\mathcal{E}_m, \mathcal{E}_p, \mathcal{E}_q, N)}{n_0} = \frac{\chi^{\mathrm{NL},R}_{p,q,m+q-p}}{2n_0^2} \tag{2.12b}$$

We have calculated the nonlinear gain and index change over the same range of carrier densities and the same range of photon energies as we have done in the previous section for the linear case. We have shown the nonlinear gain and index change in Fig. 2.5 and Fig. 2.6 as a function of the photon energies $\mathcal{E}_p$ and $\mathcal{E}_q$ where we have chosen the carrier density as $N = 1.0 \cdot 10^{24}$ m$^{-3}$ and the energy of the mode of interest as $\mathcal{E}_m = 0.805$ eV. In these figures we have also drawn a number of contour lines in the bottom planes. From Fig. 2.5 it can be easily seen that the most influence of gain saturation occurs around the line for which $\mathcal{E}_p = \mathcal{E}_q$. Maximum saturation occurs at the point where $\mathcal{E}_p = \mathcal{E}_q = \mathcal{E}_m$. Also, the dispersive lineshape for the refractive index of the semiconductor medium can be easily recognized in Fig. 2.6.

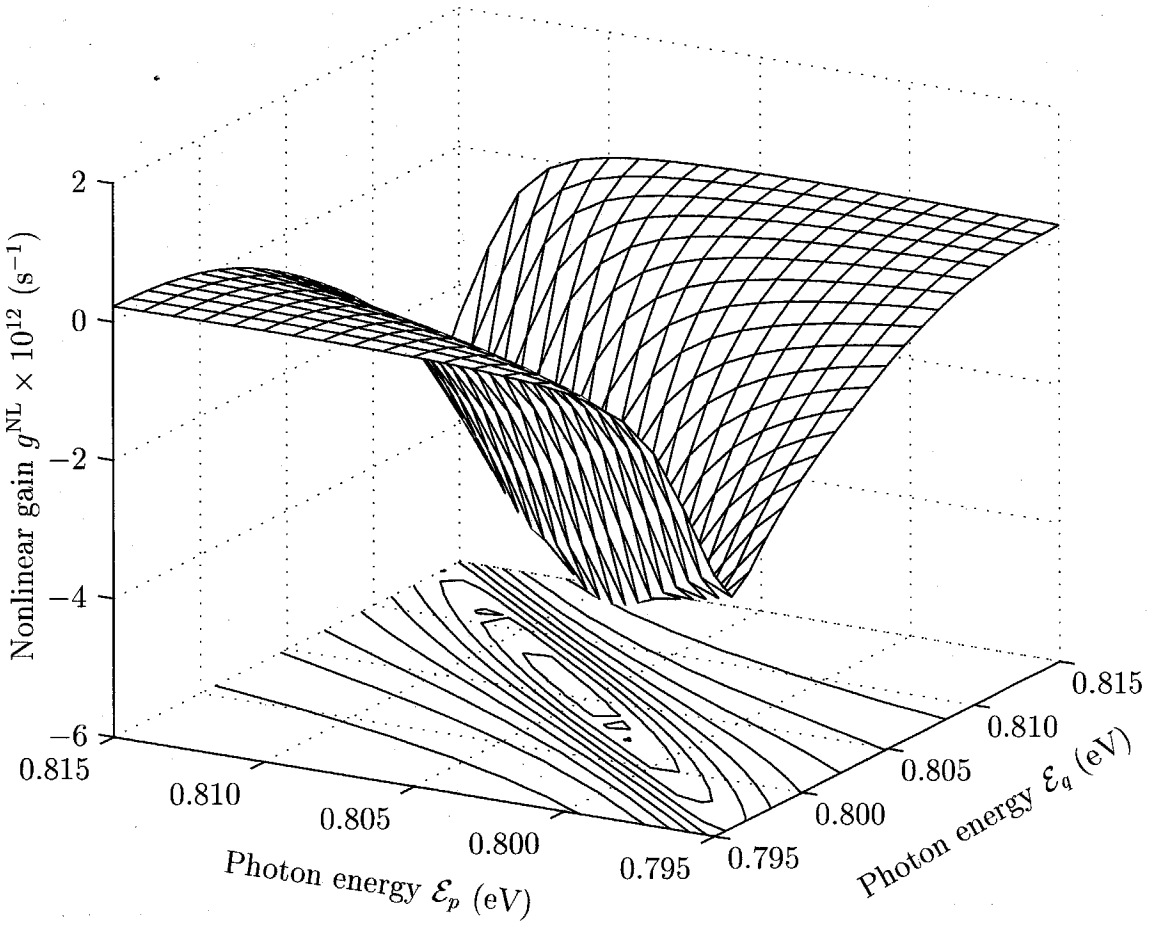


Figure 2.5: Nonlinear gain $g^{\mathrm{NL}}$ as a function of the photon energy $\mathcal{E}_p$ and $\mathcal{E}_q$. The photon energy and carrier density are $\mathcal{E}_m = 0.805$ eV and $N = 1.75 \cdot 10^{24}$ m$^{-3}$ respectively.

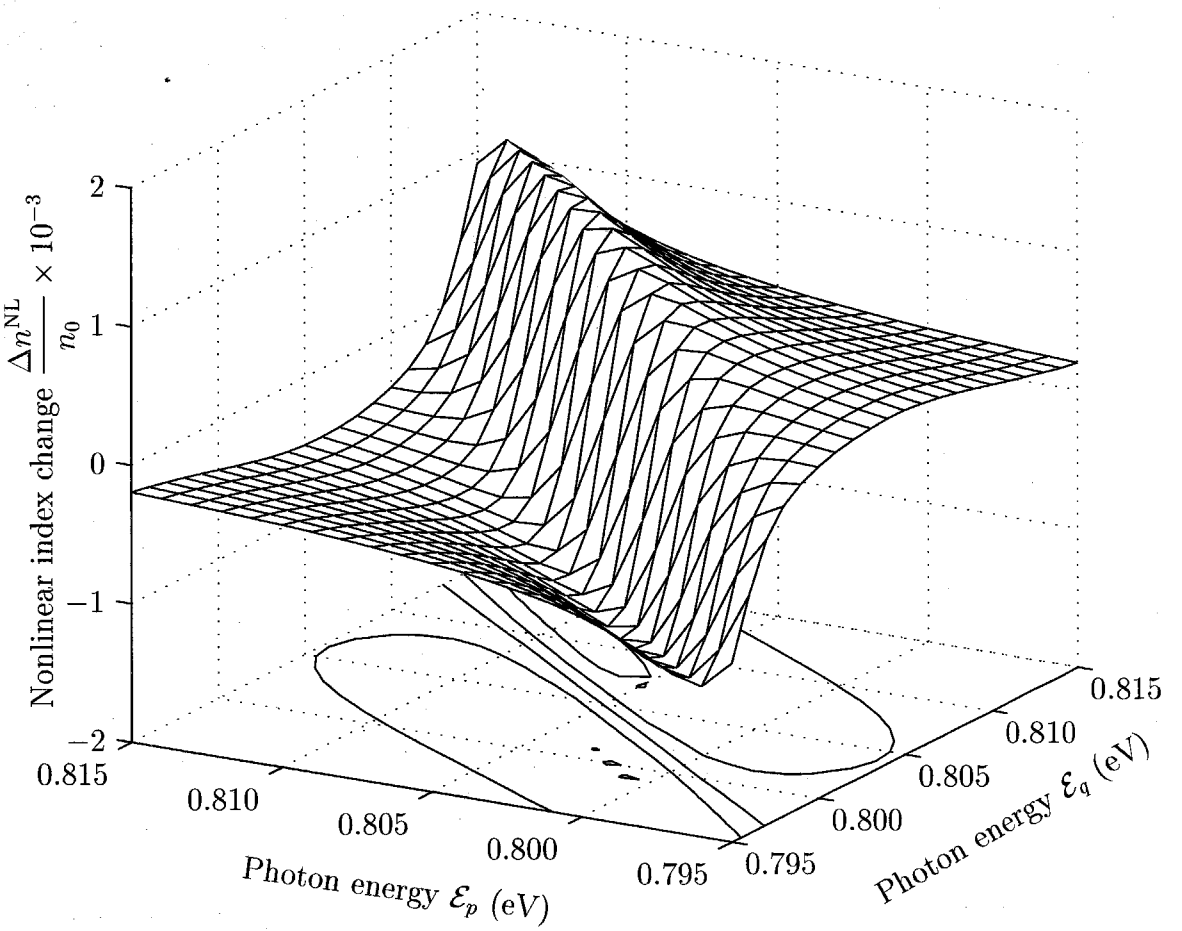


Figure 2.6: Nonlinear index change $\Delta n^{\mathrm{NL}}/n_0$ as a function of the photon energy $\mathcal{E}_p$ and $\mathcal{E}_q$. The photon energy and carrier density are $\mathcal{E}_m = 0.805$ eV and $N = 1.75 \cdot 10^{24}$ m$^{-3}$ respectively.

## 2.3 Derivation of the dynamic multi-mode laser model

In this section we derive the dynamic equations for a semiconductor laser starting from Maxwell's equations. The derived equations are valid for any semiconductor laser but we specifically focus on the dynamics of a mode-locked laser in which the electric field not only responds to a DC susceptibility but also to an AC susceptibility that varies at harmonics of the mode-spacing frequency. In order to find out how the electric field is affected by the polarization we start from Maxwell's equations

$$\nabla \times \boldsymbol{E}(\boldsymbol{r},t) = -\frac{\partial \boldsymbol{B}(\boldsymbol{r},t)}{\partial t} \tag{2.13a}$$

$$\nabla \times \boldsymbol{H}(\boldsymbol{r},t) = \boldsymbol{J}(\boldsymbol{r},t) + \frac{\partial \boldsymbol{D}(\boldsymbol{r},t)}{\partial t} \tag{2.13b}$$

$$\boldsymbol{J}(\boldsymbol{r},t) = \sigma \boldsymbol{E}(\boldsymbol{r},t) \tag{2.13c}$$

$$\boldsymbol{D}(\boldsymbol{r},t) = \varepsilon \boldsymbol{E}(\boldsymbol{r},t) + \boldsymbol{P}(\boldsymbol{r},t) \tag{2.13d}$$

$$\boldsymbol{B}(\boldsymbol{r},t) = \mu_0 \boldsymbol{H}(\boldsymbol{r},t) \tag{2.13e}$$

$$\nabla \cdot \boldsymbol{D}(\boldsymbol{r},t) = 0 \tag{2.13f}$$

$$\nabla \cdot \boldsymbol{B}(\boldsymbol{r},t) = 0 \tag{2.13g}$$

where

| | |
|---|---|
| $\boldsymbol{E}(\boldsymbol{r},t)$ | is the electric field |
| $\boldsymbol{H}(\boldsymbol{r},t)$ | is the magnetic field |
| $\boldsymbol{J}(\boldsymbol{r},t)$ | is the current density |
| $\boldsymbol{B}(\boldsymbol{r},t)$ | is the magnetic flux |
| $\boldsymbol{D}(\boldsymbol{r},t)$ | is the displacement field |
| $\boldsymbol{P}(\boldsymbol{r},t)$ | is the polarization |
| $\sigma$ | is the conductivity |
| $\varepsilon$ | is the permittivity |
| $\mu_0$ | is the permeability of vacuum |

The non-resident part of the susceptibility which accounts for the background index of refraction of the semiconductor is included in the permittivity $\varepsilon$ via $\varepsilon = \varepsilon_0 n_0^2$ where $n_0$ is the background index of refraction and $\varepsilon_0$ is the vacuum permittivity. The resonant component of the susceptibility gives the gain and carrier-induced refractive index change induced by carriers interacting with the electric field.

Taking the curl of (2.13a) and substituting into (2.13b) together with (2.13c)–(2.13f) gives

$$\frac{\partial^2 \boldsymbol{E}(\boldsymbol{r},t)}{\partial t^2} + \frac{\sigma}{\varepsilon}\frac{\partial \boldsymbol{E}(\boldsymbol{r},t)}{\partial t} - \frac{1}{\varepsilon\mu_0}\nabla^2 \boldsymbol{E}(\boldsymbol{r},t) = -\frac{1}{\varepsilon}\frac{\partial^2 \boldsymbol{P}(\boldsymbol{r},t)}{\partial t^2} \tag{2.14}$$

We expand the electric field in terms of the cold cavity modes

$$\boldsymbol{E}(\boldsymbol{r},t) = \sum_m e_m(t)\boldsymbol{u}_m(\boldsymbol{r}) \tag{2.15}$$

where $\boldsymbol{u}_m(\boldsymbol{r})$ are the cold cavity modes satisfying

$$\nabla^2 \boldsymbol{u}_m(\boldsymbol{r}) + \beta_m^2 \boldsymbol{u}_m(\boldsymbol{r}) = 0 \tag{2.16}$$

with the wave number $\beta_m$ defined by

$$\beta_m = \frac{\Omega_m n_0}{c} \tag{2.17}$$

such that the cold cavity mode resonances are given by

$$\Omega_m = m\frac{\pi c}{n_0 L_c} \tag{2.18}$$

where $m$ is the mode number, $L_c$ is the length of the cavity, and $c = 1/\sqrt{\varepsilon_0\mu_0}$ is the speed of light in vacuum. The cold cavity mode solutions to (2.16) are given by

$$\boldsymbol{u}_m(\boldsymbol{r}) = \boldsymbol{u}_m(x,y,z) = \boldsymbol{v}(x,y)u_m(z) \tag{2.19}$$

where

$$u_m(z) = \sqrt{2}\sin(\beta_n z) \tag{2.20}$$

and where the transverse mode structure $\boldsymbol{v}(x, y)$ is considered to be mode independent. We assume that $\boldsymbol{v}(x, y)$ can be approximated by a Gaussian in both the lateral and transverse directions, i.e.,

$$\boldsymbol{v}(x, y) = \frac{1}{\sqrt{\pi}} \exp(-x^2/2D_{\text{mode}}^2) \exp(-y^2/2W_{\text{mode}}^2) \tag{2.21}$$

where $D_{\text{mode}}$ and $W_{\text{mode}}$ are the mode field diameter in the lateral and transverse direction respectively. The longitudinal and transverse mode structure are normalized according to

$$\frac{1}{A_{\text{mode}}} \iint_{A_{\text{mode}}} |\boldsymbol{v}(x, y)|^2 \, \mathrm{d}x \, \mathrm{d}y = 1 \tag{2.22a}$$

$$\frac{1}{L_{\text{c}}} \int_{L_{\text{c}}} u_p(z) u_m^*(z) \, \mathrm{d}z = \delta_{p,m} \tag{2.22b}$$

where $A_{\text{mode}} = D_{\text{mode}} W_{\text{mode}}$ leading to the cold cavity mode normalization

$$\frac{1}{V_{\text{mode}}} \iiint_{V_{\text{mode}}} \boldsymbol{u}_p(\boldsymbol{r}) \boldsymbol{u}_q^*(\boldsymbol{r}) \, \mathrm{d}^3\boldsymbol{r} = \delta_{p,q} \tag{2.23}$$

where $V_{\text{mode}} = A_{\text{mode}} L_{\text{c}}$ is the volume occupied by the mode. We define the following confinement factors in the transverse direction

$$\Gamma = \frac{1}{A_{\text{mode}}} \iint_{A_{\text{act}}} |\boldsymbol{v}(x, y)|^2 \, \mathrm{d}x \, \mathrm{d}y \tag{2.24a}$$

$$\Gamma' = \frac{1}{A_{\text{mode}}} \iint_{A_{\text{act}}} |\boldsymbol{v}(x, y)|^4 \, \mathrm{d}x \, \mathrm{d}y \tag{2.24b}$$

where $A_{\text{act}} = wd$ is the area of the active region where $w$ and $d$ are the width and the thickness of the active region respectively. Using (2.21) we can calculate the

confinement factors as

$$\Gamma = \operatorname{erf}(d/2D_{\text{mode}})\operatorname{erf}(w/2W_{\text{mode}}) \tag{2.25a}$$

$$\Gamma' = \frac{1}{2\pi}\operatorname{erf}(d/\sqrt{2}D_{\text{mode}})\operatorname{erf}(w/\sqrt{2}W_{\text{mode}}) \tag{2.25b}$$

Using the typical values [3] of $d/D_{\text{mode}} = 0.4$ and $w/W_{\text{mode}} = 3$ we find $\Gamma = 0.22$ and $\Gamma' = 0.05$. For future reference we also define the following overlap factors:

$$\xi_{k,p,m} = \Gamma\zeta_{k,p,m} \qquad \zeta_{k,p,m} = \frac{1}{L_{\text{c}}}\int_{L_{\text{act}}} \cos\left(\frac{k\pi z}{L_{\text{c}}}\right) u_p(z)u_m^*(z)\,\mathrm{d}z \tag{2.26a}$$

$$\xi_{p,q,r,m} = \Gamma'\zeta_{p,q,r,m} \qquad \zeta_{p,q,r,m} = \frac{1}{L_{\text{c}}}\int_{L_{\text{act}}} u_p(z)u_q^*(z)u_r(z)u_m^*(z)\,\mathrm{d}z \tag{2.26b}$$

Substituting (2.15) in (2.14), dot multiplying by $\boldsymbol{u}_m^*(\boldsymbol{r})$, integrating over the mode volume and using the orthonormality condition (2.23) gives

$$\frac{\mathrm{d}^2 e_m(t)}{\mathrm{d}t^2} + \frac{1}{\tau_{p,m}}\frac{\mathrm{d}e_m(t)}{\mathrm{d}t} + \Omega_m^2 e_m(t) = -\frac{1}{\varepsilon_0 n_0^2}\frac{\mathrm{d}^2 p_m(t)}{\mathrm{d}t^2} \tag{2.27}$$

where the driving polarization for mode $m$ is given by

$$p_m(t) = \frac{1}{V_{\text{mode}}}\iiint_{V_{\text{mode}}} \boldsymbol{P}(\boldsymbol{r},t)\boldsymbol{u}_m^*(\boldsymbol{r})\,\mathrm{d}^3\boldsymbol{r} \tag{2.28}$$

and where the photon lifetime for mode $m$ has been introduced as

$$\tau_{p,m} = \frac{\varepsilon_0 n_m^2}{\sigma} \tag{2.29}$$

where $n_m$ is the index of refraction for mode $m$. As a solution to (2.27) we take

$$e_m(t) = E_m(t)\,\mathrm{e}^{j\omega_m t} \tag{2.30a}$$

$$p_m(t) = P_m(t)\,\mathrm{e}^{j\omega_m t} \tag{2.30b}$$

where $E_m(t)$ and $P_m(t)$ are the slowly varying complex amplitudes of the electric

field and the polarization respectively. Assuming that both $E_m(t)$ and $P_m(t)$ vary adiabatically, i.e.,

$$\left|\frac{\mathrm{d}^2 E_m(t)}{\mathrm{d}t^2}\right| \ll \omega_m \left|\frac{\mathrm{d}E_m(t)}{\mathrm{d}t}\right| \tag{2.31a}$$

and

$$\left|\frac{\mathrm{d}P_m(t)}{\mathrm{d}t}\right| \ll \omega_m \left|P_m(t)\right| \tag{2.31b}$$

and that the photon lifetime is much longer than an optical cycle

$$\frac{1}{\omega_m \tau_{p,m}} \ll 1 \tag{2.31c}$$

the dynamic mode equation (2.27) can be rewritten as

$$\frac{\mathrm{d}E_m(t)}{\mathrm{d}t} = \left[j(\Omega_m - \omega_m) - \frac{1}{2\tau_{p,m}}\right] E_m(t) - j\frac{\omega_m}{2\varepsilon_0 n_0^2} P_m(t) \tag{2.32}$$

where we have used

$$\frac{\Omega_m^2 - \omega_m^2}{2\omega_m} \approx \Omega_m - \omega_m \tag{2.33}$$

The first term on the right-hand side of (2.32) describes the pulling of the oscillating mode from its cold cavity resonance, the second term represents the cavity loss and the third term represents the driving force for mode $m$. This third term both provides the complex gain for mode $m$ as well as coupling between different modes.

The polarization is related to the electric field by

$$\boldsymbol{P}(\boldsymbol{r},t) = \varepsilon_0 \chi(\boldsymbol{r},t)\boldsymbol{E}(\boldsymbol{r},t) \tag{2.34}$$

The polarization can be split up into a linear and a non-linear part

$$\boldsymbol{P}(\boldsymbol{r},t) = \boldsymbol{P}^{\mathrm{L}}(\boldsymbol{r},t) + \boldsymbol{P}^{\mathrm{NL}}(\boldsymbol{r},t) \tag{2.35}$$

Using (2.15) and (2.30a) we can rewrite the linear part of the susceptibility as

$$\boldsymbol{P}^{\mathrm{L}}(\boldsymbol{r},t) = \varepsilon_0 \sum_p \chi_p^{\mathrm{L}}(\boldsymbol{r},t) E_p(t)\, \mathrm{e}^{j\omega_p t}\, \boldsymbol{u}_p(\boldsymbol{r}) \tag{2.36a}$$

and the nonlinear part as

$$\boldsymbol{P}^{\mathrm{NL}}(\boldsymbol{r},t) = \frac{\varepsilon_0}{I_s} \sum_p \sum_q \sum_r \chi_{p,q,r}^{\mathrm{NL}}(t) E_p(t) E_q^*(t) E_r(t)\, \mathrm{e}^{j(\omega_p - \omega_q + \omega_r)t}\, \boldsymbol{u}_p(\boldsymbol{r}) \boldsymbol{u}_q^*(\boldsymbol{r}) \boldsymbol{u}_r(\boldsymbol{r}) \tag{2.36b}$$

where the linear susceptibility $\chi_p^{\mathrm{L}}$ and the non-linear susceptibility $\chi_{p,q,r}^{\mathrm{NL}}$ are defined according to (2.1) and (2.10). The field saturation intensity is given by [3]

$$I_s = \frac{\hbar^2}{T_2 \overline{T} \mu^2} \tag{2.37}$$

where $\mu$ is the dipole matrix element. The susceptibility depends on $t$ and $\boldsymbol{r}$ only through the carrier density $N(\boldsymbol{r},t)$. Although (2.34) and (2.36) might look suspicious since a convolution would be expected in the time-domain to account for dipole memory, $\chi$ is considered a frequency-domain variable and has effectively a vanishing memory on the time-scale on which $E(t)$ and $N(\boldsymbol{r},t)$ vary.

Without loss of generality we now consider a mode-locked laser and assume a uniform carrier distribution in the lateral and transverse direction of the active region. For a mode-locked laser the photon density inside the cavity is modulated due to the beating of equally spaced modes. In addition to an average DC photon density, part of the photon density varies with a time dependence at the fundamental and higher harmonics of the cavity mode spacing. The photon density inside the laser cavity is given by

$$\begin{aligned} S(z,t) &= \frac{2\varepsilon_0 n_0^2}{\hbar\omega_c} |E(z,t)|^2 \\ &= \frac{2\varepsilon_0 n_0^2}{\hbar\omega_c} \sum_p \sum_q E_p(t) E_q^*(t)\, \mathrm{e}^{j(p-q)\Delta\omega t}\, u_p(z) u_q^*(z) \\ &= S^{(0)}(t) + \sum_{k>0} \left[ S_c^{(k)}(t) \cos(k\Delta\omega t) + S_s^{(k)}(t) \sin(k\Delta\omega t) \right] \cos\left(\frac{k\pi z}{L_c}\right) \end{aligned} \tag{2.38}$$

where $\omega_c$ is the frequency of the central mode and $\Delta\omega = \omega_p - \omega_{p-1}$ is the mode spacing. Defining the photon density for mode $p$ as

$$S_p(t) = \frac{2\varepsilon_0 n_0^2}{\hbar\omega_c}|E_p(t)|^2 \tag{2.39}$$

the DC photon density $S^{(0)}(t)$ is given by

$$S^{(0)}(t) = \sum_p S_p(t) \tag{2.40a}$$

and the photon density at the first harmonic is given by

$$S_c^{(1)}(t) = \sum_p s_{p-1,p}^c(t) + s_{p+1,p}^c(t) \tag{2.40b}$$

$$S_s^{(1)}(t) = \sum_p s_{p-1,p}^s(t) - s_{p+1,p}^s(t) \tag{2.40c}$$

where

$$s_{p,q}^c(t) = \sqrt{S_p(t)S_q(t)}\cos\{\varphi_p(t) - \varphi_q(t)\} \tag{2.41a}$$

$$s_{p,q}^s(t) = \sqrt{S_p(t)S_q(t)}\sin\{\varphi_p(t) - \varphi_q(t)\} \tag{2.41b}$$

and where we have expanded the electric field for mode $p$ as

$$E_p(t) = |E_p(t)|\exp\{j\varphi_p(t)\} \tag{2.42}$$

The photon density succeedingly modulates the carrier density. Accordingly, the time dependent part of the carrier density $N(t)$ is written as

$$\begin{aligned} N(t) &= \sum_{k\geq 0} N^{(k)}(t)\cos\left[k\Delta\omega t + \varphi^{(k)}(t)\right] \\ &= N^{(0)}(t) + \sum_{k>0}\left[N_c^{(k)}(t)\cos\left(k\Delta\omega t\right) + N_s^{(k)}(t)\sin\left(k\Delta\omega t\right)\right] \\ &\approx N^{(0)}(t) + \left[N_c^{(1)}(t)\cos\left(\Delta\omega t\right) + N_s^{(1)}(t)\sin\left(\Delta\omega t\right)\right] \end{aligned} \tag{2.43}$$

Here we have defined the amplitude of the modulation of the carrier density at the $k^{th}$ harmonic $N^{(k)}(t)$ by

$$N^{(k)}(t) = \sqrt{\left[N_c^{(k)}(t)\right]^2 + \left[N_s^{(k)}(t)\right]^2} \tag{2.44}$$

Its phase angle $\varphi^{(k)}(t)$, i.e., its lag with respect to the optical modulation, is given by

$$\varphi^{(k)}(t) = -\sin^{-1}\left(\frac{N_s^{(k)}(t)}{N^{(k)}(t)}\right) \tag{2.45}$$

In the last step of (2.43), we have made the approximation that only the first harmonic of the carrier density is considered. It is noted that the carriers in the semiconductor can only respond to the optical pulsations caused by the beating of two modes when the beating frequency is low enough for the carriers to respond. This means that it is usually sufficient to limit the summation in (2.43) to the fundamental harmonic, i.e., we only consider nearest neighbor mode beating, i.e., $k = 1$.

Similarly, the rate equation for the carrier density $N(t)$ contains both a dc part and an AC part

$$\frac{\mathrm{d}N(t)}{\mathrm{d}t} = \frac{I}{qV_{\mathrm{act}}} - \frac{N(t)}{\tau} - R^{(0)}(t) - R_c^{(1)}(t)\cos(\Delta\omega t) - R_s^{(1)}(t)\sin(\Delta\omega t) \tag{2.46}$$

where the dc stimulated emission rate $R^{(0)}(t)$ is given by

$$R^{(0)}(t) = \Gamma \sum_p g_p^{(0),\mathrm{L}}(t)\zeta_{0,p,p}S_p(t) \tag{2.47a}$$

The AC stimulated emission rates are given by

$$R_c^{(1)}(t) = \frac{\Gamma}{2}\sum_p (g_p^{(0),\mathrm{L}} + g_{p-1}^{(0),\mathrm{L}})\zeta_{0,p,p-1}s_{p-1,p}^c + (g_p^{(0),\mathrm{L}} + g_{p+1}^{(0),\mathrm{L}})\zeta_{0,p,p+1}s_{p-1,p}^c \tag{2.47b}$$

$$R_s^{(1)}(t) = \frac{\Gamma}{2}\sum_p (g_p^{(0),\mathrm{L}} + g_{p-1}^{(0),\mathrm{L}})\zeta_{0,p-1,p}s_{p-1,p}^s - (g_p^{(0),\mathrm{L}} + g_{p+1}^{(0),\mathrm{L}})\zeta_{0,p+1,p}s_{p+1,p}^s \tag{2.47c}$$

Using (2.43) and (2.46) we can derive the following rate equations for $N^{(0)}(t)$, $N_c^{(1)}(t)$ and $N_s^{(1)}(t)$

$$\frac{\mathrm{d}N^{(0)}(t)}{\mathrm{d}t} = \frac{I}{qV_{\mathrm{act}}} - \frac{N^{(0)}(t)}{\tau} - R^{(0)}(t) \tag{2.48a}$$

$$\frac{\mathrm{d}N_c^{(1)}(t)}{\mathrm{d}t} = -\frac{N_c^{(1)}(t)}{\tau} - \Delta\omega N_s^{(1)}(t) - R_c^{(1)}(t) \tag{2.48b}$$

$$\frac{\mathrm{d}N_s^{(1)}(t)}{\mathrm{d}t} = -\frac{N_s^{(1)}(t)}{\tau} + \Delta\omega N_c^{(1)}(t) - R_s^{(1)}(t) \tag{2.48c}$$

where $q$ is the electron charge.

In its turn the carrier density drives the linear susceptibility which is thus also modulated at the fundamental and higher harmonics of the mode spacing. We therefore expand the susceptibility in (2.36) as

$$\chi_p^{\mathrm{L}}(z,t) = \frac{1}{2}\sum_k (1+\delta_k)\chi_p^{(k),\mathrm{L}}(t)\,\mathrm{e}^{j\{k\Delta\omega t+\varphi^{(k)}(t)\}}\cos\left(\frac{k\pi z}{L_{\mathrm{c}}}\right) \tag{2.49}$$

where the summation now is performed over both positive and negative $k$ and where $\chi_p^{(-k),\mathrm{L}} = -\chi_p^{*(k),\mathrm{L}}$ and $\varphi^{(-k)}(t) = -\varphi^{(k)}(t)$. Using (2.28), (2.30b) and (2.49) we can write the slowly varying polarization for mode $m$ as

$$P_m^{\mathrm{L}}(t) = \frac{1}{2}\varepsilon_0 \sum_k \sum_p (1+\delta_k)\delta_{p+k,m}\chi_p^{(k),\mathrm{L}}(t)E_p(t)\,\mathrm{e}^{j\{\varphi^{(k)}+\psi_{k,p,m}(t)\}}\,\xi_{k,p,m} \tag{2.50a}$$

$$P_m^{\mathrm{NL}}(t) = \frac{\varepsilon_0}{I_s}\sum_p \sum_q \sum_r \delta_{p-q+r,m}\chi_{p,q,r}^{\mathrm{NL}}(t)E_p(t)E_q^*(t)E_r(t)\,\mathrm{e}^{j\psi_{p,q,r,m}(t)}\,\xi_{p,q,r,m} \tag{2.50b}$$

where $\xi_{k,p,m}$ and $\xi_{p,q,r,m}$ are defined according to (2.26) and

$$\psi_{k,p,m}(t) = k\Delta\omega + (\omega_p - \omega_m)t \tag{2.51a}$$

$$\psi_{p,q,r,m}(t) = (\omega_p - \omega_q + \omega_r - \omega_m)t \tag{2.51b}$$

It is noted that in (2.26) the integration is performed over the active region, i.e., the region where the resonant susceptibility is non-zero.

We again limit the summation in (2.50) to the fundamental harmonics $-1 \le k \le 1$,

i.e., we only consider nearest neighbor mode beating and mode coupling. The linear polarization term can then be rewritten as

$$\begin{aligned} P_m^{\mathrm{L}}(t) = {} & \varepsilon_0 \chi_m^{(0),\mathrm{L}}(t) E_m(t) \xi_{0,m,m} \\ & + \frac{1}{2}\varepsilon_0 \chi_{m-1}^{(1),\mathrm{L}}(t)\, \mathrm{e}^{j\varphi^{(1)}(t)}\, E_{m-1}(t) \xi_{+1,m-1,m} \\ & + \frac{1}{2}\varepsilon_0 \chi_{m+1}^{(1),\mathrm{L}}(t)\, \mathrm{e}^{-j\varphi^{(1)}(t)}\, E_{m+1}(t) \xi_{-1,m+1,m} \end{aligned} \tag{2.52}$$

The linear susceptibility $\chi^{(1),\mathrm{L}}$ at the first harmonic is approximated from the amplitude $N^{(1)}$ of the carrier density modulation around its average value $N^{(0)}$ according to

$$\chi_m^{(1),\mathrm{L}} = \frac{1}{2}\left[\chi_m^{(0),\mathrm{L}}\left(N^{(0)} + N^{(1)}\right) - \chi_m^{(0),\mathrm{L}}\left(N^{(0)} - N^{(1)}\right)\right] \tag{2.53}$$

The non-linear polarization term (2.50b) can be split up into the following terms

$$P_m^{\mathrm{SAT}}(t) = \frac{\varepsilon_0}{I_s} \sum_p \chi_{p,p,m}^{\mathrm{NL}}(t) |E_p(t)|^2 E_m(t) \xi_{p,p,m,m} \tag{2.54a}$$

$$P_m^{\mathrm{PP}}(t) = \frac{\varepsilon_0}{I_s} \sum_{q \neq m} \chi_{m,q,q}^{\mathrm{NL}}(t) E_m(t) |E_q(t)|^2 \xi_{m,q,q,m} \tag{2.54b}$$

$$P_m^{\mathrm{FWM}}(t) = \frac{\varepsilon_0}{I_s} \sum_{p \neq m} \sum_{q \neq p} \chi_{p,q,m+q-p}^{\mathrm{NL}}(t) E_p(t) E_q^*(t) E_{m+q-p}(t) \xi_{p,q,m+q-p,m} \tag{2.54c}$$

The polarization term $P_m^{\mathrm{SAT}}$ represents the saturation (SAT) of the complex gain due to static hole burning (both spatially and spectrally). The self-saturation term is given for $p = m$ while the cross-saturation term are given for $p \neq m$. The term $P_m^{\mathrm{PP}}$ represents the saturation due to population pulsations (PP) caused by the beating of two modes. The term $P_m^{\mathrm{FWM}}$ is due to four-wave mixing (FWM) and causes additional coupling between the modes.

Using (2.5), (2.12) and (2.42) and substituting into (2.32) gives the rate equations

for the mode amplitudes

$$\begin{aligned}\frac{\mathrm{d}|E_m|}{\mathrm{d}t} &= \left[\Gamma\frac{g_m^{(0),\mathrm{L}}}{2}\zeta_{0,m,m} - \frac{1}{2\tau_{p,m}}\right]|E_m| \\ &+ \frac{\Gamma}{2}\left[\frac{g_{m-1}^{(1),\mathrm{L}}}{2}\cos(\phi_{+1,m-1,m}) + \omega_{m-1}\frac{\Delta n_{m-1}^{(1),\mathrm{L}}}{n_0}\sin(\phi_{+1,m-1,m})\right]\zeta_{+1,m-1,m}|E_{m-1}| \\ &+ \frac{\Gamma}{2}\left[\frac{g_{m+1}^{(1),\mathrm{L}}}{2}\cos(\phi_{-1,m+1,m}) + \omega_{m+1}\frac{\Delta n_{m+1}^{(1),\mathrm{L}}}{n_0}\sin(\phi_{-1,m+1,m}))\right]\zeta_{-1,m+1,m}|E_{m+1}| \\ &+ \Gamma'\sum_p \frac{g_{m,p,p}^{\mathrm{NL}}}{2}\zeta_{p,p,m,m}\frac{|E_p|^2}{I_s}|E_m| + \Gamma'\sum_{q\neq m}\frac{g_{m,m,q}^{\mathrm{NL}}}{2}\zeta_{m,q,q,m}\frac{|E_q|^2}{I_s}|E_m| \\ &+ \Gamma'\sum_{p\neq m}\sum_{q\neq p}\left[\frac{g_{m,p,q}^{\mathrm{NL}}}{2}\cos(\phi_{p,q,r,m}) + \omega_m\frac{\Delta n_{m,p,q}^{\mathrm{NL}}}{n_0}\sin(\phi_{p,q,r,m})\right]\zeta_{p,q,r,m}\frac{|E_p||E_q|}{I_s}|E_r|\end{aligned} \tag{2.55}$$

where $r = m + q - p$, $\phi_{k,p,m} = \varphi^{(k)} + \varphi_p - \varphi_m$ and $\phi_{p,q,r,m} = \varphi_p - \varphi_q + \varphi_r - \varphi_m$. The rate equations for the phases of the modes are given by

$$\begin{aligned}\frac{\mathrm{d}\varphi_m}{\mathrm{d}t} &= \Omega_m - \omega_m - \omega_m\Gamma\frac{\Delta n_m^{\mathrm{L}}}{n_0}\zeta_{0,m,m} \\ &+ \frac{\Gamma}{2}\left[\frac{g_{m-1}^{(1),\mathrm{L}}}{2}\sin(\phi_{+1,m-1,m}) - \omega_{m-1}\frac{\Delta n_{m-1}^{(1),\mathrm{L}}}{n_0}\cos(\phi_{+1,m-1,m})\right]\zeta_{+1,m-1,m}|E_{m-1}| \\ &+ \frac{\Gamma}{2}\left[\frac{g_{m+1}^{(1),\mathrm{L}}}{2}\sin(\phi_{-1,m+1,m}) - \omega_{m+1}\frac{\Delta n_{m+1}^{(1),\mathrm{L}}}{n_0}\cos(\phi_{-1,m+1,m}))\right]\zeta_{-1,m+1,m}|E_{m+1}| \\ &- \Gamma'\sum_p \omega_m\frac{\Delta n_{m,p,p}^{\mathrm{NL}}}{n_0}\zeta_{p,p,m,m}\frac{|E_p|^2}{I_s} - \Gamma'\sum_{q\neq m}\omega_m\frac{\Delta n_{m,m,q}^{\mathrm{NL}}}{n_0}\zeta_{m,q,q,m}\frac{|E_q|^2}{I_s} \\ &+ \Gamma'\sum_{p\neq m}\sum_{q\neq p}\left[\frac{g_{m,p,q}^{\mathrm{NL}}}{2}\sin(\phi_{p,q,r,m}) - \omega_m\frac{\Delta n_{m,p,q}^{\mathrm{NL}}}{n_0}\cos(\phi_{p,q,r,m})\right]\zeta_{p,q,r,m}\frac{|E_p||E_q|}{I_s}\frac{|E_r|}{|E_m|}\end{aligned} \tag{2.56}$$

It is useful to write the mode equations in terms of photon densities using (2.39). We

can then rewrite (2.55) as

$$\begin{aligned}
\frac{\mathrm{d}S_m}{\mathrm{d}t} &= \left[\Gamma g_m^{\mathrm{L}}\zeta_{0,m,m} - \frac{1}{\tau_{p,m}}\right] S_m \\
&+ \frac{\Gamma}{2}\left[g_{m-1}^{(1),\mathrm{L}}\cos(\phi_{+1,m-1,m}) + 2\omega_{m-1}\frac{\Delta n_{m-1}^{(1),\mathrm{L}}}{n_0}\sin(\phi_{+1,m-1,m})\right]\zeta_{+1,m-1,m}\sqrt{S_{m-1}S_m} \\
&+ \frac{\Gamma}{2}\left[g_{m+1}^{(1),\mathrm{L}}\cos(\phi_{-1,m+1,m}) + 2\omega_{m+1}\frac{\Delta n_{m+1}^{(1),\mathrm{L}}}{n_0}\sin(\phi_{-1,m+1,m}))\right]\zeta_{-1,m+1,m}\sqrt{S_{m+1}S_m} \\
&+ \Gamma'\sum_p g_{m,p,p}^{\mathrm{NL}}\zeta_{p,p,m,m}\frac{S_p}{S_s}S_m + \Gamma'\sum_{q\neq m} g_{m,m,q}^{\mathrm{NL}}\zeta_{m,q,q,m}\frac{S_q}{S_s}S_m \\
&+ \Gamma'\sum_{p\neq m}\sum_{q\neq p}\left[g_{m,p,q}^{\mathrm{NL}}\cos(\phi_{p,q,r,m}) + 2\omega_m\frac{\Delta n_{m,p,q}^{\mathrm{NL}}}{n_0}\sin(\phi_{p,q,r,m})\right]\zeta_{p,q,r,m}\frac{\sqrt{S_pS_q}}{S_s}\sqrt{S_rS_m}
\end{aligned} \tag{2.57}$$

Here the photon saturation density is given by

$$S_s = \frac{2\varepsilon_0 n_0^2}{\hbar\omega_c} I_s \tag{2.58}$$

The rate equations for the phases of the modes (2.56) can be rewritten as

$$\begin{aligned}
\frac{\mathrm{d}\varphi_m}{\mathrm{d}t} &= \Omega_m - \omega_m - \omega_m\Gamma\frac{\Delta n_m^{\mathrm{L}}}{n_0}\zeta_{0,m,m} \\
&+ \frac{\Gamma}{2}\left[\frac{g_{m-1}^{(1),\mathrm{L}}}{2}\sin(\phi_{+1,m-1,m}) - \omega_{m-1}\frac{\Delta n_{m-1}^{(1),\mathrm{L}}}{n_0}\cos(\phi_{+1,m-1,m})\right]\zeta_{+1,m-1,m}\sqrt{S_{m-1}S_m} \\
&+ \frac{\Gamma}{2}\left[\frac{g_{m+1}^{(1),\mathrm{L}}}{2}\sin(\phi_{-1,m+1,m}) - \omega_{m+1}\frac{\Delta n_{m+1}^{(1),\mathrm{L}}}{n_0}\cos(\phi_{-1,m+1,m}))\right]\zeta_{-1,m+1,m}\sqrt{S_{m+1}S_m} \\
&- \Gamma'\sum_p \omega_m\frac{\Delta n_{m,p,p}^{\mathrm{NL}}}{n_0}\zeta_{p,p,m,m}\frac{S_p}{S_s} - \Gamma'\sum_{q\neq m}\omega_m\frac{\Delta n_{m,m,q}^{\mathrm{NL}}}{n_0}\zeta_{m,q,q,m}\frac{S_q}{S_s} \\
&+ \Gamma'\sum_{p\neq m}\sum_{q\neq p}\left[\frac{g_{m,p,q}^{\mathrm{NL}}}{2}\sin(\phi_{p,q,r,m}) - \omega_m\frac{\Delta n_{m,p,q}^{\mathrm{NL}}}{n_0}\cos(\psi_{p,q,r,m})\right]\zeta_{p,q,r,m}\frac{\sqrt{S_pS_q}}{S_s}\sqrt{\frac{S_r}{S_m}}
\end{aligned} \tag{2.59}$$

Summarizing, the complete dynamic behavior of the laser is described by the modal rate equations (2.57) and (2.59) and the carrier density rate equations (2.48).

In the following sections these rate equations are numerically integrated using a fourth-order Runge-Kutta integration algorithm with adaptive stepsize [6]. On each integration step the frequencies of the modes are adjusted according to

$$\omega_m^{k+1} = \omega_m^k + \frac{\mathrm{d}\varphi_m}{\mathrm{d}t} \tag{2.60}$$

where $k$ indicates the time-step. The mode-spacing $\Delta\omega$ for the next step is calculated from a weighted average according to

$$\Delta\omega^{k+1} = \frac{1}{2}\sum_m (\omega_{m+1}^{k+1} - \omega_{m-1}^{k+1})\frac{S_m}{S^{(0)}} \tag{2.61}$$

On each iteration the mode index $n_m$ is calculated according to

$$n_m = n_0\left(1 + \frac{\Delta n_m^{\mathrm{L}}}{n_0}\right) \tag{2.62}$$

and the photon lifetime for mode $m$ is calculated from

$$\frac{1}{\tau_{p,m}} = \frac{c}{n_m}\left[\frac{1}{L_{\mathrm{c}}}\ln\left(\frac{1}{R}\right) + \alpha_c\right] \tag{2.63}$$

where $R$ is the facet power reflectivity and $\alpha_c$ is the cavity loss.

## 2.4 Mode competition in mode-locked lasers

In this section we will consider a mode-locked semiconductor laser with a total cavity length $L_c = 2000$ $\mu$m. The laser cavity consists of a gain section and an absorber section. The length of the gain section is $L_g = 1900$ $\mu$m and covers the area where $0 \leq z \leq L_g$. The absorber section has a length of $L_a = 100$ $\mu$m and covers the area where $L_c - L_a \leq z \leq L_c$.

Using (2.26), the overlap factor for the gain section $\zeta_{0,m,m}^g$ and the overlap factor

for the absorber section $\zeta^a_{0,m,m}$ are given by

$$\zeta^g_{0,m,m} = \frac{2}{L_c}\int_0^{L_g} \sin^2\left(\frac{m\pi z}{L_c}\right) dz \approx \frac{L_g}{L_c} = 0.95 \tag{2.64a}$$

$$\zeta^a_{0,m,m} = \frac{2}{L_c}\int_{L_c-L_a}^{L_c} \sin^2\left(\frac{m\pi z}{L_c}\right) dz \approx \frac{L_a}{L_c} = 0.05 \tag{2.64b}$$

where in the last approximation we have assumed that the mode number $m$ is large (for our laser the $m \sim 9000$). It is noted that the integrals (2.26) can actually be solved analytically. In our simulations later on we use the exact values calculated from (2.26) and not the approximated ones as given in (2.64).

The overlap factors $\zeta^g_{+1,m-1,m}$, $\zeta^g_{-1,m+1,m}$, $\zeta^a_{+1,m-1,m}$ and $\zeta^a_{-1,m+1,m}$ for the gain and absorber section respectively can be calculated analytically as well. For large $m$ they are approximately equal to

$$\zeta^g_{+1,m-1,m} \approx \zeta^g_{-1,m+1,m} = \frac{1}{2}\frac{L_g}{L_c} + \frac{1}{4\pi}\sin\left(\frac{2\pi L_g}{L_c}\right) \approx 0.45 \tag{2.65a}$$

$$\zeta^a_{+1,m-1,m} \approx \zeta^a_{-1,m+1,m} = \frac{1}{2}\frac{L_a}{L_c} - \frac{1}{4\pi}\sin\left(\frac{2\pi L_g}{L_c}\right) \approx 0.05 \tag{2.65b}$$

The overlap factors $\zeta^{g,a}_{p,q,m+q-p,m}$ for the FWM process are given by (2.26b). A plot of the FWM overlap factor for the gain section as a function of the mode numbers $p$ and $q$ for a central mode $m = 9000$ is shown in Fig. 2.7. Looking at Fig. 2.5, Fig. 2.6 and Fig. 2.7 it can be seen that most of the nonlinear contributions in the modal rate equations (2.57) and (2.59) come from the summation terms for which $q = p$ (saturation terms) and $q = p \pm 1$ (mixing of nearest neighbor modes). In our simulations we have limited the summations to these terms as we only consider nearest neighbor mode coupling. It is noted that higher order coupling between modes can be easily included as well. In this case the modulation of the carrier density at higher harmonics also needs to be taken into account.

We have next simulated our laser by integrating the modal amplitude and phase rate equations (2.57) and (2.59) and the carrier rate equations (2.48a)–(2.48c) for both

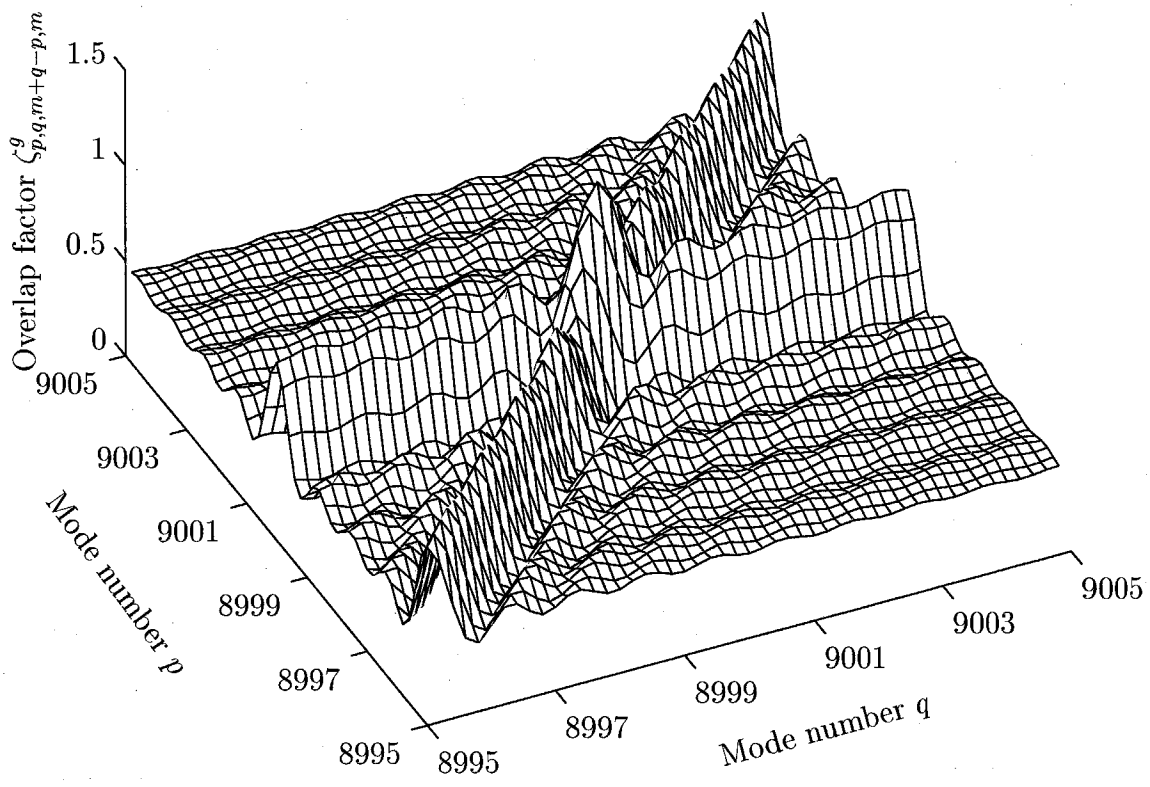


Figure 2.7: Overlap factor $\zeta^g_{p,q,m+q-p,m}$ for the gain section as a function of the mode number $p$ and the mode number $q$ for a central mode number $m = 9000$.

| Symbol | Name | Value | Units |
|---|---|---|---|
| $n_0$ | refractive index | 3.5 | — |
| $\alpha_c$ | cavity loss | 5.0 | $cm^{-1}$ |
| $R$ | mirror power reflectivity | 0.3 | — |
| $S_s$ | photon saturation density | $3.9 \cdot 10^{22}$ | $m^{-3}$ |
| $\Delta\Omega$ | cold cavity mode spacing | $134.6 \cdot 10^9$ | $s^{-1}$ |
| $\tau_g$ | carrier lifetime in gain section | 1.0 | ns |
| $\tau_a$ | carrier lifetime in absorber section | 0.1 | ns |
| $L_c$ | cavity length | 2000 | $\mu$m |
| $L_g$ | gain section length | 1900 | $\mu$m |
| $L_a$ | absorber section length | 100 | $\mu$m |
| $w$ | width of the active region | 3.0 | $\mu$m |
| $d$ | thickness of the active region | 0.1 | $\mu$m |
| $\Gamma$ | confinement factor | 0.22 | — |
| $\Gamma'$ | confinement factor | 0.05 | — |
| $I_g$ | gain current | 250 | mA |
| $I_a$ | absorber current | 5 | mA |
| $M$ | number of modes | 75 | — |
| $M_c$ | central mode number | 9004 | — |

Table 2.2: Parameters used in the simulations.

the gain section and absorber section. The total number of equations to be integrated equals $2M+6$ where $M$ is the number of modes that is being considered. In Table 2.2 we have summarized the various parameters that are used in the simulations in this and the next section.

The typical startup behaviour of the laser in the first 4 nanoseconds is shown in Fig. 2.8. The gain section is pumped at $I_g = 250$ mA, the absorber section is pumped at $I_a = 5$ mA and the currents are turned on at $t = 0$. The carrier density in the gain section increases slowly and the photon density starts to build up. The increasing number of photons in the laser cavity start to saturate the gain causing the well-known relaxation oscillation behavior. The relaxation oscillation is clearly visible in Fig. 2.8 and is a result of the out-of-phase interaction between the carriers in the gain section and the photons. The relaxation frequency is approximately equal to $f_r = 4.1$ GHz. The relaxation oscillation is eventually damped out when the gain

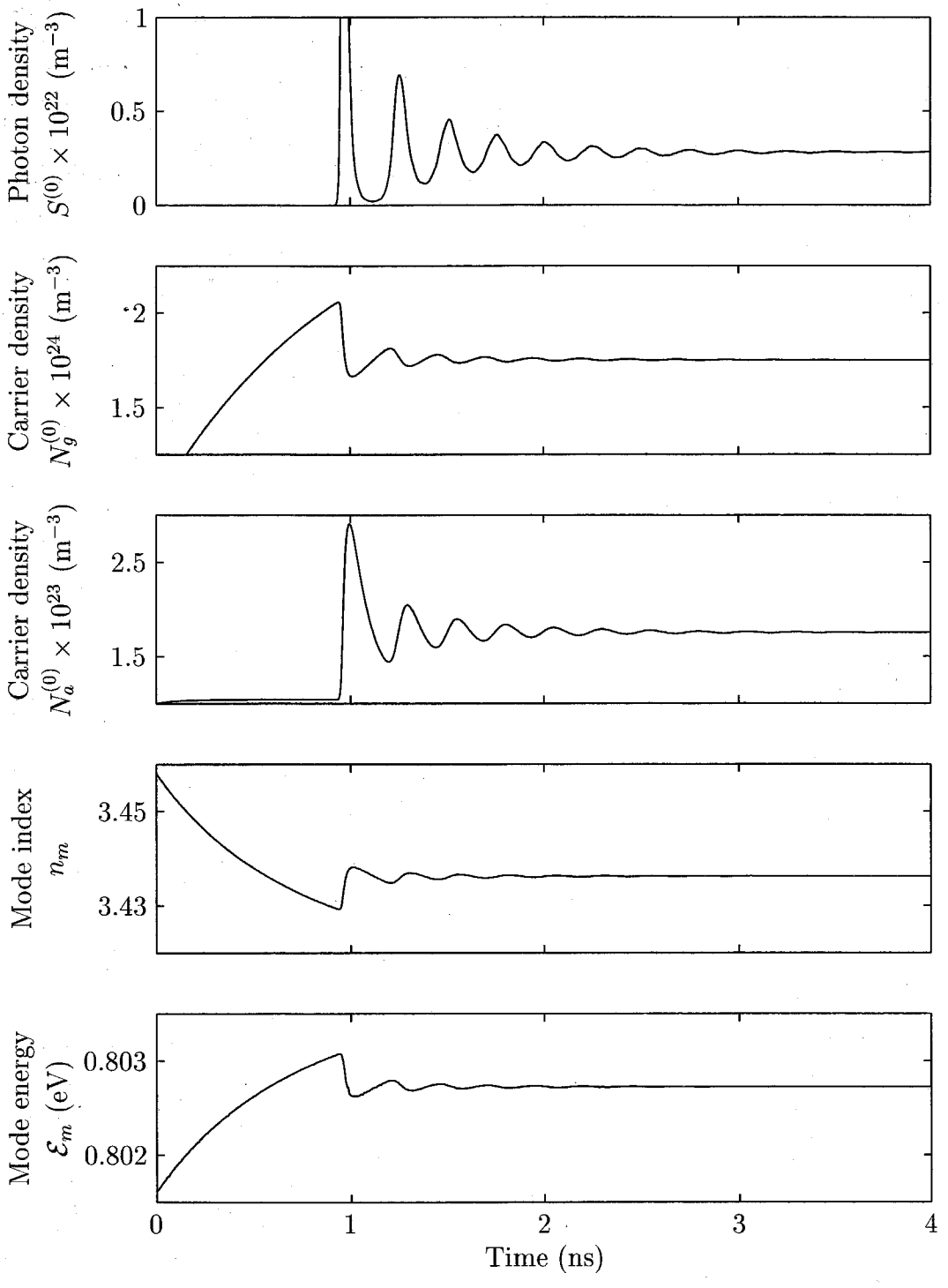


Figure 2.8: Time evolution of the DC photon density $S^{(0)}$, the DC carrier density in the gain section $N_g^{(0)}$ and in the absorber section $N_a^{(0)}$, and the refractive index, $n_m$, and energy, $\mathcal{E}_m$, for the central mode $m = M_c$.

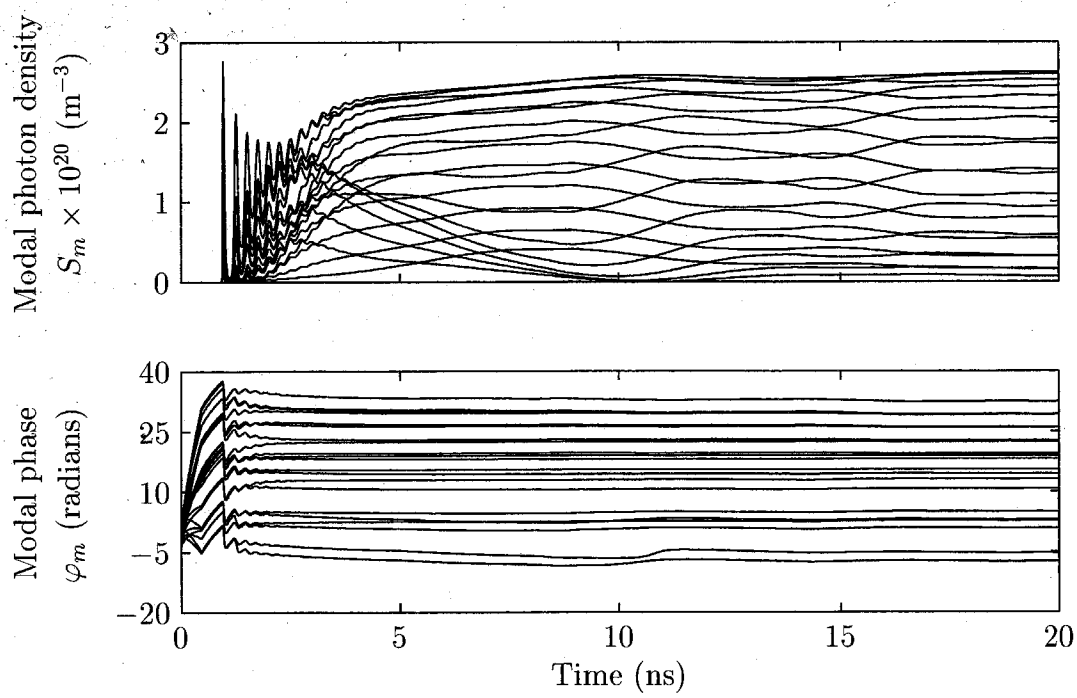


Figure 2.9: Time evolution of the photon densities $S_m$ and the phases $\varphi_m$ for modal numbers $M_c - 10 \leq m \leq M_c + 10$ with $M_c = 9004$.

of the laser medium is clamped at its steady-state value. Due to the fact that the absorber section is biased below transparency, its carrier density is in-phase with the photon-density, i.e., the photons create carriers in the absorber section.

As a result of the change in carrier density, mainly in the gain section, the refractive index of the semiconductor material decreases over time as well. This causes detuning of the energies of the modes from their cold cavity resonant energies (see Fig. 2.8) and detuning of the mode-spacing from the cold cavity mode-spacing. It can be seen that the total photon density $S^{(0)}$, the DC gain carrier density $N_g^{(0)}$ and absorber carrier density $N_a^{(0)}$, the modal refractive index $n_m$ and energy $\mathcal{E}_m$ reach their steady states within a few nanoseconds. As we will see next this is not true for the photon density and phase of each individual mode. The individual modes compete with each other on a longer time scale, typically up to a hundred nanoseconds.

In Fig. 2.9 we have plotted the time evolution of the amplitude and phase of each of the modes. As we can see from Fig. 2.9, the amplitudes and phases of the modes follow the relaxation oscillation behaviour during the first few nanoseconds. The

phases of the modes are locked to each other in these first few nanoseconds as well. The competition between the modes, however, takes place over a much longer time. Even after 20 nanoseconds the individual mode amplitudes still have not reached their steady-state values. Although the modes are locked in phase to each other, they are still competing for the gain medium. Clearly visible is the fact that the modes on one side of the main mode are anti-correlated with the modes on the other side of the main mode. All modes exchange power between each other through nearest neighbor mode coupling. The total photon density in the cavity remains constant throughout this process of mode-competition, which means that some modes grow in amplitude at the cost of others. This process of energy exchange between all of the competing modes continues until finally a steady-state is reached where the amount of energy that a mode obtains from its neighbors is equal to the amount of energy that mode gives to its neighbors. For our simulations a steady-state is reached after about 100 nanoseconds.

The detuning $\delta(t)$ of the mode-spacing from the cold cavity mode spacing in steady-state is

$$\delta(t) = \Delta\omega(t) - \Delta\Omega = -3.47 \cdot 10^9 \text{ s}^{-1} \tag{2.66}$$

This detuning is caused by the dispersion of the material expressed through the change of the refractive index caused by the real part of the linear susceptibility, see (2.5b).

The mode-locked spectrum in steady-state is shown in Fig. 2.10. About 25 modes are locked together. In Fig. 2.10 we have also plotted the spectral phase of the modes resulting from the simulation. The phase curvature indicates that the mode-locked pulse contains a non-linear spectral chirp. In order to determine the chirp values of the pulse, we fit the spectral phase around the center mode with frequency $\omega_c$ to a $4^{th}$ order polynomial according to

$$\varphi(\omega) = \varphi(\omega_c) + \frac{\mathrm{d}\varphi}{\mathrm{d}\omega}(\omega - \omega_c) + \frac{1}{2}\frac{\mathrm{d}^2\varphi}{\mathrm{d}\omega^2}(\omega - \omega_c)^2 + \frac{1}{6}\frac{\mathrm{d}^3\varphi}{\mathrm{d}\omega^3}(\omega - \omega_c)^3 + \ldots \tag{2.67}$$

This fitting gives a linear spectral chirp $\mathrm{d}^2\varphi/\,\mathrm{d}\omega^2 \approx -5.3$ ps$^2$ and a nonlinear spectral chirp $\mathrm{d}^3\varphi/\,\mathrm{d}\omega^3 \approx -1.5$ ps$^3$ and $\mathrm{d}^4\varphi/\,\mathrm{d}\omega^4 \approx 8.8$ ps$^4$.

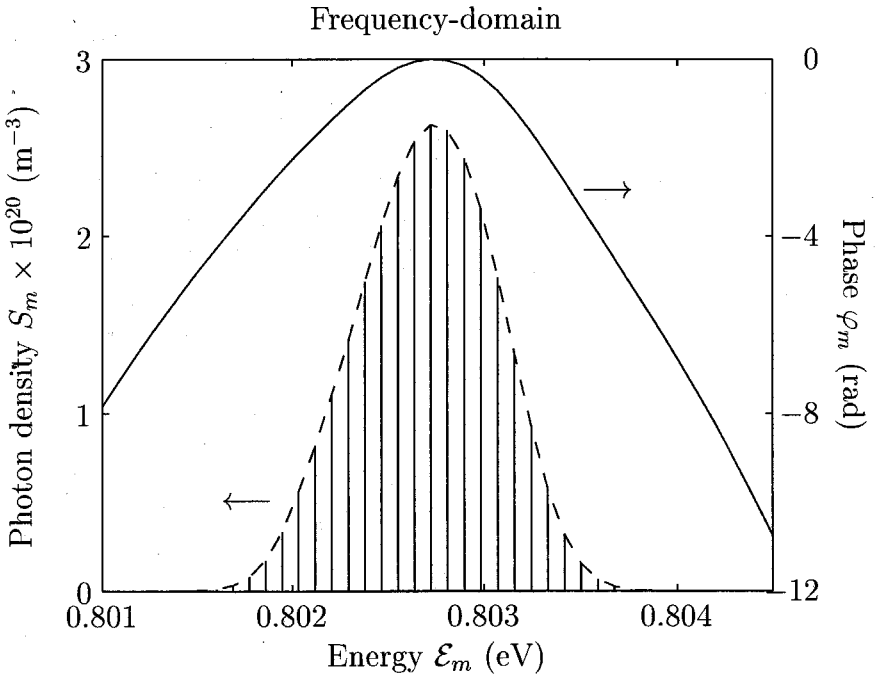


Figure 2.10: Photon density $S_m$ and phase $\varphi_m$ for each mode in steady state.

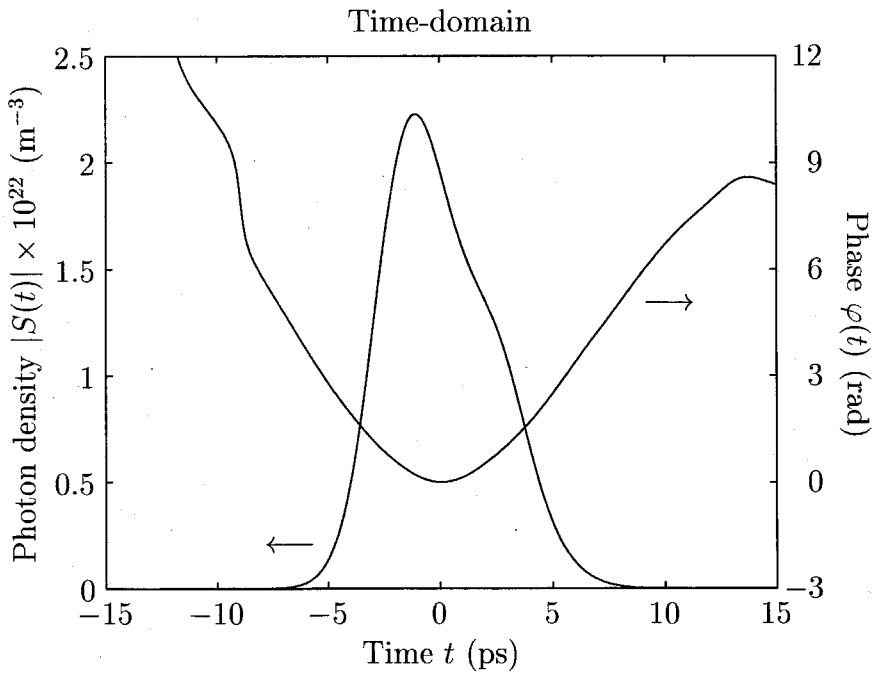


Figure 2.11: Temporal intensity $|S(t)|$ and phase $\varphi(t)$ of the pulse in steady state.

The complex pulse shape in the time-domain can be calculated according to

$$S(t) = |S(t)|\, e^{j\varphi(t)} = \left| \sum_m \sqrt{S_m(t)} \exp\{j(\omega_m - \omega_c)t + j\varphi_m(t)\} \right|^2 \tag{2.68}$$

The result is shown in Fig. 2.11. In this figure we have also shown the temporal phase $\varphi(t)$ of the pulse which has a roughly parabolic shape. The mode-locked pulse is asymmetric in time. The pulse width is $\Delta t_p \approx 7$ ps. The instantaneous frequency of the pulse is given by

$$\omega(t) = \omega_c + \frac{\mathrm{d}\varphi(t)}{\mathrm{d}t} \tag{2.69}$$

The phase over the pulse varies approximately quadratically in time. This means that the pulse contains an approximately linear temporal up-chirp, i.e., the red components are present in the leading edge of the pulse while the blue components are present in the trailing edge.

## 2.5 Spontaneous emission and its cause of timing and amplitude jitter

In this section we examine the influence of spontaneous emission on the steady state mode-lock behavior. The spontaneous emission rate has been calculated according to (2.7) in Section 2.2. The spontaneous emission causes an additional term in the photon density rate equation given by (2.57). This spontaneous emission term is given by

$$\left.\frac{\mathrm{d}S_m}{\mathrm{d}t}\right|_{sp} = \frac{W_{sp}}{V_{\mathrm{mode}}} \tag{2.70}$$

Spontaneous emission contributions come from both the gain and the absorber section but at different rates as these sections are being pumped differently. The total spontaneous emission contributions are given by

$$\left.\frac{\mathrm{d}S_m}{\mathrm{d}t}\right|_{sp} = \Gamma\zeta^g_{0,m,m}\frac{W^g_{sp}}{V_g} + \Gamma\zeta^a_{0,m,m}\frac{W^a_{sp}}{V_a} \tag{2.71}$$

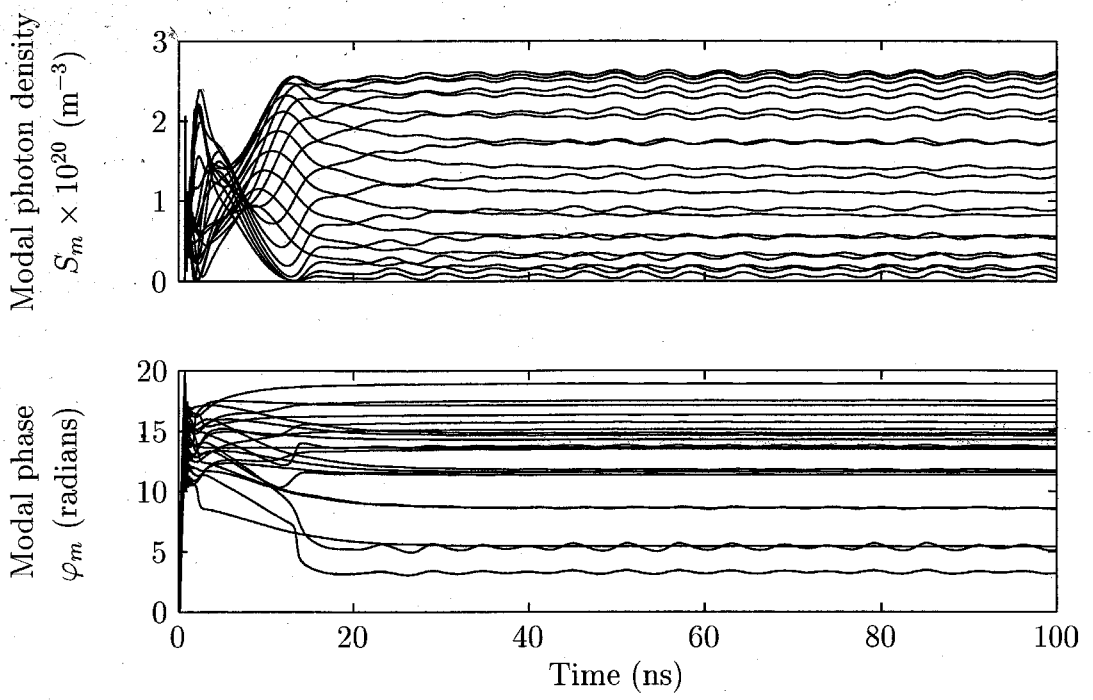


Figure 2.12: Time evolution of the photon densities $S_m$ and the phases $\phi_m$ for modal numbers $M_c - 10 \leq m \leq M_c + 10$ with $M_c = 9004$ when spontaneous emission is included.

It is noted that the contributions from the absorber are negligible compared to the gain medium as the absorber section is biased below transparency. In our simulations these contributions are however included for completeness.

We have next integrated the mode equations with the spontaneous emission terms included. The typical startup behavior is shown in Fig. 2.12. The initial mode-competition process occurs within the first few tens of nanoseconds. After this time, the mode-locked laser is in a quasi-steady state. This quasi-steady state fluctuates around the steady state calculated in the previous section due to spontaneous emission events into the lasing modes. The explanation for this is as follows: in order to maintain the steady state calculated in the previous section, the laser needs to maintain a certain amplitude and phase for each mode. For the modes at the outer ends of the spectrum, this amplitude is small. When spontaneous emission is included, the amplitude of these modes rise above the value that is needed to keep the laser in steady state due to the additional spontaneous emission terms (2.71) in (2.57). As a result the phases of these modes are also perturbed from their steady state values

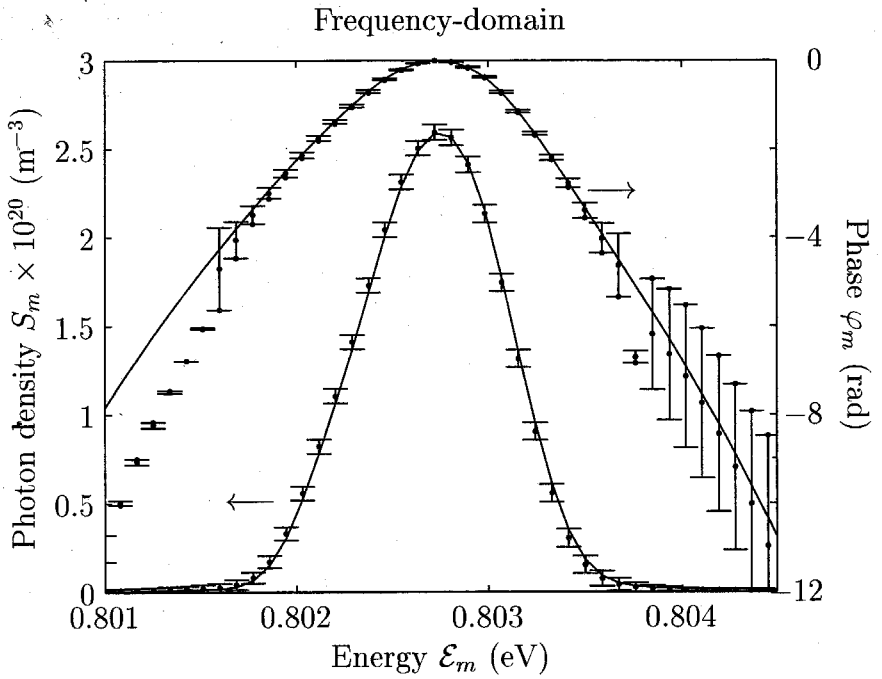


Figure 2.13: Photon density $S_m$ and phase $\varphi_m$ for each mode when spontaneous emission is included (error bars). The photon density and phase without the inclusion of spontaneous emission is shown by the solid lines.

through (2.59). Due to the fact that all modes are coupled together, the perturbation of the modes at the outer ends of the spectrum couples to all the other lasing modes as can be seen in Fig. 2.12. In Fig. 2.13 we have shown the typical fluctuations of the amplitudes and phases of the modes. The error-bars indicate the ranges in which the amplitudes and phases fluctuate when the laser is in its quasi-steady state. From Fig. 2.13 it can be seen that the phase disturbance does not couple very far into the center of the spectrum. The oscillations in the modal phases is mainly visible in the modes at the outer ends of the spectrum (the size of the error-bars decreases towards the center of the spectrum). However, the amplitude fluctuations that are caused by the spontaneous emission into the outer modes manifest themselves over the complete spectrum as can be seen from Fig. 2.13 (see the error-bars for the photon densities). It is noted again that although all modes are fluctuating in amplitude, the total photon density in the laser cavity is constant in this quasi-steady state due to the previously discussed anti-correlation of the modes.

If we consider the mode-locked laser from a time-domain point of view, the laser is

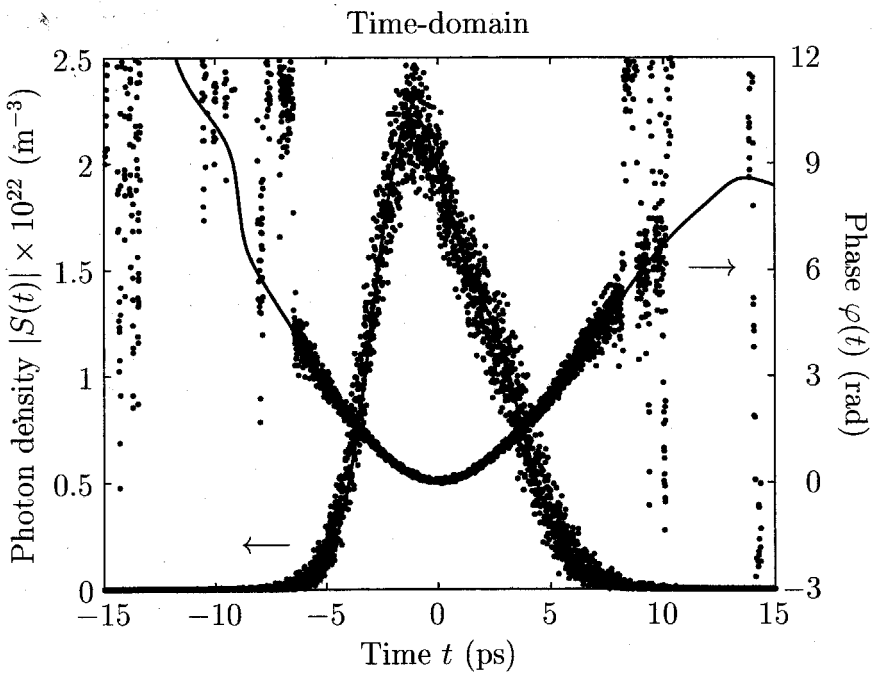


Figure 2.14: Temporal intensity $|S(t)|$ and phase $\varphi(t)$ of the pulse when spontaneous emission is included (dots). The pulse intensity and phase without the inclusion of spontaneous emission is shown by the solid lines.

not perfectly mode-locked due to spontaneous emission events. The phase fluctuations of the modes cause timing jitter of the pulse, while the amplitude fluctuations of the modes cause amplitude fluctuations in the pulse. In Fig. 2.14 we have plotted the fluctuations of the pulse over a time period of 100 ns. For comparison we have also plotted the steady-state pulse intensity and phase calculated in the previous section. Clearly visible are the timing jitter and the amplitude jitter in the intensity of the pulse. From Fig. 2.14 the relative timing jitter $\Delta T/T$ and amplitude jitter $\Delta\mathcal{E}/\mathcal{E}$ of the pulse is estimated to be

$$\frac{\Delta T}{T} = \frac{\Delta T}{2\pi/\Delta\omega} = \frac{0.5 \text{ ps}}{47.9 \text{ ps}} = 1.0\% \tag{2.72a}$$

$$\frac{\Delta\mathcal{E}}{\mathcal{E}} = \frac{0.25 \cdot 10^{22}}{2.2 \cdot 10^{22}} = 11.4\% \tag{2.72b}$$

## References

[1] W. Chow, S. Koch, and M. Sarget III, *Semiconductor-Laser Physics.* New York: Springer-Verlag, 1994.

[2] U. Herzog, "Longitudinal mode interaction in semiconductor- lasers due to nonlinear gain suppression and 4-wave- mixing," *Opt. Commun.*, vol. 82, no. 3-4, pp. 390–405, 1991.

[3] G. Agrawal, "Gain nonlinearities in semiconductor-lasers - theory and application to distributed feedback lasers," *IEEE J. Quantum Electron.*, vol. 23, no. 6, pp. 860–868, 1987.

[4] M. Asada and Y. Suematsu, "Density-matrix theory of semiconductor-lasers with relaxation broadening model - gain and gain- suppression in semiconductor-lasers," *IEEE J. Quantum Electron.*, vol. 21, no. 5, pp. 434–442, 1985.

[5] M. Asada and Y. Suematsu, "Gain and gain suppression in semiconductor-lasers," *J. Opt. Soc. Amer. B*, vol. 1, no. 3, pp. 450–451, 1984.

[6] W. Press, S. Teukolsky, W. Vetterling, and B. Flannery, *Numerical Recipes in C.* Cambridge University Press, 1992.

# CHAPTER 3

# *Applications of mode-locked lasers*

## 3.1 Introduction

In this chapter we discuss the potential of two new applications for mode-locked lasers in the field of optical communications and in the high-speed photonics area. The first application uses the frequency-domain characteristics of a mode-locked laser: each of the mode-locked modes can potentially be used as a single wavelength source in an optical communication system after the appropriate spectral filtering. A mode-locked laser with a dense mode-spacing is studied for this purpose. The second application uses the time-domain or pulse characteristics of a mode-locked laser. A photonic scheme is proposed that is able to increase the sampling speed of analog to digital (A/D) converters. The pulse trains of a number of mode-locked lasers are combined into a multi-wavelength sampling pulse train which can be used as the sampling source in an A/D converter. The combination of optics and electronics in this approach makes it possible to cross over the electronic boundaries for the sampling speed of conventional A/D converters. The photonic A/D converter combines wavelength multiplicity and optical short pulse generation in such a way that it becomes possible to digitize high-end microwave signals with conventional state-of-the-art A/D converters in a parallel fashion.

## 3.2 An optical source for wavelength division multiplexing (WDM)

Wavelength division multiplexing (WDM) is becoming increasingly important in current optical communication systems. WDM systems utilize the large bandwidth of

an optical fiber very efficiently by launching multiple closely spaced optical channels into a single fiber, each modulated at high bit-rates. In order to have accurate control over the wavelength of every channel simultaneously, it is advantageous to generate all of the wavelengths at one central node in the network and provide the capability to modulate them at each network node [1]. As a result, one of the key components of a WDM system is a stable and controllable multi-wavelength laser source.

One of the earliest designs for a WDM multi-wavelength source uses a discrete DFB laser for every channel [2]. However, this type of setup is highly cost inefficient and channel spacing control is poor. Every DFB lasers needs to be accurately temperature stabilized in order to keep its absolute wavelength within specifications. Monolithically integrated multi-wavelength lasers have better potential as a stable and controllable source. A multi-frequency laser with a waveguide grating router as an intra-cavity element to lock all wavelengths at a specifically determined channel spacing of 200 GHz has been demonstrated [3].

As an alternative to using an array of external or monolithic lasers, spectral slicing of devices with a broad optical emission spectrum, for example light emitting diodes [4] or semiconductor optical amplifiers [5], has been proposed. Also, amplification of the spontaneous emission from a Fabry-Pérot (FP) laser biased below threshold has been demonstrated [6]. The emission spectrum of this type of device consists of a large number of modes whose spacing is constant and determined by the FP cavity length. After amplification of the spectrum, every mode can be used as a separate WDM channel. Stabilization or adjustment of the channel-spacing without modifying the center wavelength of the laser is complicated however. Multiple wavelengths can also be generated using super-continuum (SC) generation in optical fibers [7]. The SC pulse generator outputs spectrally super-broadened, short optical pulses. A very large number of WDM channels can be sliced out of this extremely broad spectrum.

Another promising design of a multi-wavelength source incorporates a mode-locked semiconductor laser [8, 9]. In analogy to the FP laser below threshold, the light output of a mode-locked laser consists of many optical modes whose spacing is determined by the cavity length. In contrast to the FP laser, the modes are locked by an intra-cavity

saturable absorber and do not need pre-amplification. Applying an RF signal to the saturable absorber section of the laser makes the channel spacing temperature independent and very stable. Absolute wavelength control can be achieved by temperature tuning or incorporation of Bragg reflectors inside the cavity [10, 11]. Fine-tuning of the channel spacing can be achieved by slightly detuning the RF modulation frequency from the cavity repetition rate. Simultaneous demultiplexing of all channels using an arrayed waveguide grating filter with a channel spacing of 100 GHz has been demonstrated [9]. In the next section we examine the potential of a mode-locked laser with a dense mode spacing ($\sim$ 25 GHz) as a WDM source.

### 3.2.1 WDM mode-locked laser source

A schematic drawing of our mode-locked semiconductor laser is shown in Fig. 3.1. The active layer consists of four quantum wells, grown by metal organic chemical vapor deposition (MOCVD). The device is a buried heterostructure using reverse biased junctions as current confining layers, grown by liquid phase epitaxy (LPE). The cavity is split up into two sections. The length of the absorber section is 110 $\mu$m long while the length of the gain section is approximately 1900 $\mu$m. The total device length is 2010 $\mu$m while the isolation region between the gain and absorber section is approximately 15 $\mu$m. Electrical isolation between the two sections is 1.5 k$\Omega$. No coatings are applied to the end facets of the laser.

In order to make the absorber section suitable for high frequency modulation, the parasitic capacitance of this section needs to be minimized. This can be done by insulating blocking layers around the active region [12], and isolation channels with a thick polyimide deposition [13]. We use a different method. An isolated narrow mesa is formed by etching a pair of channels along the active region. This reduces the capacitance caused by the reverse-biased blocking layers. A standard $SiO_2$ layer is deposited on top to isolate the contact. An air-bridge contact configuration has been used to provide the electrical contact to the absorber section [14]. This further reduces the parasitic capacitance caused by the metal/$SiO_2$/semiconductor interface. The air-

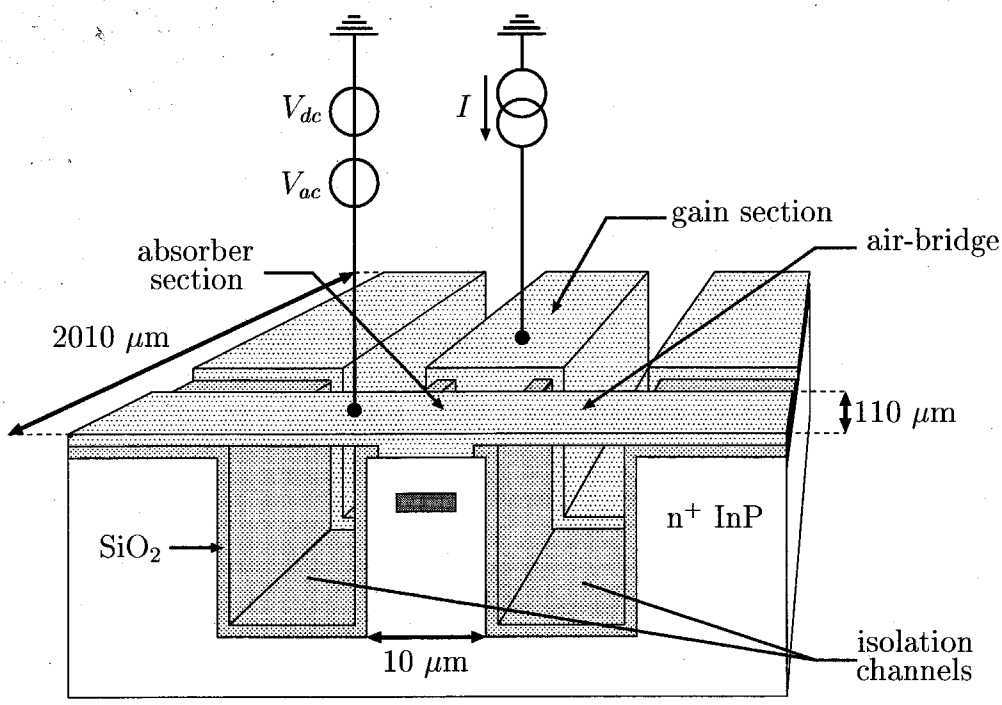


Figure 3.1: Schematic view of the mode-locked laser, showing the isolated mesa, air-bridge and gain and absorber sections.

bridge contact has been fabricated using the standard photolithographic process and thick gold metallization.

The complete laser structure has been mounted on a custom high frequency mount consisting of a K-connector and 50 Ω micro-strip. This mount allows RF modulation frequencies up to 35 GHz. The laser is not impedance matched to the micro-strip. The threshold current for the laser with both the gain and absorber section forward biased by a current source is 35 mA. In Fig. 3.2 we have shown a few typical LI-curves as a function of the gain current with the absorber voltage as a parameter. The absorber voltage ranges from 1 V to $-1$ V in steps of 200 mV. The modulation response (see Fig. 3.3) is measured using a high-speed photo-detector and a network analyzer. The absorber is biased at $V_a = -0.26$ V and the gain section is pumped at $I_g = 130$ mA for this measurement. The mode-lock frequency or cavity resonance peak occurs around 21.7 GHz.

We next examine the dependence of the mode-lock frequency on biasing conditions. The laser is passively mode-locked for this purpose and its cavity resonance

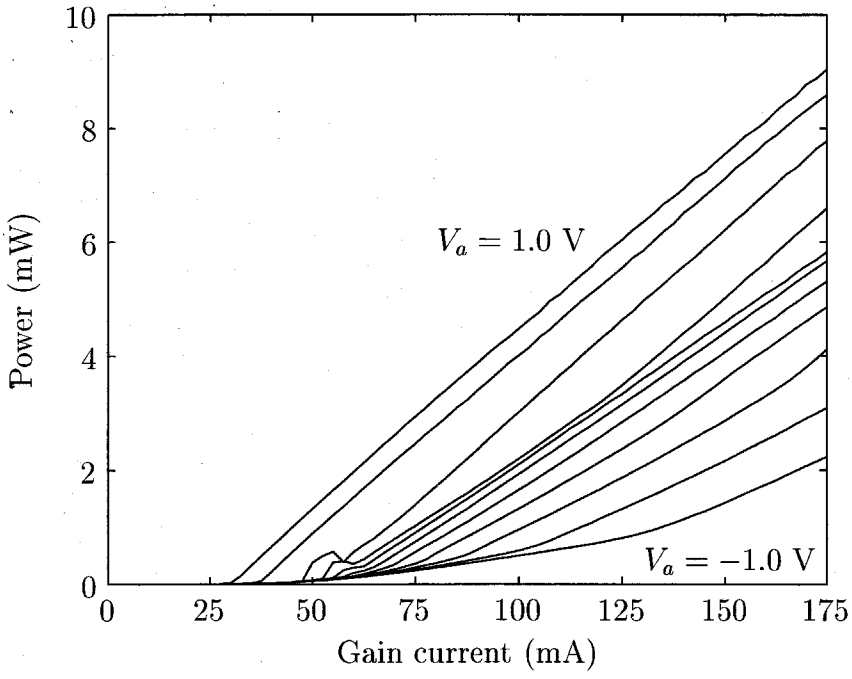


Figure 3.2: Output power of the mode-locked laser as a function of the gain current $I_g$ with the absorber voltage $V_a$ as a parameter. The absorber voltage is changed from 1 V to $-1$ V in steps of 200 mV.

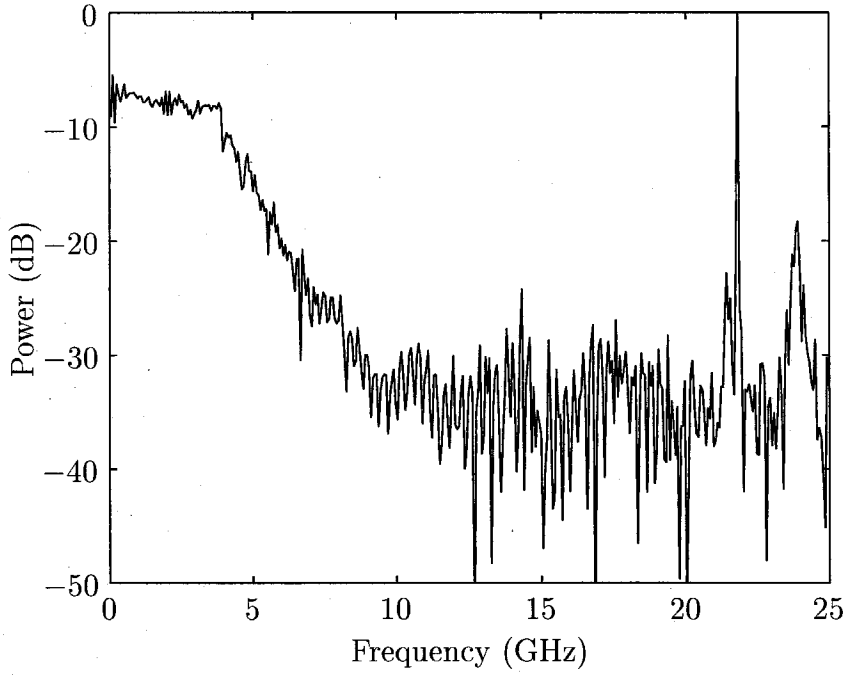


Figure 3.3: Modulation response of the air-bridge type mode-locked laser. The cavity resonance peak occurs around 21.7 GHz.

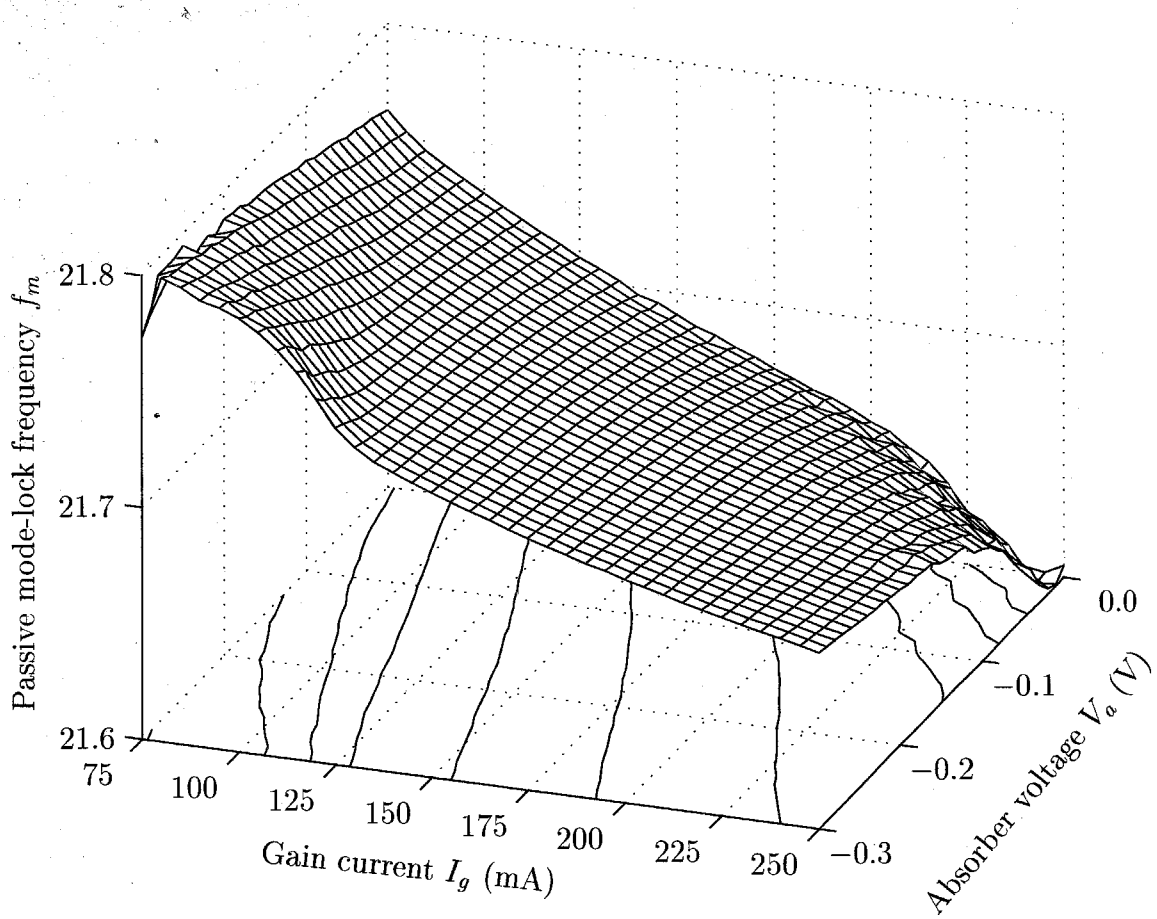


Figure 3.4: Cavity resonance frequency as a function of the gain current $I_g$ and the absorber voltage $V_a$.

is measured using a high-speed photo-detector and an electrical spectrum analyzer (ESA). The gain current $I_g$ is varied from 75 mA to 250 mA in steps of 5 mA. The absorber voltage $V_a$ is varied from 0.0 V to -0.3 V in steps of 10 mV. The results are shown in Fig. 3.4. We have also drawn a number of contour lines in this plot. From Fig. 3.4 we can see that we can change the mode-lock frequency continuously from 21.6 GHz to 21.8 GHz by changing the gain current and the absorber voltage. This means that the channel spacing of our WDM source can be fine-tuned over a range of approximately 200 MHz by changing biasing conditions.

The laser is next actively mode-locked by applying an RF signal to the absorber section. The gain current is set to $I_g = 250$ mA and the absorber voltage to $V_a = -0.22$ V. The mode-lock frequency for these settings equals $f_m = 21.669$ GHz. We

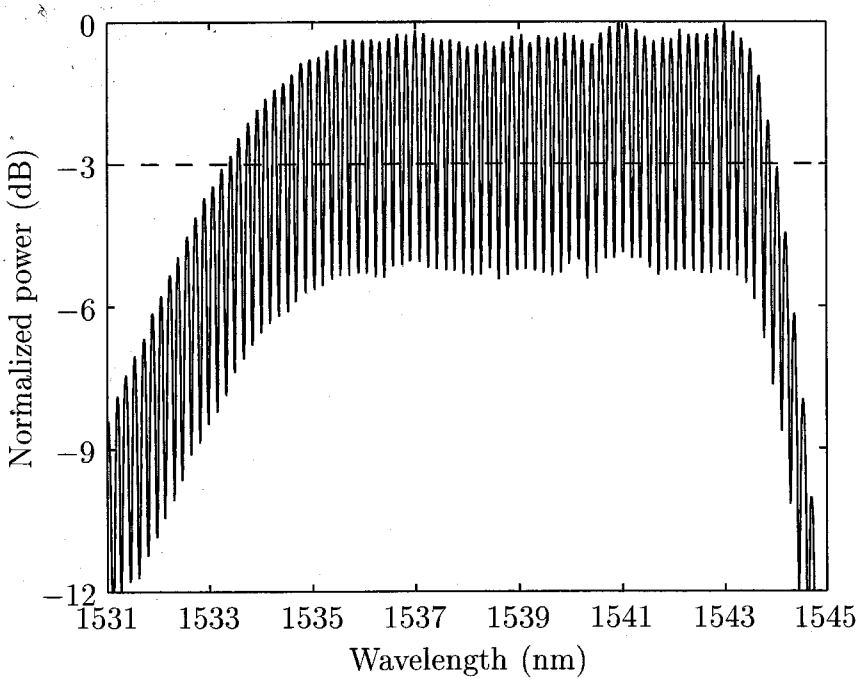


Figure 3.5: Spectrum of the mode-locked laser source. The flat-top spectrum contains 62 modes within its 3 dB spectral width.

next adjust the power level of the RF source such that we get a flat-top and broad spectrum of locked modes. The spectrum is measured with an optical spectrum analyzer (OSA) with a resolution bandwidth of 0.08 nm. The result is shown in Fig. 3.5. Under the given biasing conditions a nice broad and flat-top spectrum of our laser is obtained. The 3 dB width of the spectrum is approximately 10.5 nm and contains 62 locked modes.

We next examine whether the mode-locked modes are suitable for high-speed data transmission. In order to do this we need to separate one of the modes from the total mode-locked spectrum shown in Fig. 3.5. In Fig. 3.6 we have shown the wavelength "dropping" method to split off one of the modes from the mode-locked laser. The light from the laser is coupled into a fiber, passes through a circulator and then hits a fiber Bragg grating. The WDM channel of interest that needs to be dropped is reflected off the Bragg grating back to the circulator where it is "dropped" from the fiber. All of the other WDM channels are available at the output of the fiber Bragg grating and can succeedingly be dropped in a similar way. Note that the circulator

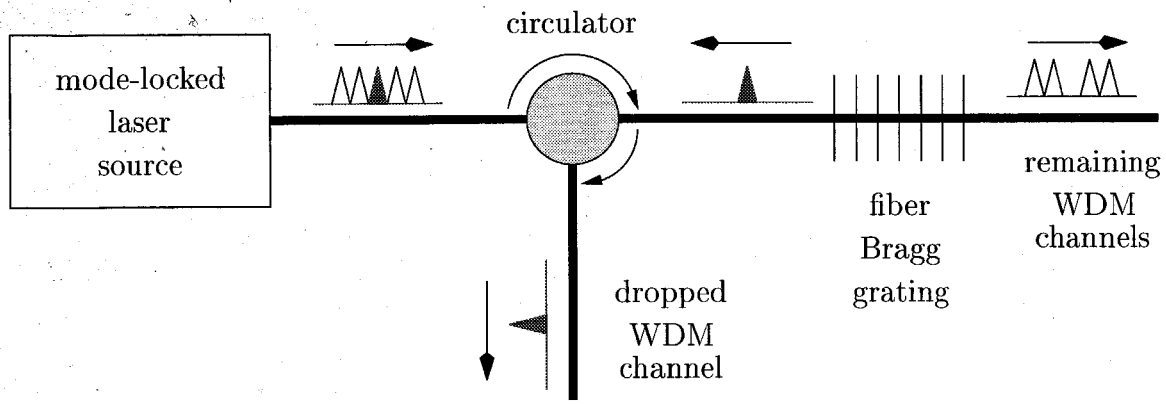


Figure 3.6: The WDM single wavelength setup incorporating a multi-wavelength mode-locked laser source and a fiber Bragg grating/circulator based drop filter.

introduces a loss of around 1 dB for each of the channels that are not dropped and an additional loss of 1 dB for the dropped channel. This loss may be avoided by replacing the combination of the circulator and the fiber Bragg grating by a lossless add/drop filter such as the filter described in [15]. The transmission characteristics of the fiber Bragg grating are shown in Fig. 3.7. The center wavelength of the fiber Bragg grating is around 1536 nm, the peak reflectivity is 80% and the full width at half maximum (FWHM) of the grating is 0.5 Å ($\sim$ 7 GHz). The total length of the grating is 21 mm.

In order to have the wavelength of one of the channels coincide with the center wavelength of the Bragg grating, we physically stretch the grating so that its reflection peak is tuned to one of the channels. With the grating tuned to the selected channel, we measure the spectral characteristics of the dropped WDM channel. The result is shown in Fig. 3.8. Trace (a) shows the complete mode-locked spectrum (all channels). Trace (b) shows the dropped channel and trace (c) shows the spectrum of the remaining modes after dropping (exiting the grating). The inset shows the spectrum of the dropped channel taken by an OSA with a resolution bandwidth of 0.01 nm. The side-mode suppression of the nearest neighboring modes is 19 dB. From trace (c) one can see that the channel is not fully dropped due to the fact that the peak reflectivity of the grating is only 80%. A stronger grating can improve this at the cost of a wider passband and thus less side-mode suppression, assuming that the

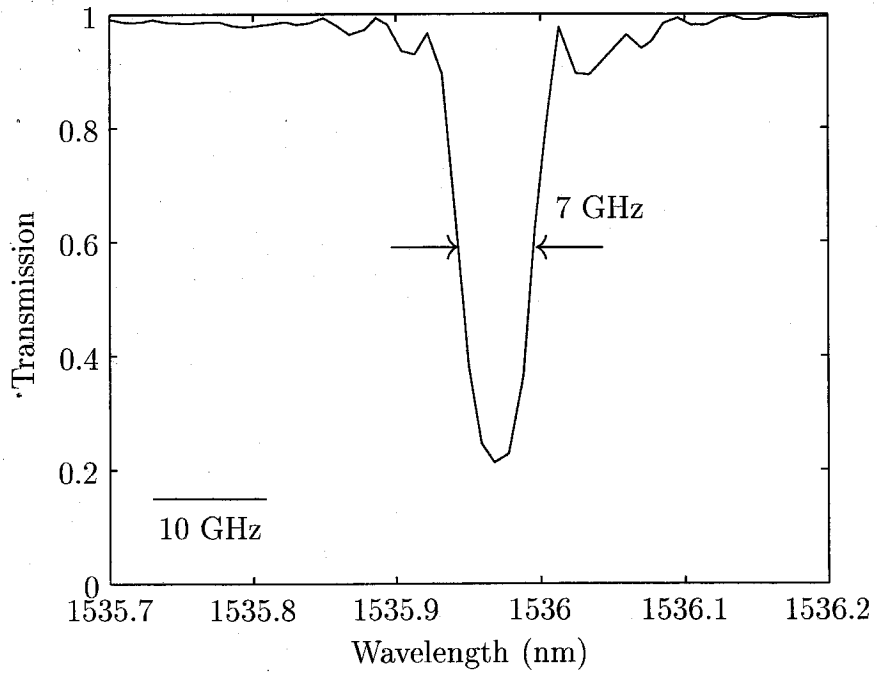


Figure 3.7: Transmission characteristics of the fiber Bragg grating used in the setup of Fig. 3.6.

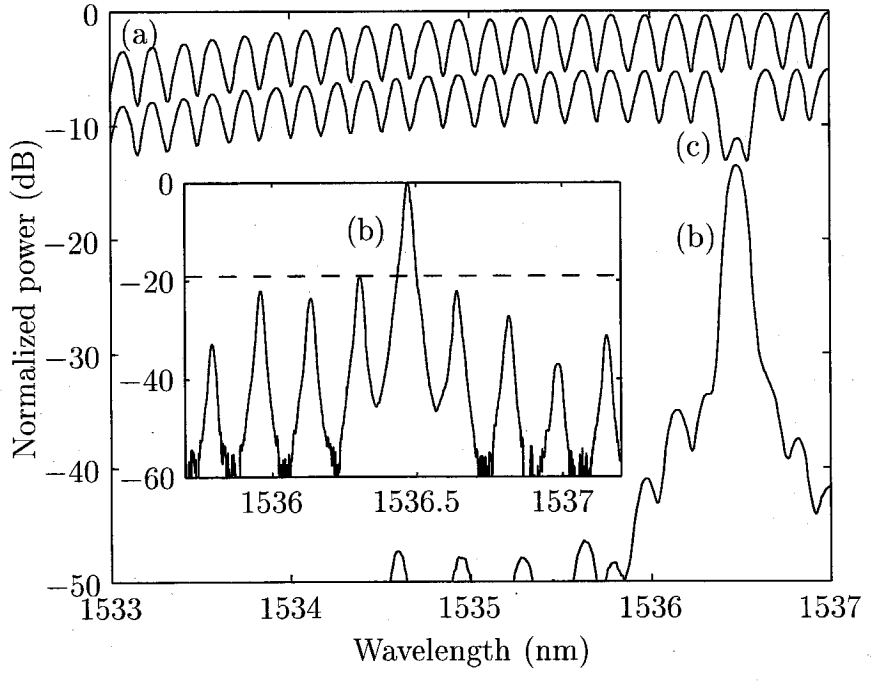


Figure 3.8: Spectrum of the WDM mode-locked laser source: complete mode-locked spectrum (a), a single channel filtered out by a fiber Bragg grating (b) and the remaining channels (c). The inset shows a higher resolution trace of the dropped channel.

grating can not be made any longer than 21 mm.

We have next examined the transmission capabilities of the dropped channel. The setup for the measurement of a bit error rate (BER) for the channel is given in Fig. 3.9. The dropped channel is boosted by an erbium doped fiber amplifier (EDFA) and next modulated with real-time date by an external electro-optic modulator (EOM) driven by the BER pattern generator. At the receiver 10% of the signal is tapped off for monitoring purpose on an OSA and the remaining 90% of the signal can be variably attenuated. The attenuated signal is bandpass filtered by a tunable FP filter with a 0.5 nm FWHM bandwidth and is next amplified by a low-noise EDFA. The resulting amplified signal is then again bandpass filtered by a 0.5 nm FP filter to limit the spontaneous emission from the EDFA. The signal is next detected by a high-speed photo-detector, electrically amplified and filtered and fed back to the BER tester for determination of the error rate as a function of the received optical power.

Even though the side mode suppression for the WDM channel is 19 dB, which should be more than sufficient for "error free" data transmission, we have not been able to achieve "error free" data transmission, even without fiber in the transmission path. "Error free" data transmission here means that a bit error rate smaller than $10^{-10}$ can be achieved. In order to find out what the reason is for this poor performance, we have performed a noise analysis of our device. In the next section we both examine the noise properties of the multi-wavelength mode-locked laser source as well as of the single channel WDM source.

### 3.2.2 *Noise properties*

We start this section by examining the stability of the pulse train. For this purpose we detect the pulse train with a high-speed photo-detector. The signal from the photo-detector is amplified by an electrical amplifier and succeedingly spectrally analyzed with an ESA. The measured power spectrum consists of a number of carriers at harmonics of the pulse repetition rate ($\sim$ 21.7 GHz). Due to the limited response of the photo-detector and electrical amplifier only the fundamental and second harmonic

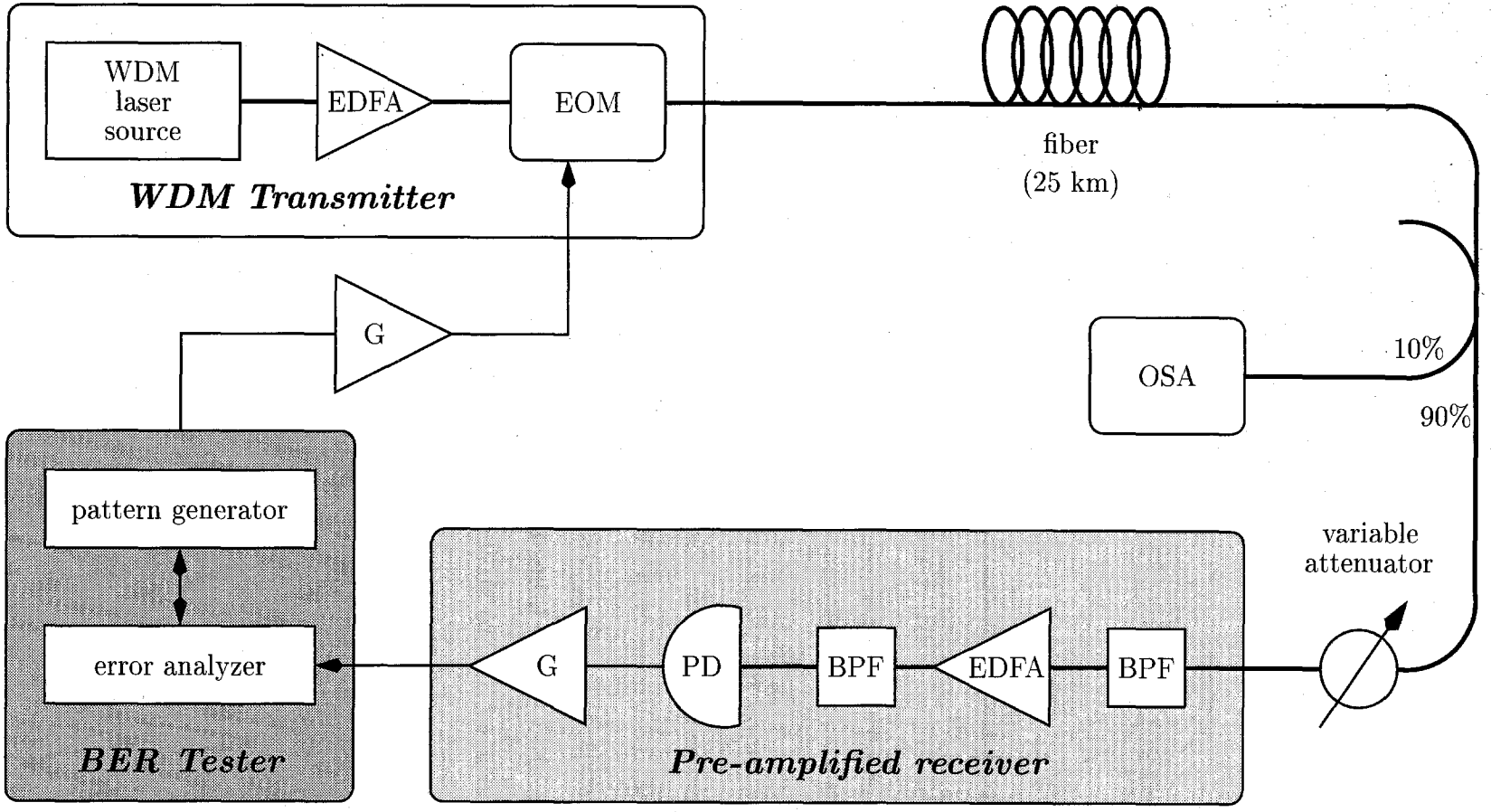


Figure 3.9: Measurement setup for the determination of the BER performance of a WDM transmitter. EOM: electro-optic modulator, EDFA: erbium doped fiber amplifier, G: electrical amplifier, BPF: bandpass filter, PD: photo-detector, OSA: optical spectrum analyzer.

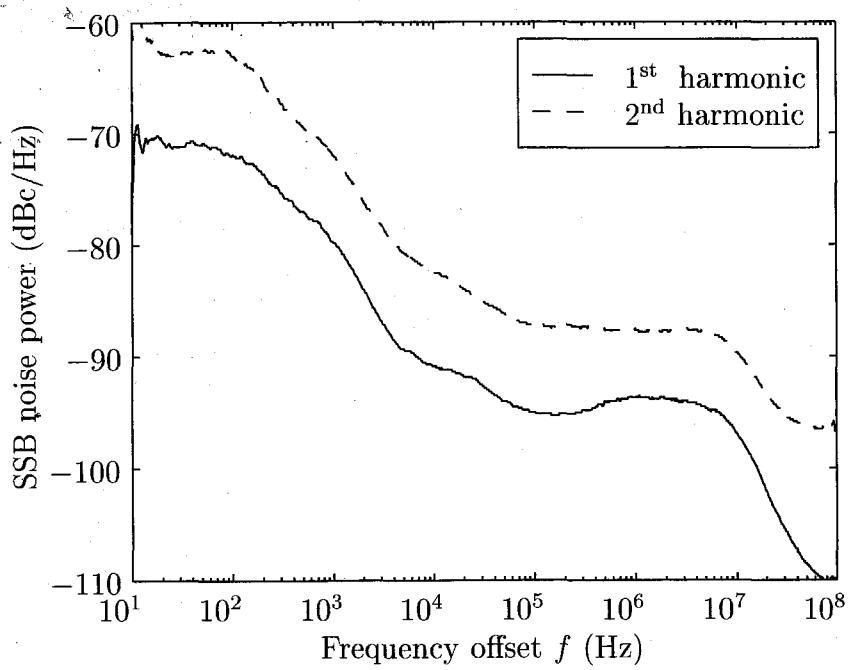


Figure 3.10: SSB power spectrum of the pulse train around the fundamental harmonic carrier ($n = 1$, solid line) and the second harmonic carrier ($n = 2$, dashed line).

(although close to the measurement background noise level) can be detected. Around this fundamental carrier the phase and amplitude noise bands appear corresponding to timing and amplitude jitter respectively. We have measured the single-sideband (SSB) noise for an evaluation of the timing jitter. Fig. 3.10 shows the SSB noise versus the frequency offset $f$ from the fundamental 21.669 GHz carrier frequency (solid curve) and the second harmonic 43.338 GHz carrier frequency (dashed line). The laser biasing conditions are chosen as $I_g = 250$ mA and $V_a = -0.22$ V. The SSB noise power is measured over the frequency offset range 10 Hz $\leq f \leq$ 100 MHz. According to [16, 17] the root mean square (RMS) timing jitter $\Delta T$ over a frequency band $f_{\min} \leq f \leq f_{\max}$ is given by

$$\frac{\Delta T}{T} = \frac{1}{2\pi n}\sqrt{2\int_{f_{\min}}^{f_{\max}} S_P(f)\,\mathrm{d}f} \tag{3.1}$$

where $T$ is the pulse repetition time, $n$ is the harmonic number of the carrier that is being measured and $S_P(f)$ is the ratio of the SSB phase noise power spectral density

to the carrier power. The RMS pulse energy fluctuation $\Delta\mathcal{E}$ can be found similarly from

$$\frac{\Delta\mathcal{E}}{\mathcal{E}} = \sqrt{2\int_{f_{\min}}^{f_{\max}} S_A(f)\,\mathrm{d}f} \tag{3.2}$$

where $\mathcal{E}$ is the pulse energy and $S_A(f)$ is the ratio of the SSB amplitude noise power spectral density to the carrier power.

As will become clear later on, the phase noise in Fig. 3.10 is much stronger than the amplitude noise for frequencies up to 25 MHz. Integration of the SSB phase noise power in Fig. 3.10 for 10 Hz $\leq f \leq$ 25 MHz gives the timing jitter $\Delta T/T$. Integration for the first harmonic curve gives $\Delta T/T = 1.56\%$ and integration of the second harmonic curve gives $\Delta T/T = 1.77\%$. Both values agree very well with each other. It is noted that the noise power for the second harmonic fails to drop off for frequencies higher than 25 MHz. This is due to the fact that this measurement is made close to the measurement background noise level. As a result the timing jitter value resulting from this measurement is estimated to be on the high side. It is noted that the frequency range in Fig. 3.10 does not extend far enough to get an estimate for the amplitude jitter $\Delta\mathcal{E}/\mathcal{E}$ using (3.2). We will use a different method to estimate this amplitude jitter later on.

First, in order to confirm the results above we have made a few more measurements of the jitter as described next. Following [16] the pulse timing jitter and amplitude jitter are related to the ratio of their respective noise band powers $P_J$ and $P_A$ to the carrier peak power $P_C$ of the $n^{\text{th}}$ harmonic by

$$\frac{\Delta T}{T} = \frac{1}{2\pi n}\sqrt{\left(\frac{P_J}{P_C}\right)_n \frac{\Delta f_J}{\Delta f_{\text{res}}}} \tag{3.3a}$$

$$\frac{\Delta\mathcal{E}}{\mathcal{E}} = \sqrt{\left(\frac{P_A}{P_C}\right)_{n=0} \frac{\Delta f_A}{\Delta f_{\text{res}}}} \tag{3.3b}$$

where $\Delta f_A$, $\Delta f_J$ and $\Delta f_{\text{res}}$ are the amplitude noise bandwidth, the timing jitter bandwidth and the resolution bandwidth for the measurement respectively.

For the measurement of the timing jitter, the RF power spectrum of the funda-

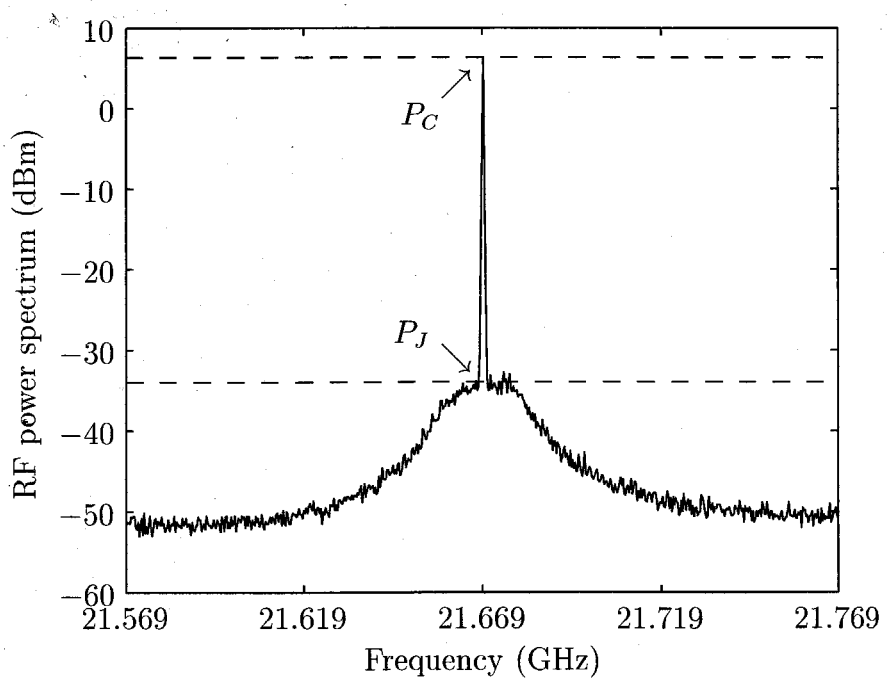


Figure 3.11: RF power spectrum of the pulse train around the fundamental harmonic ($n = 1$) carrier at a span of 200 MHz and a resolution bandwidth of 300 kHz.

mental harmonic ($n = 1$) is shown in Fig. 3.11. We have used a span and resolution bandwidth of 200 MHz and 300 kHz respectively. With $P_J/P_C = 8.2 \cdot 10^{-5}$ (−40.8 dB) and $\Delta f_J = 25$ MHz we find $\Delta T/T = 1.32\%$. We have also measured the RF power spectrum of the second harmonic ($n = 2$), as shown in Fig. 3.12. The span and resolution bandwidth are set to 100 MHz and 300 kHz respectively for this case. With $P_J/P_C = 4.3 \cdot 10^{-4}$ (−33.7 dB) and $\Delta f_J = 24$ MHz we find $\Delta T/T = 1.48\%$. Both values are in close agreement with each other and also with the result obtained from the integration of the SSB noise power of Fig. 3.10. Averaging all four calculated values gives an average timing jitter of $\overline{\Delta T}/T \approx 1.53\%$. With a pulse round-trip time of $T = 46$ ps this gives an average timing jitter of $\overline{\Delta T} = 700$ fs.

When the timing jitter is assumed to be small (which is the case for our laser), the energy fluctuation can be approximated by [18]

$$\frac{\Delta \mathcal{E}}{\mathcal{E}} \approx \sqrt{\left(\frac{P_A}{P_C}\right)_{n=1} \frac{\Delta f_A}{\Delta f_{\text{res}}}} \tag{3.4}$$

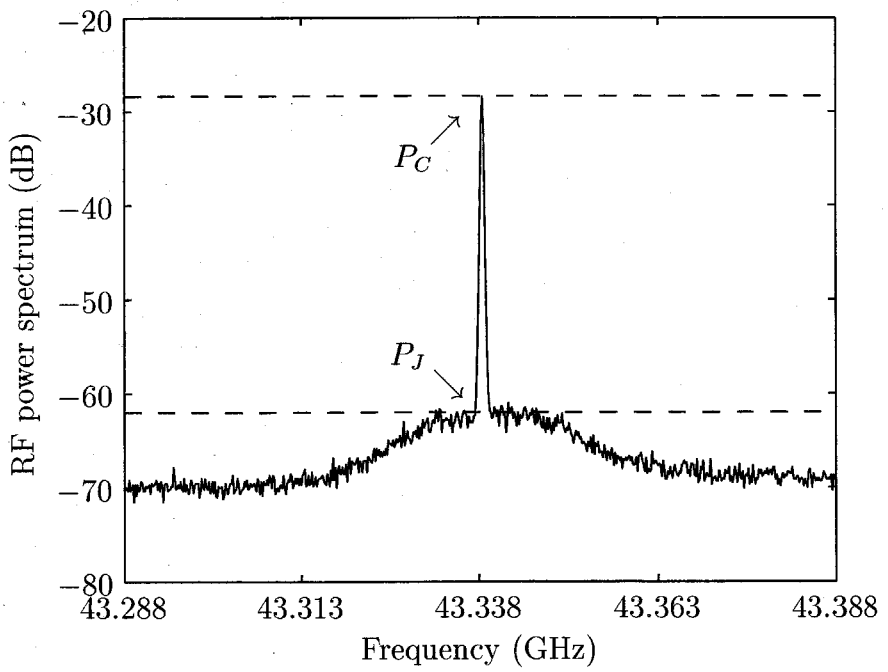


Figure 3.12: RF power spectrum of the pulse train around the second harmonic ($n = 2$) carrier at a span of 100 MHz and a resolution bandwidth of 300 kHz.

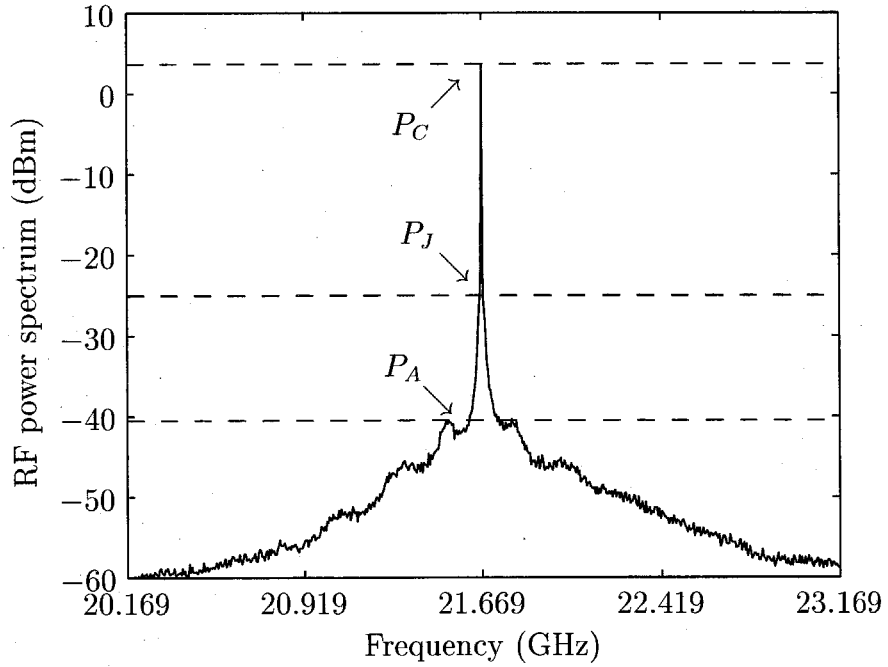


Figure 3.13: RF power spectrum of the pulse train around the fundamental harmonic ($n = 1$) carrier at a span of 3 GHz and a resolution bandwidth of 2 MHz.

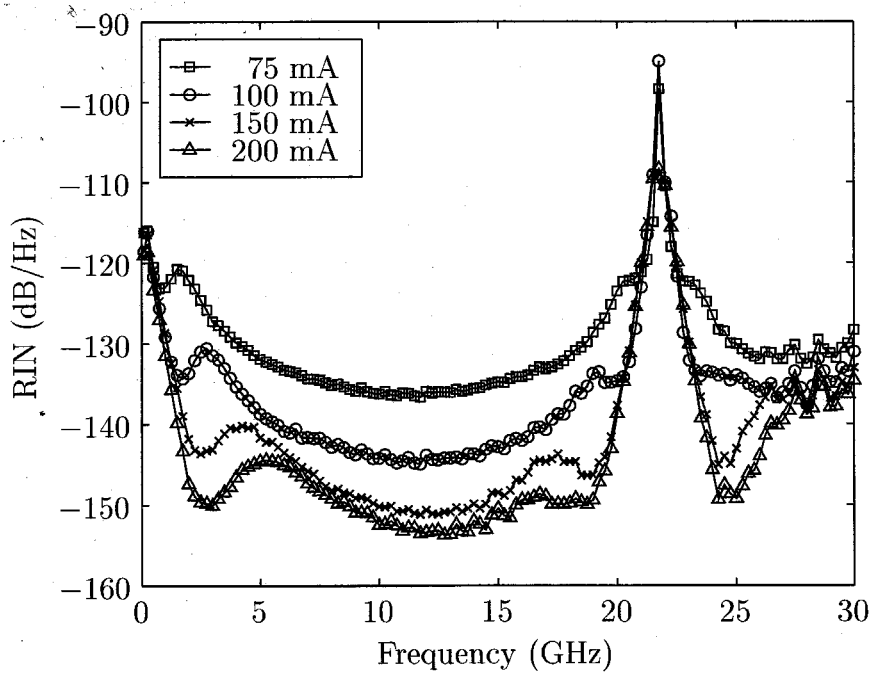


Figure 3.14: RIN spectrum of the actively mode-locked laser for $V_a = -0.2$ V with the gain current $I_g$ as a variable.

In order to estimate the amplitude jitter of the laser, we have measured the RF power spectrum of the fundamental harmonic ($n = 1$) on a wider span. The result is shown in Fig. 3.13. The span and the resolution bandwidth for this measurement are set to 3 GHz and 2 MHz respectively. With $P_A/P_C = 3.8 \cdot 10^{-5}$ (−44.2 dB) and $\Delta f_A = 370$ MHz we obtain $\Delta\mathcal{E}/\mathcal{E} = 8.4\%$. This value is very high and indicates that even though the timing jitter is small, the amplitude variations are not. This means that there are large fluctuations in the photon density of each mode over time. In order to investigate how bad these fluctuations are, we have measured the relative intensity noise (RIN) of the mode-locked laser. The RIN spectrum as a function of the gain current for an absorber voltage $V_a = -0.2$ V is shown in Fig. 3.14. The relaxation oscillation frequency can be clearly distinguished in Fig. 3.14 as well as two noise bands around $f = 0$ Hz and $f = 21.7$ GHz. The noise band around $f = 0$ Hz represents the amount of pulse amplitude jitter and the noise band around 21.7 GHz contains both amplitude and timing jitter contributions.

The RIN spectrum as a function of the absorber voltage for a gain current of

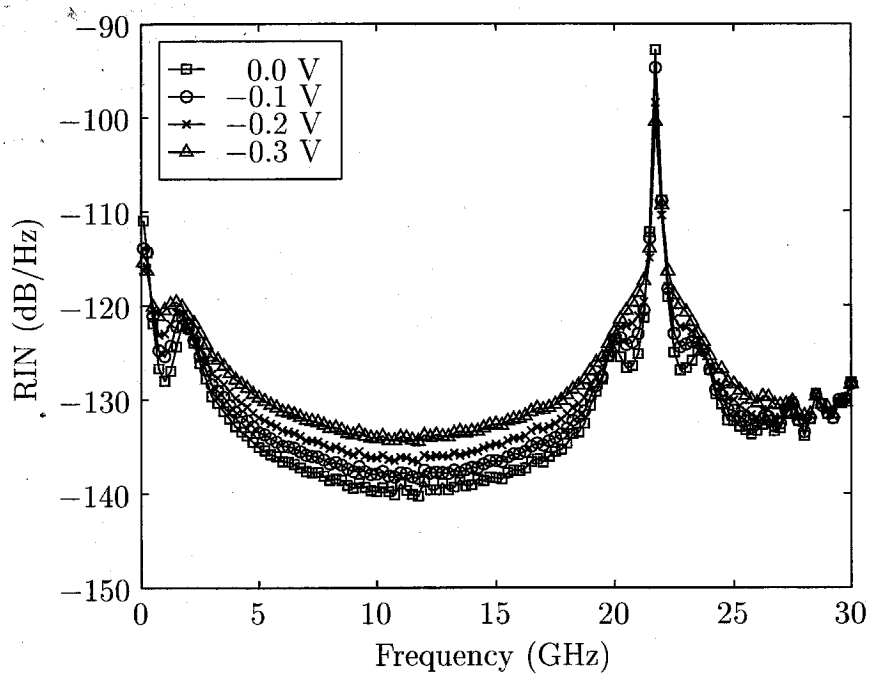


Figure 3.15: RIN spectrum of the actively mode-locked laser for $I_g = 75$ mA with the absorber voltage $V_a$ as a variable.

$I_g = 75$ mA is shown in Fig. 3.15.

The dependence of the RIN on absorber voltage is only significant for low gain currents. For gain currents greater than 150 mA the RIN dependence on absorber voltage becomes indistinguishable. It is noted that the RIN increases when the saturable loss increases (more negative absorber voltage). This is in agreement with the theoretical predictions made in [19]. For a detailed discussion on the influence of nonlinear gain and absorption on the intensity noise of a multi-mode semiconductor laser the reader is referred to [19]. It is noted that the measured levels of RIN are low enough to perform an "error free" BER measurement.

We next measure the RIN spectrum of the single wavelength WDM channel after dropping it from the total mode-locked laser output with the setup of Fig. 3.6. The result is shown in Fig. 3.16. For comparison we have displayed the RIN spectrum of the actively mode-locked laser (all modes) in this plot as well. The biasing conditions for this measurement are $I_g = 200$ mA and $V_a = 0.0$ V. We notice a very large increase in the RIN indicating that the amount of amplitude jitter has increased enormously.

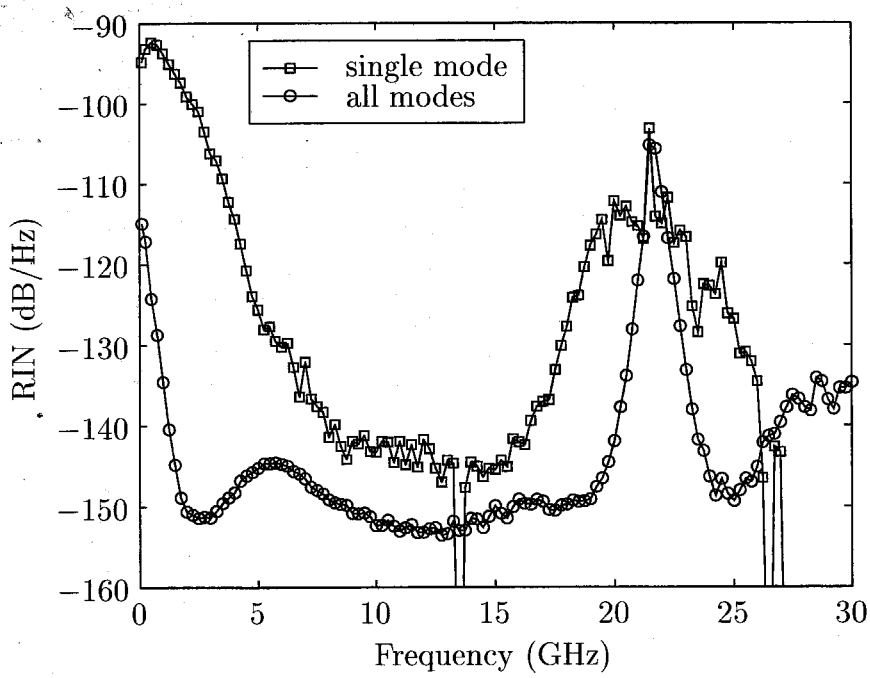


Figure 3.16: RIN spectrum of the actively mode-locked laser (all modes) and of a single WDM channel (dropped channel). The biasing conditions are $I_g = 200$ mA and $V_a = 0$ V.

This large amount of amplitude jitter in the amplitude of the single WDM channel makes it impossible to obtain an "error free" BER measurement.

The increase in noise can be explained as follows. The RIN for the mode-locked laser containing all modes is made up of the total of contributions from each mode. In Chapter 2 we have found that the fluctuations in the the mode-amplitudes are coupled due to the ongoing mode-competition in the presence of spontaneous emission. If the amplitude in the main mode increases, then the total amplitude of all the other modes decreases. This is also called anti-correlation of the mode-partition noise [19]. Adding up these anti-correlated noise powers for all modes results in a total noise power for the total intensity which is lower than the noise power for a single mode. Or in other words, the mode-partition noise of one mode is perfectly anti-correlated with the mode-partition noise in the collection of the rest of the modes. Therefore, the mode-partition noise is canceled in the total intensity noise. By filtering one mode out of the spectrum, the near perfect anti-correlation in the noise is destroyed and the measured RIN is significantly increased as shown in Fig. 3.16. For our laser this

increase is very large due to the fact that our laser has a dense mode-spacing and thus many modes ($> 62$) are competing and constantly exchanging power between each other, i.e., the laser is in a quasi-steady state. For more details on this quasi-steady state and its cause, the reader is referred to the simulations carried out in Section 2.5.

### 3.2.3 *Discretely tunable single mode operation through external feedback*

As we have seen in the previous sections, we have not managed to use the mode-locked laser as a multi-wavelength WDM source due to high mode-amplitude fluctuations. In this section we will use the mode-locked laser in an external feedback configuration and examine its potential as a discretely tunable single wavelength WDM source. The feedback is provided by the same grating used in the previous section. The measurement setup is shown in Fig. 3.17. The narrow band fiber Bragg grating ($\sim$ 7 GHz) reflects 80% of the laser light at its Bragg wavelength. The remaining 20% is coupled out of the compound cavity and is used as an output. The fiber Bragg grating is placed on a mechanical stretcher so that it is possible to adjust the Bragg wavelength. For this measurement we bias the gain section of the laser at $I_g = 200$ mA and the absorber section at $V_a = 0.9$ V. We apply an RF signal at a frequency $f_m = 21.722$ GHz to the absorber section of the laser. We next measure the RF power spectrum of the laser without feedback with the RF signal turned off and on respectively. The results are shown in Fig. 3.18. From Fig. 3.18 we see that the spacing between the modes of the laser is locked to the frequency of the RF modulation signal when this signal is turned on. When the RF signal is turned off, the laser runs freely and the cavity resonance frequency is determined by the cavity length. The RF modulation frequency is detuned by about 3 MHz from the cavity resonance of the free running laser.

Without the proper tuning of the fiber Bragg grating to one of the monolithic cavity modes, a multi-mode spectrum is obtained. By tuning of the grating such that its Bragg wavelength coincides with one of the modes of the monolithic cavity, single mode lasing operation is achieved at the particular mode the grating is tuned to. The

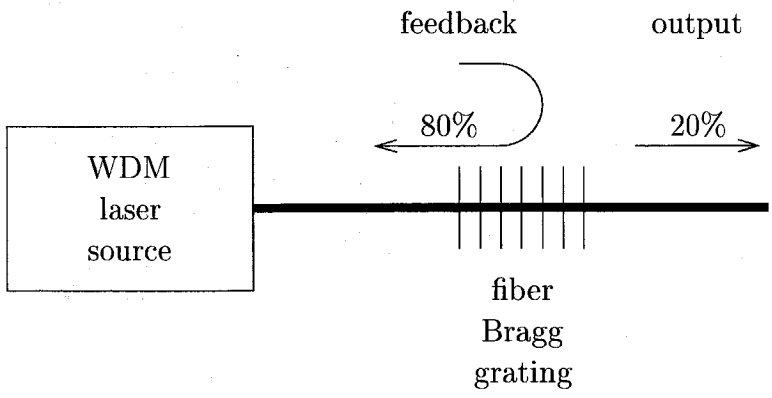


Figure 3.17: Measurement setup for the discretely tunable single wavelength WDM source.

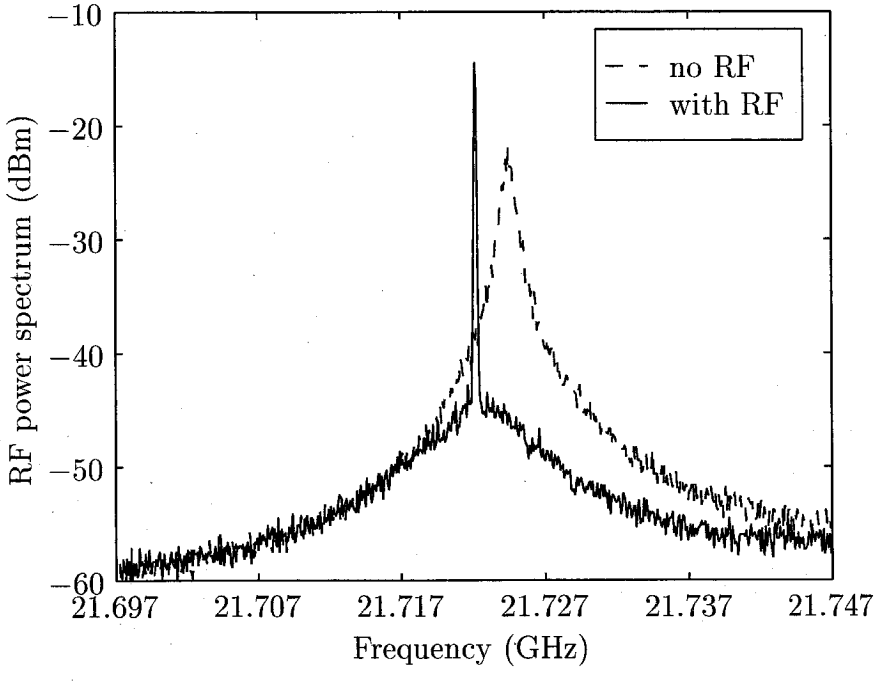


Figure 3.18: RF power spectrum of the laser without feedback when the RF modulation signal is turned off (dashed line) and when the RF modulation signal is turned on (solid line).

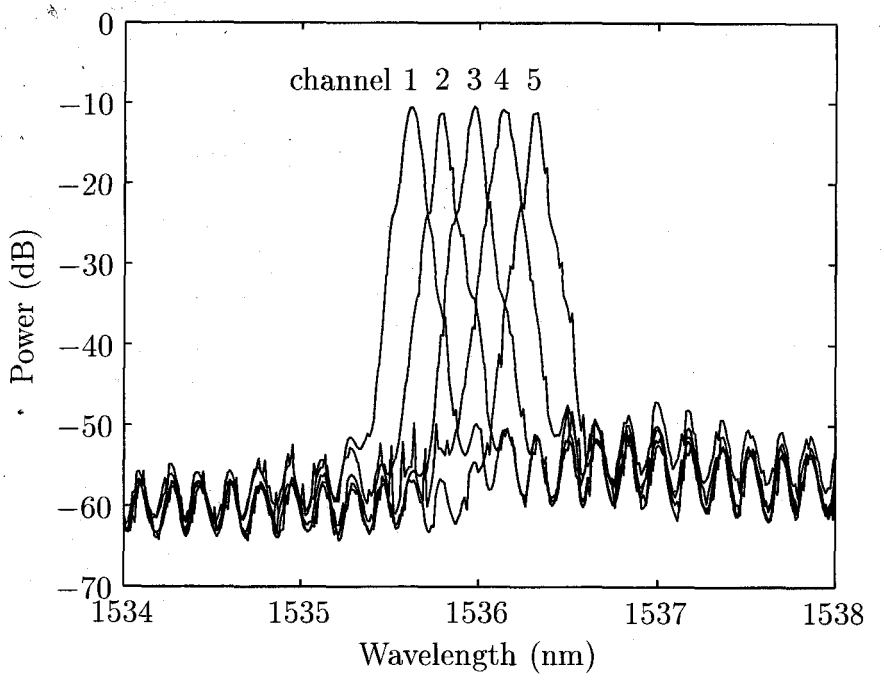


Figure 3.19: Optical spectra measured for four different WDM channels selected by the appropriate tuning of the fiber Bragg grating.

spectrum for single mode lasing operation at a wavelength of 1535.656 nm (channel 1) is shown in Fig. 3.19. The side mode suppression ratio (SMSR) is greater than 35 dB. By stretching the grating the single mode lasing action can be discretely tuned to neighboring modes. We have shown the lasing spectrum for four neighboring channels in Fig. 3.19 as well. The spacing between two adjacent channels is determined by the cavity length of the monolithic semiconductor laser. As we have seen before, this spacing can be locked to an external RF reference signal. Locking of the mode-spacing when there is no external feedback has been shown in Fig. 3.18. It is unclear whether this locking is maintained when external feedback by the fiber Bragg grating is applied. Equal lasing power and a SMSR $> 35$ dB is obtained for all channels.

We have next performed a BER measurement for each of the channels. As a first step we have measured the eye-diagram of each of the channels. An eye-diagram is obtained by synchronously writing a sequence of the received random bits to a sampling oscilloscoop. The resulting shape resembles a human eye (see Fig. 3.20) and is widely known as the eye-pattern of the system. Eye-patterns are often used for

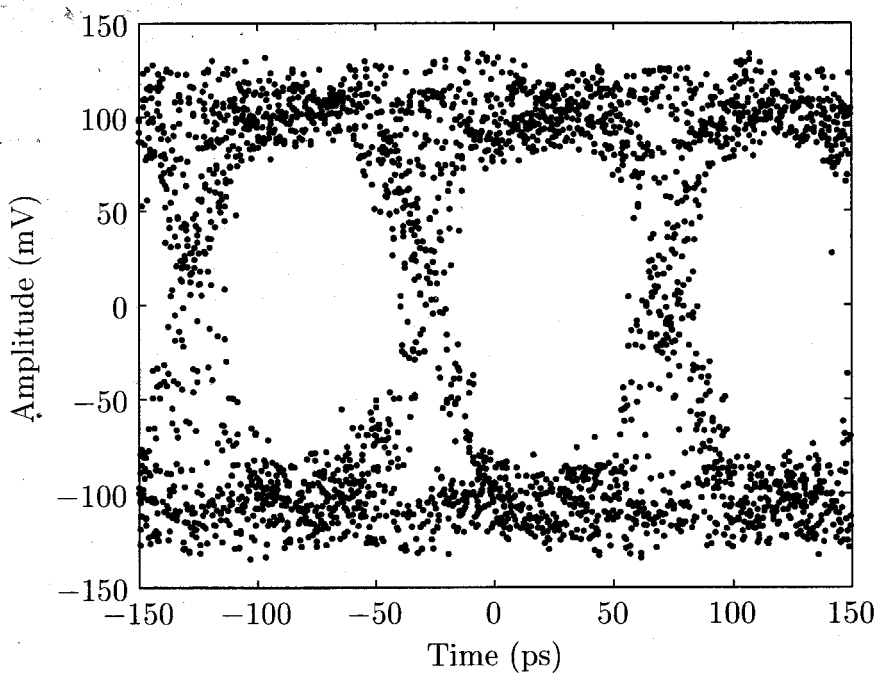


Figure 3.20: Eye-diagram for WDM channel 3 (1536.000 nm). The bit-rate for this measurement is 10 Gbits/s.

monitoring the performance of communication systems. The best time to sample the received waveform at the receiver end occurs when the eye-opening is largest. The larger the eye-opening is the more immune the system is to noise.

For channel 3 we have measured the eye-pattern after transmission over a fiber length of 25 km and its result is shown in Fig. 3.20. From Fig. 3.20 we see that the eye is wide open which means that there is good signal recovery. The exact BER can, however, not be estimated from the eye-diagram. We perform a real BER test for this channel and for the other four channels in order to determine the exact BER. The exact wavelengths of each of the measured channels and the results of the BER measurements are given in Fig. 3.21. For this measurement each channel is modulated with a pseudo-random bit-sequence (PRBS) of $2^{31} - 1$ bits generated by the BER pattern generator. After transmission over 25 km of fiber, the BER is measured as a function of the received power (before amplification) at the receiver end (see Fig. 3.21). "Error free" transmission over the link is achieved for all channels and all channels perform equally well, indicating that our discretely tunable WDM

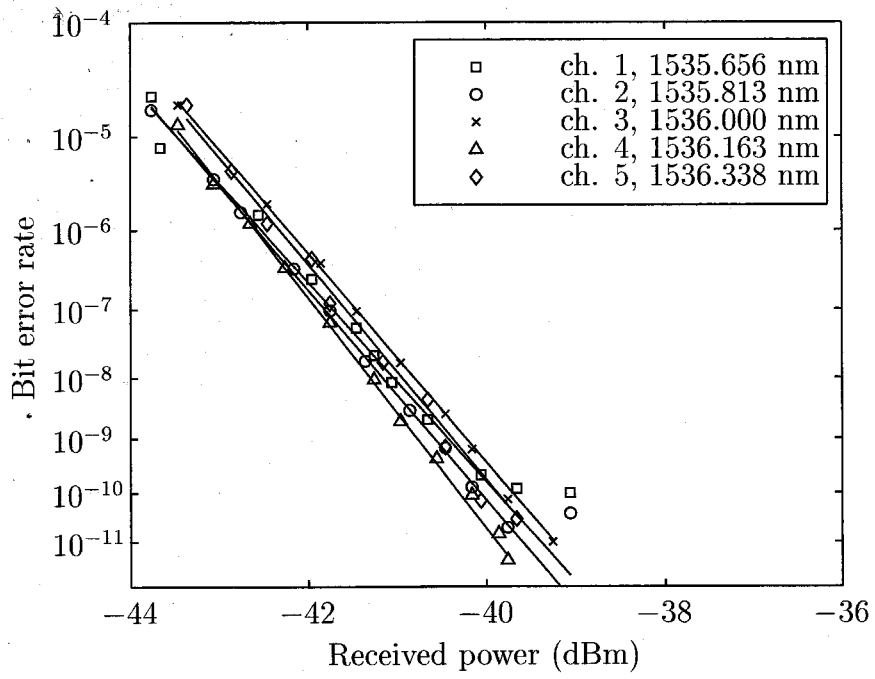


Figure 3.21: BER as a function of the received optical power for channels 1–5.

laser can be used in a WDM system.

## 3.3 A photonic analog/digital (A/D) converter

### 3.3.1 State-of-the-art A/D converter technology

The increasing demand in military systems, and soon civilian, for real-time data over a wide range of signal frequencies has created a need for high speed A/D converters. Current state-of-the art electronic A/D converters operate at a sampling rate of about 10 Giga samples per second (Gsps) with a resolution of about 4-bits per sample. Such a sampling rate, while sufficient for low-end microwave signals, is not sufficient for sampling, for example, high-end microwave signals. To attempt to perform the task of sampling at a rate of, for example, 100 Gsps would require electronic circuitry with uniform frequency responses up to 200-300 GHz. This technology is not available today, and even if selected components can be found to operate at these speeds, the resulting circuit requirements such as parasitic inductances and capacitances and broadband impedance matching are not guaranteed to be solvable in the immediate future, so new approaches need to be considered. Since we are stretching the limits of electronics technology, we need to look to a new direction for solutions. Optics has no problem in handling the bandwidths needed in this application, so it is a reasonable assumption to look in the optics area for solutions. A realizable approach would be one where state-of-the-art electronic components are combined with opto-electronic ones, and this concept is described in the remainder of this chapter.

Recent progress in photonic technology has made high-speed A/D conversion feasible. Under the scheme we are about to introduce [20], analog waveforms are sampled at a rate of up to 100 Gsps, with a minimum resolution of 4-bit per sample. This improvement, over tenfold, in performance is possible because of a number of reasons. First of all, semiconductor mode-locked lasers are capable of generating stable, 10 GHz-range (repetition frequency) pulse trains with relatively little noise. This allows multiple pulse trains with different center wavelengths to be interleaved together to create a multi-wavelength sampling pulse train (MW-SPT) with an even higher repetition frequency (e.g., 100 GHz). Besides that, low-loss fiber add/drop filters are now available for WDM purposes [15]. Thus, multiplexing and demultiplexing of mul-

tiple pulse trains with different center wavelengths can be performed with little loss, resulting in all-fiber systems which is a prerequisite for compact ruggedness. Finally, the photo-detectors operating over 10 GHz are commercially available today. Hence, converting an optical signal to the electric domain does not constitute a bottle-neck in photonic A/D converter designs.

### 3.3.2 *An ultra high speed multi-wavelength sampling pulse train (MW-SPT)*

As in conventional A/D converters, the most crucial part of a photonic A/D converter is the quality of the sampling pulse train. In order to improve on current A/D converter technology, pulse sampling rates have to be in the range of 10–100 Gsps and sampling pulses should have low timing-jitter and amplitude fluctuations. In addition, the optical sampling pulse train has to be generated in such a way that (after the actual sampling of a signal) it can be easily processed (A/D conversion and word encoding) by conventional electronics.

In the next section we introduce a scheme to generate a train of optical sampling pulses that has all of the above properties, by combining ultra short pulse generation in semiconductor lasers with wavelength diversity. The main advantage of this scheme is that it uses wavelength multiplicity to increase the sampling rate of A/D converters. This approach has been made practical by recent developments in WDM filters and semiconductor mode-locked lasers as described in the previous section. The scheme makes use of a multi-wavelength sampling pulse train (MW-SPT). This pulse train consists of ultra short optical pulses with different wavelengths. To be specific, the wavelength of each pulse in the train is different from the wavelength of its neighbors, in a repeating fashion; see Fig. 3.22.

If the goal, for example, is to sample an analog signal at a rate of $f_s = 100$ Gsps, the temporal spacing between two adjacent sampling pulses is $T_s = 1/f_s = 10$ ps. As depicted in Fig. 3.22, neighboring pulses in the pulse train have a different wavelength $\lambda_1 \ldots \lambda_N$, where $N$ is the number of wavelengths used. In our example we use $N = 10$.

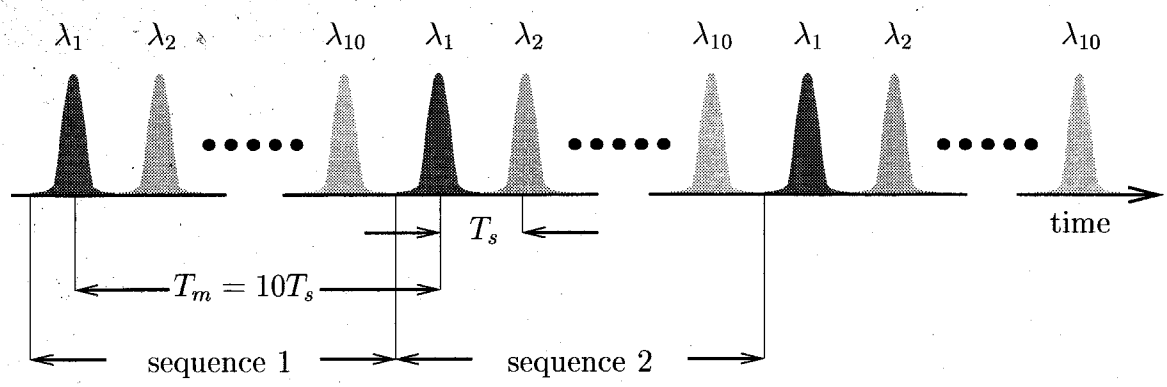


Figure 3.22: A multi-wavelength ultra short pulse train with ten different wavelengths. $T_s$ is the sampling period and $T_m$ is the period for pulses with the same wavelength.

The optical pulse train is thus made up of a repeating sequence of pulses with 10 different wavelengths within each sequence. The temporal spacing between pulses of the same wavelength is $T_m = NT_s = 100$ ps, i.e., the sampling rate for pulses at a particular wavelength is $f_m = f_s/N = 10$ Gsps.

The MW-SPT in our example possesses a pulse repetition rate of 100 Gsps, i.e., $10^{11}$ samples per second. The inter-pulse spacing is thus $10^{-11}$ s. The individual optical pulse widths thus need to be of the order of $\tau_p \lesssim 2 - 3 \cdot 10^{-12}$ s. To generate this pulse width by mode-locking requires lasers with a gain linewidth exceeding $\Delta\nu \sim 1/\tau_p \sim 3 - 5 \cdot 10^{11}$ Hz. The gain linewidth of semiconductor lasers is in excess of $10^{13}$ Hz and thus easily meets our criterion.

Another important consideration is the resolution of the optical filters which are used to assemble the MW-SPT and to demultiplex them following the sampling. This situation is depicted in Fig. 3.23. We are free to choose the set of wavelengths

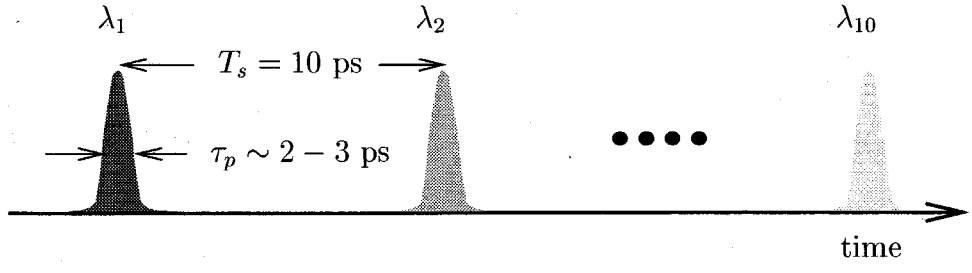


Figure 3.23: Temporal view of the MW-SPT and typical orders of magnitude for pulse duration $\tau_p$ and sampling time $T_s$.

$\lambda_1 \ldots \lambda_{10}$ subject to two requirements:

1. The wavelengths have to be such that mode-locked semiconductor lasers can be made to possess them.
2. The total span $\lambda_1 \ldots \lambda_{10}$ has to fall within the gain bandwidth of erbium doped fiber amplifiers (EDFA) so that the required power levels can be obtained. Using typical EDFA linewidths of 30 nm, we can use an inter-pulse wavelength separation $\Delta\lambda = \lambda_2 - \lambda_1 = \lambda_n - \lambda_{n-1}$ of 30 nm/10 = 3 nm or a corresponding frequency separation of $\Delta\nu = \Delta\lambda c/\lambda^2 \approx 300$ GHz. The linewidth of the optical filters which are used to multiplex and, after sampling the analog signal, to demultiplex the wavelengths $\lambda_1 \ldots \lambda_{10}$ must be smaller than $\Delta\nu$. This is well within the capability of fiber Bragg gratings [21] which in commercial applications are already used to handle (multiplex, demultiplex) optical signals separated by $\Delta\nu < 30$ GHz, i.e., ten times smaller than our system requirements.

The last requirement is that of the optical detectors used to detect, separately, each of the ten parallel optical pulse trains. These detectors are not required to respond to each individual pulse but can be integrated over the whole inter-pulse period which in our example is $10^{-10}$ s. Such detectors are now routinely commercially available.

In order to qualify as a good clock source for A/D conversion, the pulses in the sampling train should exhibit the following properties:

1. Pulse-to-pulse fluctuations should be small, i.e., amplitude fluctuations, pulse width fluctuations and timing-jitter fluctuations should be small. Active (or hybrid) mode-locking of monolithic semiconductor lasers with a high quality radio frequency (RF) source can provide such pulses.
2. The pulse width $\tau_p$ of an individual pulse should be small compared to the sampling time $T_s$, so that an individual pulse behaves essentially as a delta function when sampling the microwave signal. Mode-locking can generate such ultra short pulses [22]. In our design, the sampling time is $T_s = 10$ ps and the pulse width should be on the order of 2-3 ps or less.
3. Pulses of a given width should preferably contain no chirp so that their spectral

width is minimized and the number of usable wavelengths is maximized within the 1530–1560 nm band of optical fibers and erbium doped amplifiers. Note that the minimum spectral width for a Gaussian pulse with a temporal width of 1 ps pulse is about 2.4 nm.

4. Average timing-jitter between any two arbitrary pulses in the sampling train should be bounded in time, so that no so-called "clock wandering" will occur over long periods of time. Clock wandering is inherently avoided in actively mode-locked lasers in contrast to passively mode-locked lasers [23].

### 3.3.3 A photonic A/D converter using a MW-SPT

A schematic view of our photonic A/D converter incorporating this MW-SPT is shown in Fig. 3.24 and Fig. 3.25. The MW-SPT is used to sample the analog signal $V(t)$ by feeding it as the optical input to an electro-optic modulator. The modulator is driven by the microwave signal to be sampled; see Fig. 3.24.

The train of optical pulses at the output of the modulator is thus multiplied by the analog signal $V(t)$. An optical high resolution wavelength demultiplexer ("drop" filters) are then used to separate the ten wavelengths resulting in ten individual parallel optical pulse trains with a relatively low sampling rate $f_m$. Each of these pulse trains can now be detected by a photo-detector and converted into a digital signal by available state-of-the-art A/D converters; see Fig. 3.25.

The net result is thus ten parallel electronic bit-streams that contain the sampled information of the analog signal $V(t)$ in a parallel and interleaved fashion.

The main advantage of this scheme is that it transfers the focus of providing the bandwidth necessary for ultra-high speed sampling (bandwidth $>$ 100 GHz in our example) from electronics, where the limits are about to be reached, to lasers and optics where the bandwidth is available and can be handled without problems. The use of multi-wavelength optical sampling enables us to convert the final high repetition rate data stream to a number of parallel data streams each with a fraction of the sampling rate. This final data rate is chosen to be low enough so that it can

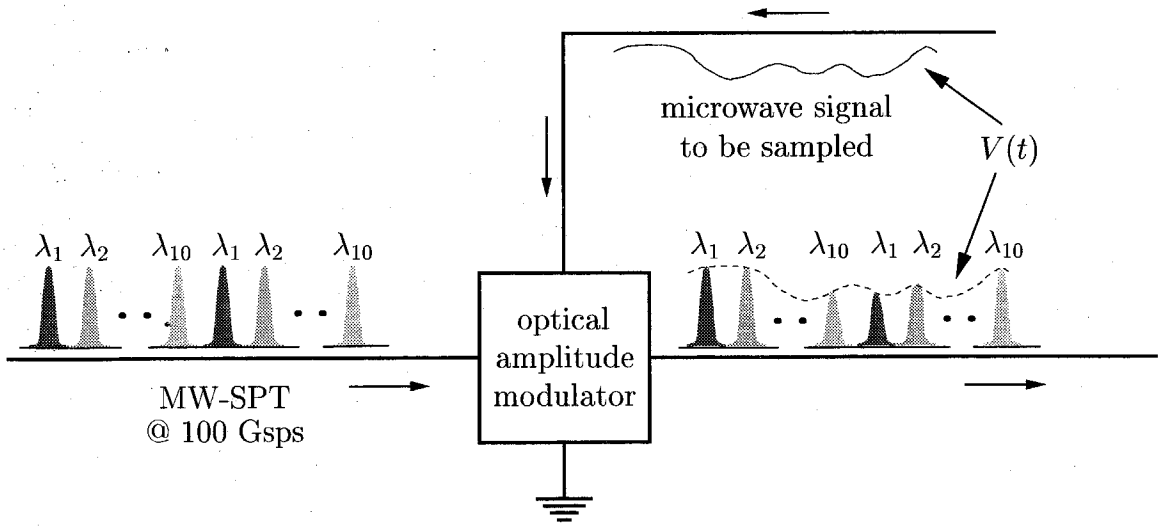


Figure 3.24: A MW-SPT samples a microwave signal at 100 Gsps.

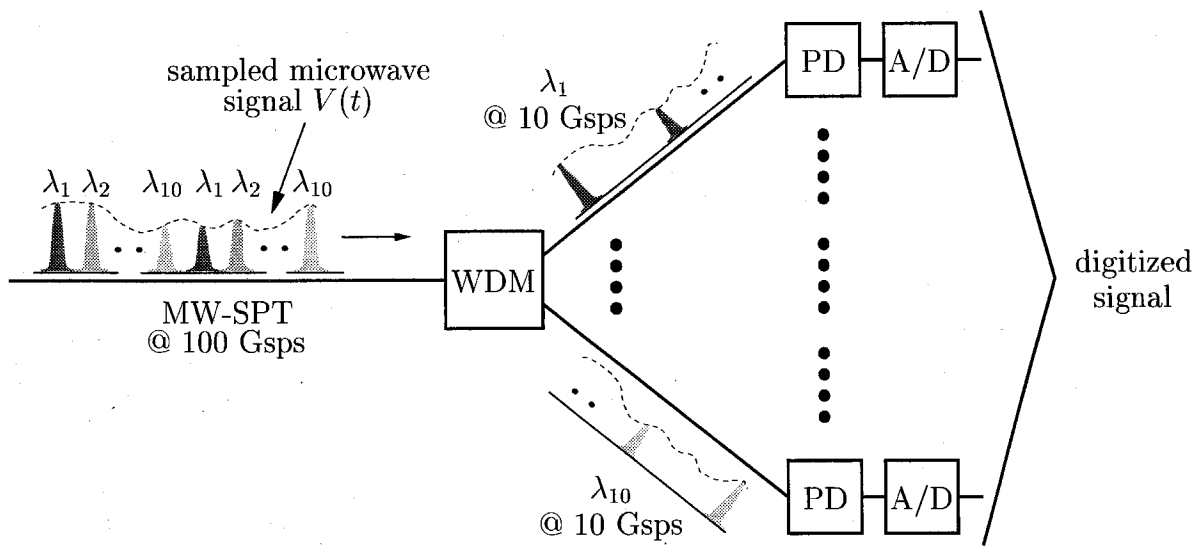


Figure 3.25: The stream of samples at 100 Gsps is wavelength demultiplexed (WDM) into ten parallel 10 Gsps streams which are detected by photo-detectors (PD) and processed by electronic A/D converters.

be handled by state-of-the-art conventional electronic A/D conversion.

### 3.3.4 A scheme for the generation of the MW-SPT

The most crucial part in the photonic A/D converter is the MW-SPT. Pulse to pulse fluctuations, i.e., amplitude-, pulse width and timing-jitter, should be small in order to avoid distortion. Hybridly mode-locked semiconductor lasers are capable of generating stable high repetition rate ultra short pulse trains with relatively little amplitude and timing jitter [24]. Recently low-loss add/drop filters have become available for WDM [15], so that multiple pulse trains from lasers mode-locked at different center wavelengths can be multiplexed with low loss into a higher repetition rate MW-SPT suitable for A/D conversion. Our scheme to generate the MW-SPT is depicted in Fig. 3.26.

We use ten monolithically mode-locked semiconductor lasers to generate ten pulse streams with different wavelengths $\lambda_1 \ldots \lambda_{10}$. The wavelength of each laser can be controlled by changing its temperature. A more elegant way of wavelength control could be obtained by incorporating Bragg reflectors inside the laser cavity. This would lead to an increase of pulse power by confining the gain to a specific wavelength region [10] as well as improve the locking bandwidth of the device for hybrid mode-locking [11].

All lasers are hybridly mode-locked by the same high quality, low timing-jitter electronic RF oscillator at a modulation frequency of $f_m = 10$ GHz. Another important issue is the fine tuning of the position of the optical pulses in the multiplexed MW-SPT (see Fig. 3.22). The delay between pulse streams is controlled electronically by variable phase delays to the RF driving signal. This is achieved by simple insertion of microwave variable phase delay units in-between the mode-locked lasers and the RF driving source. A variation of $\Delta\phi = 360°$ of the RF driving signal to a given laser shifts the pulse at the corresponding wavelength by the inter-pulse separation $T_m$ ($10^{-11}$ for our example). Simple sub-picosecond pulse position control is thus feasible without the need for any variable optical delay lines.

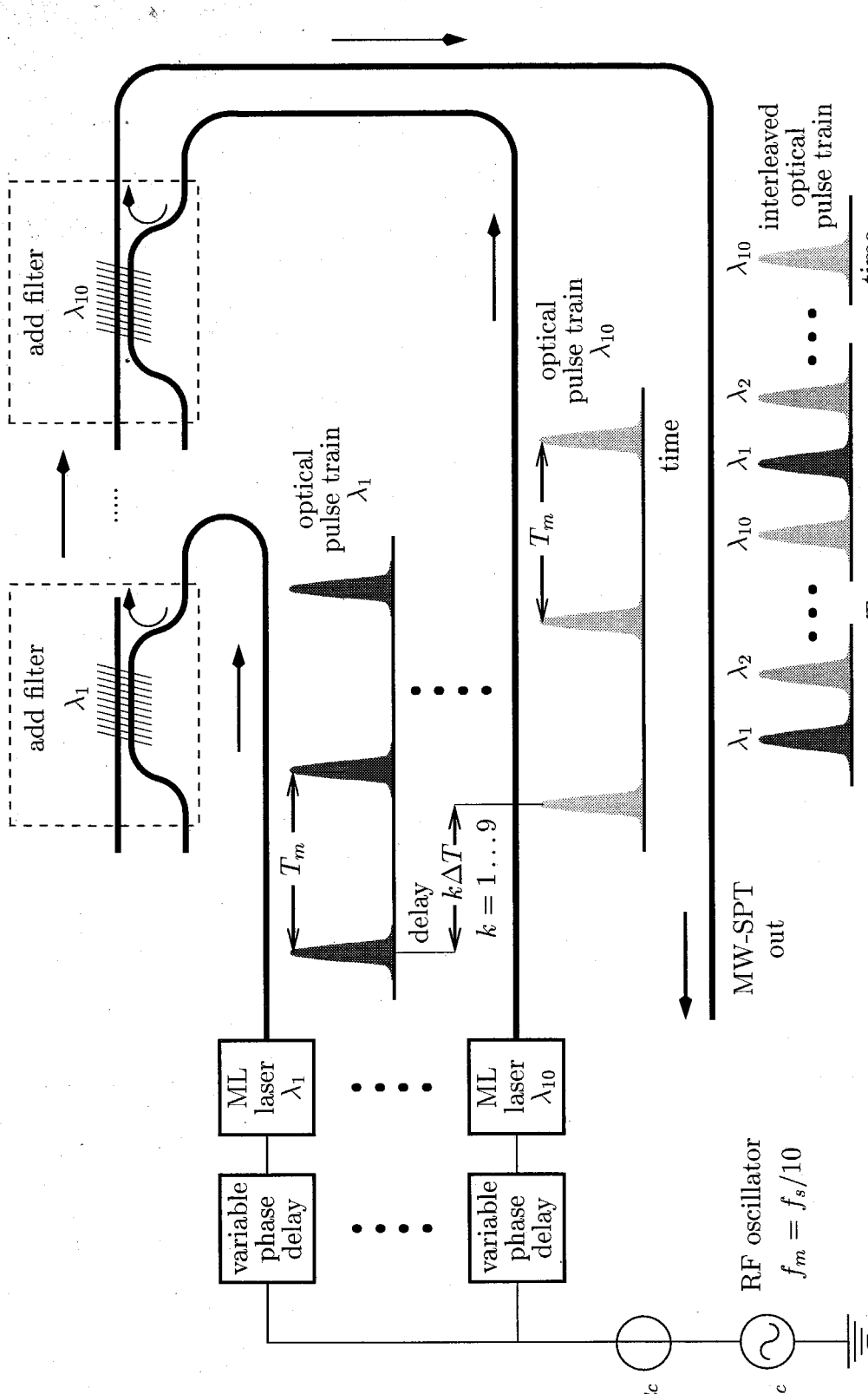


Figure 3.26: Generation of a MW-SPT using hybridly mode-locked lasers, electronic phase delays and low-loss add filters.

Low-loss add filters are next used to interleave all ten pulse trains into the MW-SPT of Fig. 3.22. For our example of $T_s = 100$ Gsps, pulse widths would be of the order of a few picoseconds while wavelength spacing would be around $\Delta\lambda = \lambda_n - \lambda_{n-1} \approx 3$ nm. These values can be easily achieved with present mode-locked semiconductor lasers [25].

### 3.3.5 *Advantages of the proposed scheme*

In this section we describe a number of advantages that are inherent to our proposed scheme for the generation of the MW-SPT. First of all our scheme provides for compactness and eased assembly. A monolithic semiconductor laser has the important advantage that it is a very compact device. No external bulk optical parts (lenses, gratings, polarizers, etc.) are needed in order to mode-lock the laser. The mode-locking process takes place in a cavity of only a few millimeters. This in contrast to externally mode-locked lasers and mode-locked fiber lasers which take a much larger amount of space and also use a fair number of bulk optical parts. Also, long term cavity stability problems, alignment difficulties, and scaling problems associated with multiple lasers are avoided in our approach. Monolithic cavity mode-locked lasers can be as easily packaged and fiber-coupled as any other DFB laser. Therefore, they are very robust and can be easily incorporated with other all-fiber components.

Another important advantage is that the use of multiple lasers provides wavelength dependent power control which facilitates pulse amplitude equalization. It also provides the ability of an easy temporal delay of each pulse train of a particular wavelength. As known from various papers in literature [6, 7, 26], pulses with different wavelengths can also be generated from a single laser using spectral slicing or the super-continuum in optical fibers. In our approach, we have explicitly chosen to create our MW-SPT from separate lasers. The most important advantage is that wavelength dependent losses in the rest of the system can be compensated by changing the gain of the laser that provides that particular wavelength. When using a single laser, this is impossible because changing the gain will change the gain for all

wavelengths at the same time. A major system advantage of using multiple lasers is that the delay between pulse trains of different wavelengths can be easily controlled electronically by phase delays of the RF drives to the individual lasers. A single laser would require very accurate picosecond optical delay units which are difficult to engineer.

By using mode-locked lasers the pulse repetition rate can be easily adjusted to the region of interest. The repetition rate of pulses for each of the mode-locked lasers will need to be adjusted to the highest sampling rate that can still be processed by conventional state-of-the-art electronics (around 10 Gsps). In mode-locked lasers, this repetition rate is determined by the cavity length and a pulse repetition rate of around 10 GHz means a cavity length of a few millimeters. When using monolithic semiconductor lasers such a cavity can be easily obtained by cleaving the semiconductor wafer to this desired length. Externally mode-locked semiconductor and fiber lasers usually have cavity lengths up to a couple of meters, meaning that the pulse repetition rate will be extremely low (in the order of a few hundred MHz). This means that additional temporal multiplexing and/or other tricks will have to be applied in order to get the pulse repetition rate up into the GHz range. One way to do this is by harmonically mode-locking a laser. This has been demonstrated in fiber lasers up to 1 GHz [27], but it requires a significant number of additional optical and RF components in the setup.

## References

[1] M. Sharma, H. Ibe, and T. Ozeki, "WDM ring network using a centralized multiwavelength light source and add-drop multiplexing filters," *J. Lightwave Technol.*, vol. 15, no. 6, pp. 917–929, 1997.

[2] H. Toba, K. Oda, K. Nakanishi, N. Shibata, K. Nosu, N. Takato, and K. Sato, "100-channel optical FDM transmission distribution at 622 Mbit/s over 50km utilizing a wave-guide frequency selection switch," *Electron. Lett.*, vol. 26, no. 6, pp. 376–377, 1990.

[3] R. Monnard, C. Doerr, C. Joyner, M. Zirngibl, and L. Stulz, "Direct modulation of a multifrequency laser up to 16x622 Mb/s," *IEEE Photon. Technol. Lett.*, vol. 9, no. 6, pp. 815–817, 1997.

[4] K. Liou, J. Stark, U. Koren, E. Burrows, J. Zyskind, and K. Dreyer, "System performance of an eight-channel WDM local access network employing a spectrum-sliced and delay-line-multiplexed LED source," *IEEE Photon. Technol. Lett.*, vol. 9, no. 5, pp. 696–698, 1997.

[5] D. Sampson and W. Holloway, "100-mW spectrally-uniform broad-band ASE source for spectrum-sliced WDM systems," *Electron. Lett.*, vol. 30, no. 19, pp. 1611–1612, 1994.

[6] W. Holloway, A. Keating, and D. Sampson, "Multiwavelength source for spectrum-sliced WDM access networks and LAN's," *IEEE Photon. Technol. Lett.*, vol. 9, no. 7, pp. 1014–1016, 1997.

[7] T. Morioka, K. Mori, S. Kawanishi, and M. Saruwatari, "Multi-WDM-channel, Gbit/s pulse generation from a single laser source utilizing LD-pumped supercontinuum in optical fibers," *IEEE Photon. Technol. Lett.*, vol. 6, no. 3, pp. 365–368, 1994.

[8] D. Eliyahu, A. Yariv, and R. Salvatore, "Broader, flatter optical spectra of passively mode- locked semiconductor lasers for a wavelength- division multiplexing source," *Appl. Opt.*, vol. 36, no. 15, pp. 3430–3434, 1997.

[9] H. Sanjoh, H. Yasaka, Y. Sakai, K. Sato, H. Ishii, and Y. Yoshikuni, "Multiwavelength light source with precise frequency spacing using a mode-locked semiconductor laser and an arrayed waveguide grating filter," *IEEE Photon. Technol. Lett.*, vol. 9, no. 6, pp. 818–820, 1997.

[10] A. S., Y. Matsui, T. Kunii, S. Oshiba, and Y. Ogawa, "Transform-limited optical short-pulse generation at high-repetition-rate over 40 GHZ from a monolithic passive mode-locked DBR laser-diode," *IEEE Photon. Technol. Lett.*, vol. 5, no. 12, pp. 1362–1365, 1993.

[11] L. Zhai, A. Lowery, and Z. Ahmed, "Locking bandwidth of actively mode-locked semiconductor-lasers using fiber-grating external cavities," *IEEE J. Quantum Electron.*, vol. 31, no. 11, pp. 1998–2005, 1995.

[12] R. Tucker, U. Koren, G. Raybon, C. Burrus, B. Miller, T. Koch, and G. Eisenstein, "40-GHZ active mode-locking in a 1.5-$\mu$m monolithic extended-cavity laser," *Electron. Lett.*, vol. 25, no. 10, pp. 621–622, 1989.

[13] R. Huang, D. Wolf, W. Cheng, C. Jiang, R. Agarwal, D. Renner, A. Mar, and J. Bowers, "High-speed, low-threshold InGaAsP semiinsulating buried crescent lasers with 22 GHZ bandwidth," *IEEE Photon. Technol. Lett.*, vol. 4, no. 4, pp. 293–295, 1992.

[14] T. Chen, P. Chen, C. Gee, and N. Barchaim, "A high-speed InGaAsP/InP DFB laser with an air bridge contact configuration," *IEEE Photon. Technol. Lett.*, vol. 5, no. 1, pp. 1–3, 1993.

[15] A. Kewitsch, G. Rakuljic, P. Willems, and A. Yariv, "All-fiber zero-insertion-loss add-drop filter for wavelength-division multiplexing," *Opt. Lett.*, vol. 23, no. 2, pp. 106–108, 1998.

[16] D. Von der Linde, "Characterization of the noise in continuously operating mode-locked lasers," *Appl. Phys. B*, vol. 39, no. 4, pp. 201–217, 1986.

[17] S. Sanders, *Passive mode-locking and millimiter-wave modulation of quantum well lasers.* PhD thesis, California Institute of Technology, 1992.

[18] E. Yoshida and M. Nakazawa, "Measurement of the timing jitter and pulse energy fluctuation of a PLL regeneratively mode-locked fiber laser," *IEEE Photon. Technol. Lett.*, vol. 11, no. 5, pp. 548–550, 1999.

[19] S. Lathi and Y. Yamamoto, "Influence of nonlinear gain and loss on the intensity noise of a multimode semiconductor laser," *Phys. Rev. A.*, vol. 59, no. 1, pp. 819–825, 1999.

[20] A. Yariv and R. Koumans, "Time interleaved optical sampling for ultrahigh speed A/D conversion," *Electron. Lett.*, vol. 34, no. 21, pp. 2012–2013, 1998.

[21] C. Giles, "Lightwave applications of fiber Bragg gratings," *J. Lightwave Technol.*, vol. 15, no. 8, pp. 1391–1404, 1997.

[22] T. Schrans, R. Salvatore, S. Sanders, and A. Yariv, "Subpicosecond (320 fs) pulses from CW passively mode-locked external cavity 2-section multiquantum well lasers," *Electron. Lett.*, vol. 28, no. 16, pp. 1480–1482, 1992.

[23] D. Eliyahu, R. Salvatore, and A. Yariv, "Effect of noise on the power spectrum of passively mode-locked lasers," *J. Opt. Soc. Amer. B*, vol. 14, no. 1, pp. 167–174, 1997.

[24] S. Sanders, T. Schrans, A. Yariv, J. Paslaski, J. Ungar, and H. Zarem, "Timing jitter and pulse energy fluctuations in a passively mode-locked 2-section quantum-well laser coupled to an external cavity," *Appl. Phys. Lett.*, vol. 59, no. 11, pp. 1275–1277, 1991.

[25] R. Salvatore, T. Schrans, and A. Yariv, "Wavelength tunable source of subpicosecond pulses from CW passively mode-locked 2-section multiple- quantum-well laser," *IEEE Photon. Technol. Lett.*, vol. 5, no. 7, pp. 756–758, 1993.

[26] M. Nuss, W. Knox, and U. Koren, "Scalable 32 channel chirped-pulse WDM source," *Electron. Lett.*, vol. 32, no. 14, pp. 1311–1312, 1996.

[27] M. Margalit, C. Yu, S. Namiki, E. Ippen, and H. Haus, "Harmonic mode-locking using regenerative phase modulation," *IEEE Photon. Technol. Lett.*, vol. 10, no. 3, pp. 337–339, 1998.

# CHAPTER 4

# *Review of methods to characterize optical pulses*

## 4.1 Introduction

The number of methods to characterize optical pulses has increased extensively over the last decade. There are various ways to characterize an optical pulse. In this chapter we review a number of important pulse characterization methods and discuss their practical value. In order to maintain a uniform mathematical description for all methods that are described, we start with a section on the notational conventions that will be used throughout the rest of this thesis. Most characterization methods use the measurement of some kind of correlation function as their basis and we therefore describe the most commonly used correlation techniques first. Although there are both interferometric and non-interferometric characterization methods, we focus our attention on the non-interferometric methods as these have usually less stringent experimental requirements. One recent and very powerfull method to fully characterize an optical pulse is frequency-resolved optical gating (FROG). The basics of this method are discussed in detail as this method is the inspiration for the development in this work of its time-domain variant time-resolved optical gating (TROG). This last new method is the topic of discussion in the next chapter. Another important characterization method which is strongly connected to both FROG and TROG is frequency-domain phase measurement (FDPM) and the basics of this method are discussed as well.

## 4.2 Notational conventions

In this section we introduce the mathematical description which will be used throughout the rest of this thesis for notational consistency. Note that this notation can be different from the symbols introduced in the previous chapters.

The electric field representing an ultra-short optical pulse can be described in the time-domain as

$$E(t) = A(t)\exp(+j2\pi f_0 t) \tag{4.1}$$

where $f_0$ is the optical carrier frequency and $A(t)$ is the "slowly" varying complex envelope of the field representing the amplitude and phase of the pulse. $A(t)$ is normalized in such a way that $|A(t)|^2$ represents the intensity of the pulse. One can also represent the electric field in the frequency-domain by Fourier transforming it

$$\widetilde{E}(f) = \widetilde{A}(f - f_0) \tag{4.2}$$

where $\widetilde{E}(f)$ and $\widetilde{A}(f)$ represent the Fourier transform of $E(t)$ and $A(t)$ respectively. Throughout the remaining chapters the following Fourier transform pairs are used:

$$\widetilde{X}(f) = \int X(t)\exp(-j2\pi ft)\,\mathrm{d}t \tag{4.3a}$$

$$X(t) = \int \widetilde{X}(f)\exp(+j2\pi ft)\,\mathrm{d}f \tag{4.3b}$$

and all integrals are assumed to be from $-\infty$ to $+\infty$ unless otherwise noted. Frequency-domain variables are indicated by a tilde.

To demonstrate the features of certain characterization methods in the following sections and chapters, we introduce a pulse shape in this section which is used in examples and simulations later on. The pulse is a non-linearly chirped double pulse which can be mathematically represented by

$$A(t) = |A(t)|\exp\{j\varphi(t)\} \tag{4.4}$$

where the amplitude of the pulse is

$$|A(t)| = \exp\left\{-a\left(\frac{t-d}{t_0}\right)^2\right\} + b\exp\left\{-c\left(\frac{t-e}{t_0}\right)^2\right\} \tag{4.5a}$$

and the phase of the pulse is

$$\varphi(t) = \alpha\left(\frac{t}{t_0}\right) + \beta\left(\frac{t}{t_0}\right)^2 + \gamma\left(\frac{t}{t_0}\right)^3 + \delta\left(\frac{t}{t_0}\right)^4 + \varepsilon\left(\frac{t}{t_0}\right)^5 \tag{4.5b}$$

The pulse parameters are chosen to be

$$\begin{array}{lll} & & \alpha = -0.058 \\ a = 0.75 & t_0 = 1 \text{ ps} & \beta = -0.41 \\ b = 0.50 & d = -1.0\, t_0 & \gamma = -0.00044 \\ c = 2.00 & e = 2.0\, t_0 & \delta = -0.0007 \\ & & \varepsilon = -0.00003 \end{array} \tag{4.6}$$

The amplitude parameters have been chosen to obtain a double pulse in the time-domain and the chirp parameters are taken from [1], except for the fact that $\beta$ has been adapted to obtain a double peaked intensity spectrum. The amplitude (solid lines) and phase (dashed lines) of the pulse in the time and frequency-domain are shown in Fig. 4.1 and Fig. 4.2 respectively. The pulse contains a non-linear down-chirp, i.e., the blue components are present in the leading edge of the pulse and the red components in the trailing edge. This particular pulse description has been chosen in order to demonstrate that the methods we are about to describe work not only on simple pulse shapes but also on complex pulses with non-linear phase variations like this one.

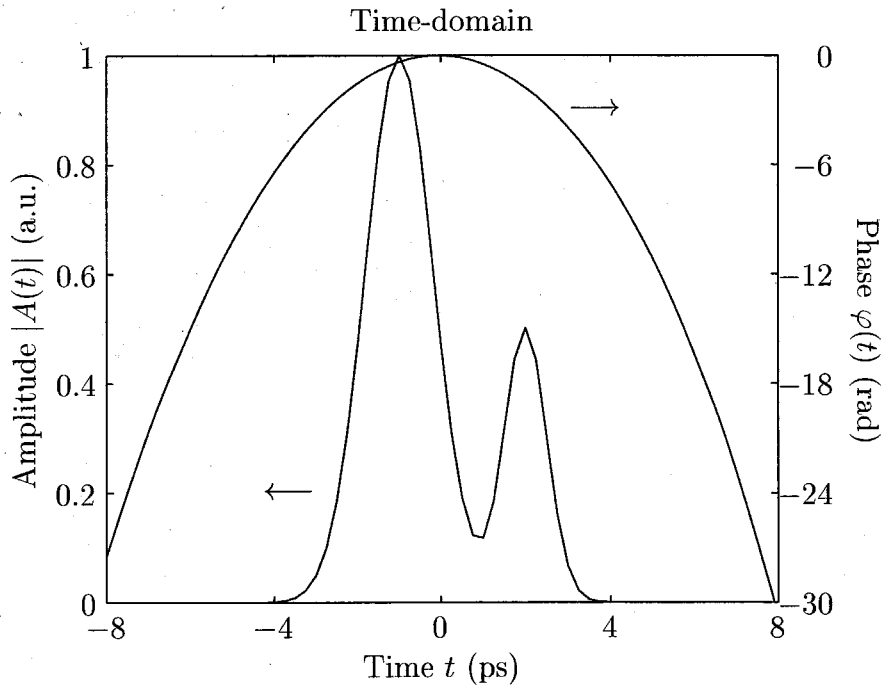


Figure 4.1: Amplitude and phase of the non-linearly chirped double pulse represented in the time-domain.

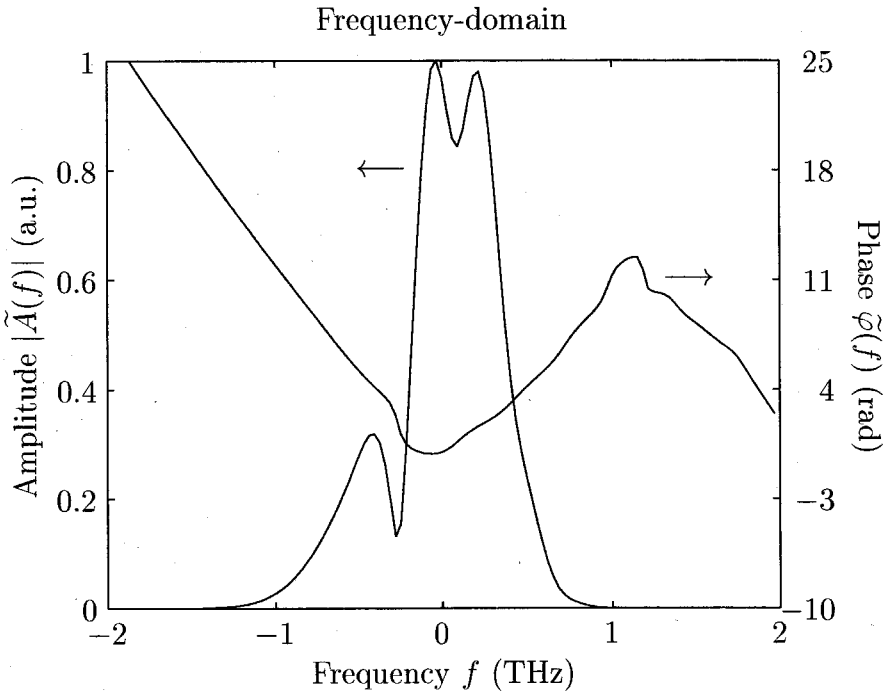


Figure 4.2: Amplitude and phase of the non-linearly chirped double pulse represented in the frequency-domain.

## 4.3 Autocorrelation traces

We will start with the description of two often used correlation methods. Although correlation measurements by themselves often can not fully characterize an optical pulse, they are useful to obtain certain estimates about pulse quantities like the pulse duration for example. They also form an important part in the measurement setup of most methods that are able to fully characterize an optical pulse. We will therefore shortly discuss these methods and their limitations in this section.

### 4.3.1 Background free autocorrelator

One of the most popular ways of getting information about an optical pulse is to measure its intensity (or background-free) autocorrelation trace by mixing the pulse with a delayed version of itself in a second harmonic generating (SHG) crystal [2, 3]. The experimental setup for the measurement of a background free autocorrelation trace is shown in Fig. 4.3. The input pulse $A(t)$ is split up into two replicas by a

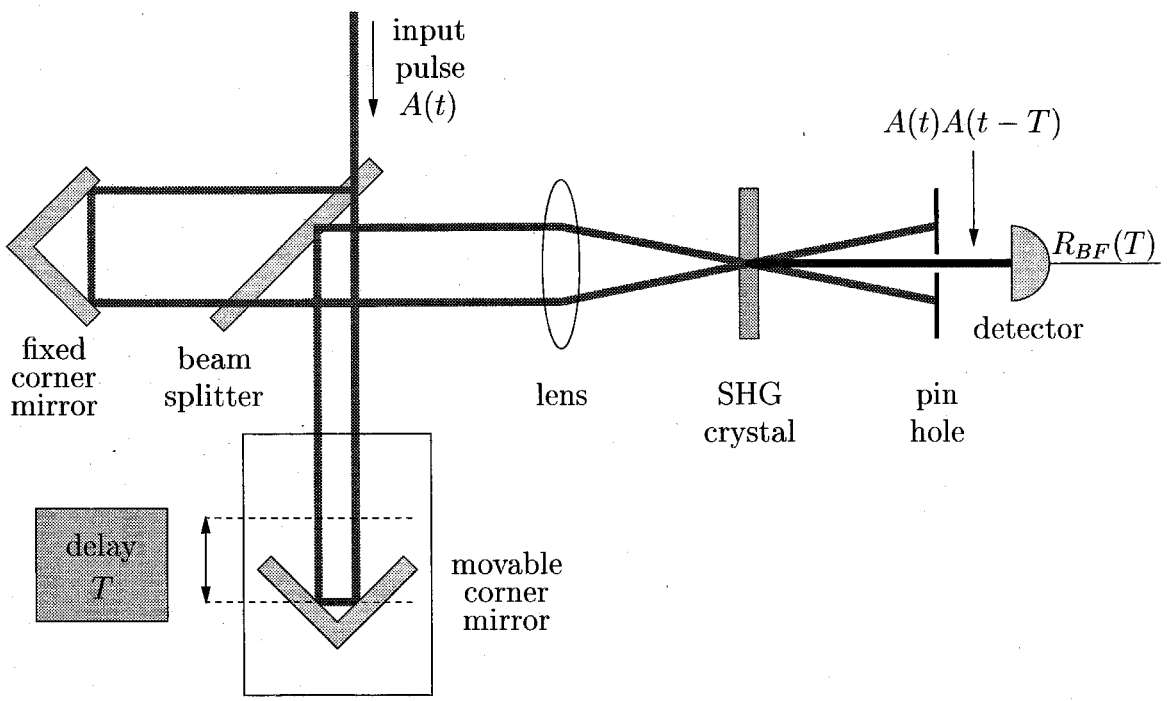


Figure 4.3: Experimental setup for the measurement of a background free autocorrelation trace.

beamsplitter. The two replicas are spatially separated by corner mirrors and one replica is delayed by a time $T$. The two beams that contain the orignal pulse and its delayed version are then focused onto a SHG crystal. Only in the case where the pulses in both beams are overlapping in time, the resulting SHG signal can pass through the pinhole and reach the detector. If the pulses are non-overlapping, their corresponding SHG signal is blocked by either side of the pinhole. This kind of autocorrelation measurement is therefore called a "background free" measurement. The SHG signal that passes through the pinhole is measured with an integrating photodetector. The detected background free autocorrelation signal $R_{BF}(T)$ is given by

$$R_{BF}(T) = \int |A(t)|^2 |A(t-T)|^2 \, \mathrm{d}t \tag{4.7}$$

Due to the nature of the measurement all phase information is lost during the measurement and complete characterization of the pulse in amplitude and phase is impossible. One can get an estimate of the pulse duration by assuming a certain pulse shape and fitting its autocorrelation trace to the measured one. Although temporal decorrelation of the autocorrelation trace of a laser pulse has recently been demonstrated theoretically [4], the method does not always reconstruct the intensity of the pulse correctly as the problem does not have a unique solution. Besides— the method does not work well for experimentally measured autocorrelation traces due to additive noise.

### 4.3.2 *Interferometric autocorrelator*

An often used variant to the measurement of the background-free autocorrelation trace is a measurement of the interferometric (or fringe-resolved) autocorrelation trace [5]. The experimental setup for the measurement of an interferometric autocorrelation trace is shown in Fig. 4.4. The input pulse $A(t)$ is split up into two replicas by a beamsplitter. The two replicas are in this case not spatially separated. One replica is delayed by a time $T$ and both replicas are next colinearly focused onto a SHG crystal. After filtering out the fundamental frequency, the SHG signal is measured with an in-

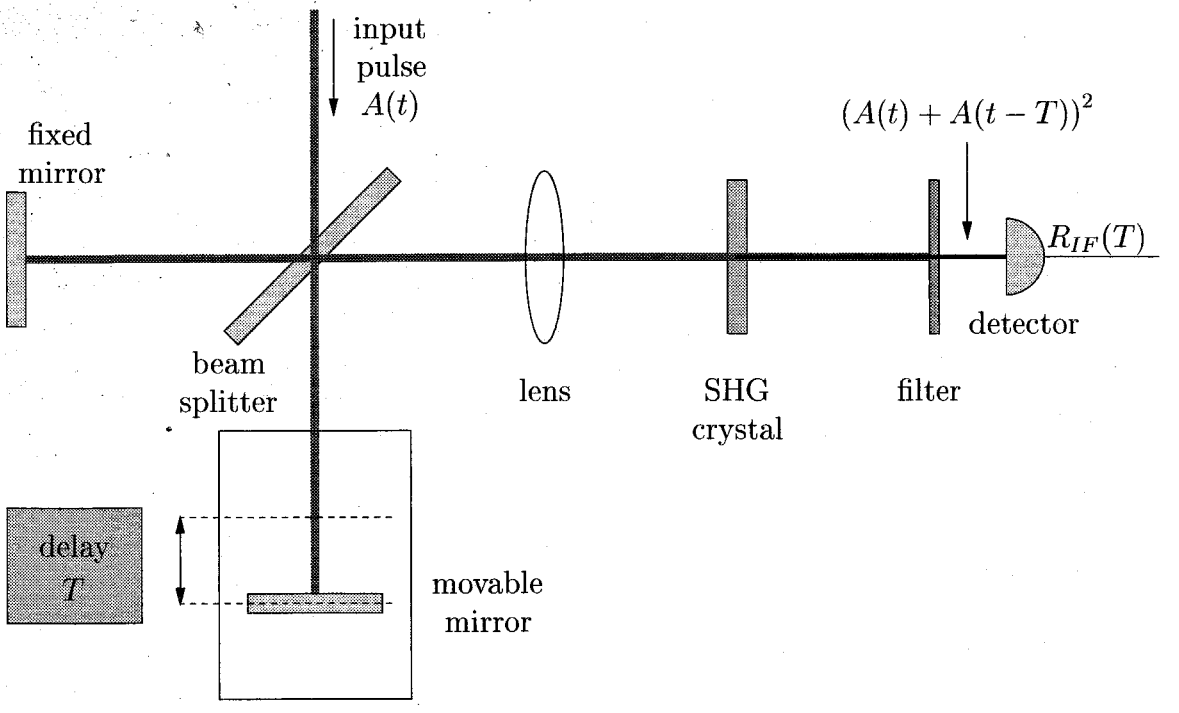


Figure 4.4: Experimental setup for the measurement of an interferometric autocorrelation trace.

tegrating photodetector. The detected interferometric autocorrelation signal $R_{IF}(T)$ is given by

$$R_{IF}(T) = \int \left| A(t) + A(t-T)\, \mathrm{e}^{-j2\pi f_0 T} \right|^2 \mathrm{d}t \tag{4.8}$$

Although the interferometric trace gives some information regarding the chirp imposed on the pulse, complete reconstruction of the phase and amplitude as a function of time or frequency is very complicated. An accurate measurement of the fringes is needed and this is not always possible especially for pulses in the picosecond range. In addition a careful deconvolution method has to be used [6, 7]. Also, the direction of time for the pulse can not be directly inferred from the measurement as all autocorrelation traces are symmetric in the time-axis. Another disadvantage is that the deconvolution method is very sensitive to measurement noise introduced, for example, by mechanical fluctuations of the autocorrelator.

## 4.4 Frequency-resolved optical gating (FROG)

There are a number of non-interferometric methods which can fully characterize a pulse. A very powerful method — frequency-resolved optical gating (FROG) — has recently been introduced by Kane and Trebino [1, 8–12]. In this method, the pulse to be characterized is cross-correlated with a delayed gating pulse in a non-linear crystal to generate a higher harmonic light output. The spectrum of this higher harmonic is measured as a function of the delay of the gating pulse. The gating pulse can take on many shapes depending on the measurement setup (also called geometry) that is used [13] and a few examples will be given later on. The measured spectra make up a two-dimensional FROG trace also called spectogram of the pulse. The amplitude and phase of the pulse can be reconstructed from this measured FROG trace by an iterative algorithm based on generalized projections (GP) [14–17].

### 4.4.1 Basics of FROG

A schematic diagram for the measurement of a FROG trace is given in Fig. 4.5. The pulse $A(t)$ is filtered in the time-domain by a gating function $G_{\mathrm{FROG}}(t,T)$, where $T$ is a variable time-delay. The signal field at the output of the time-gate is given by

$$S_{\mathrm{FROG}}(t,T) = A(t)G_{\mathrm{FROG}}(t,T) \tag{4.9}$$

The signal field is subsequently spectrally filtered and detected by a square-law and integrating detector. The signal at the output of the detector can be found by applying

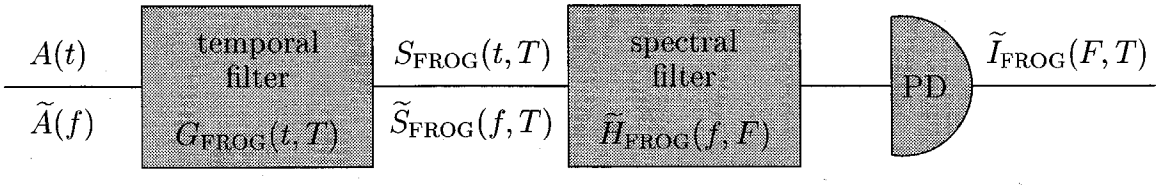


Figure 4.5: Schematic diagram for the FROG measurement setup consisting of a temporal filter followed by a spectral filter and an integrating photo-detector (PD).

straightforward linear system analysis and is given by

$$\widetilde{I}_{\mathrm{FROG}}(F,T) = \int \left|\widetilde{H}_{\mathrm{FROG}}(f,F)\right|^2 \left|\int A(t) G_{\mathrm{FROG}}(t,T)\exp(-j2\pi f t)\,\mathrm{d}t\right|^2 \mathrm{d}f \quad (4.10)$$

As the measured signal is a frequency-resolved quantity, we have indicated it with a tilde.

In most of the experimental setups (also called geometries) that are available for FROG, a spectrometer is used to perform the task of spectral filtering and detection. If the resolution of the spectrometer is much smaller than the spectrum of the pulse, the spectral transfer function behaves as a delta-function

$$|\widetilde{H}_{\mathrm{FROG}}(f,F)|^2 \rightarrow \delta(f-F) \quad (4.11)$$

and the detected signal is given by

$$\widetilde{I}_{\mathrm{FROG}}(F,T) = \left|\int A(t) G_{\mathrm{FROG}}(t,T)\exp(-j2\pi F t)\,\mathrm{d}t\right|^2 \quad (4.12)$$

This quantity is called the FROG trace or spectrogram of the input pulse; it is the set of spectra of different temporal components of the pulse.

As we have mentioned in the introduction, different measurement geometries are available for FROG and each of them has its own characteristic gating function. To date six FROG geometries have been proposed: second harmonic generation (SHG-FROG) [16, 18, 19], third harmonic generation (THG-FROG) [20], polarization gate (PG-FROG) [8, 10, 15, 21], self diffraction (SD-FROG) [1, 22], cross-phase modulation (XPM-FROG) [23, 24] and self-phase modulation (SPM-FROG) [25] with the

following gating functions respectively

$$G_{\mathrm{SHG}}(t,T) = A(t-T) \tag{4.13a}$$

$$G_{\mathrm{THG}}(t,T) = A(t)A(t-T) \tag{4.13b}$$

$$G_{\mathrm{PG}}(t,T) = |A(t-T)|^2 \tag{4.13c}$$

$$G_{\mathrm{SD}}(t,T) = A(t)A^*(t-T) \tag{4.13d}$$

$$G_{\mathrm{XPM}}(t,T) = \exp\left\{ j2\pi f_0 \left(2|A_p(t-T)|^2\right) \frac{n_2 L}{c} \right\} \tag{4.13e}$$

$$G_{\mathrm{SPM}}(t,T) = \exp\left\{ j2\pi f_0 \left(\frac{2}{3}\eta|A(t)|^2 + \frac{4}{3}(1-\eta)|A(t-T)|^2\right) \frac{n_2 L}{c} \right\} \tag{4.13f}$$

where $|A_p(t)|^2$ is the pump intensity causing the XPM, $n_2$ is the non-linear refractive index, $L$ is the interaction length over which the phase modulation takes place, $c$ is the speed of light and $\eta$ is a small proportionality constant. All geometries have been demonstrated experimentally.

It is noted that Franco and Lange [23, 24] do not recognize XPM as a FROG geometry and use a different phase retrieval algorithm for pulse reconstruction. Pulse reconstruction is however possible with the FROG algorithm, which is discussed in the next section. The pulse reconstruction procedure has been shown theoretically for the SPM geometry in [25]. A note with respect to the SPM geometry is in place here. For this geometry, the pulse is phase modulated by a delayed version of itself while propagating in an optical fiber. It is noted that a long length of fiber and high pulse intensity are needed to obtain a useful amount of SPM for the reconstruction algorithm to work. Fiber dispersion is usually not negligible for these lengths of fiber. It will change the shape and phase of the pulse while propagating and this is not taken into account in the SPM gating function. This method only works experimentally if a non-linear medium is available with a small enough dispersion. The technique has been recently demonstrated experimentally [26] and is also referred to as Fiber-FROG. More guidelines regarding what non-linear fiber should be used are given in [26].

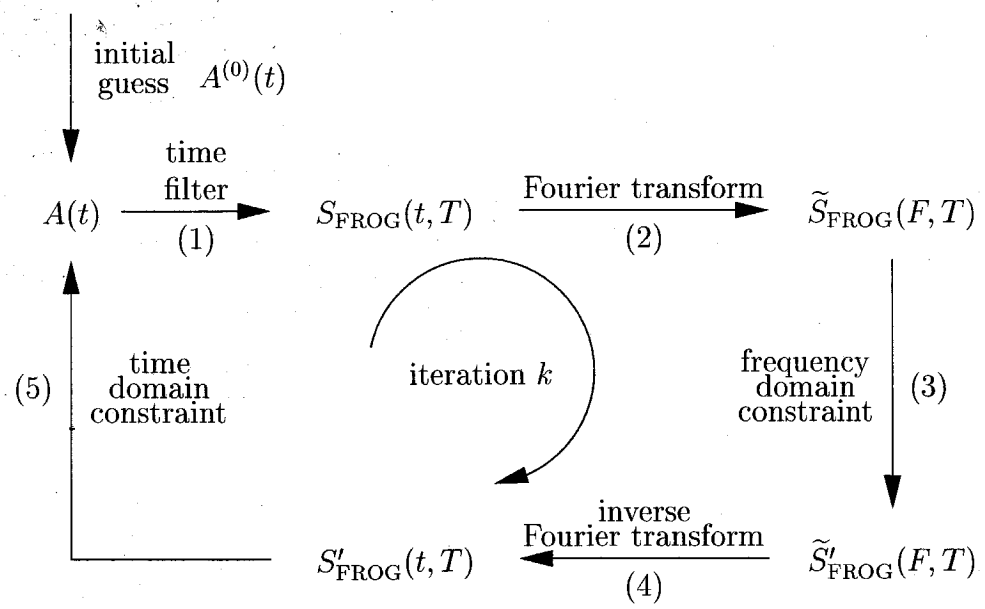


Figure 4.6: Diagram of the pulse reconstruction algorithm for FROG.

### 4.4.2 *Pulse reconstruction algorithm for FROG*

The FROG trace or spectogram of a pulse as given by (4.12) contains enough information to reconstruct its pulse shape and amplitude. This reconstruction is however not straightforward; an iterative reconstruction method needs to be applied with additional constraints. The diagram of the pulse reconstruction algorithm for FROG is shown in Fig. 4.6. The algorithm is started from an initial arbitrary guess for the complex pulse envelope $A^{(0)}(t)$. On the $k^{\mathrm{th}}$ iteration, the signal field $S^{(k)}_{\mathrm{FROG}}(t,T)$ is calculated according to (4.9) from $A^{(k)}(t)$. It is next Fourier transformed with respect to $t$ to give $\widetilde{S}^{(k)}_{\mathrm{FROG}}(F,T)$. At this point, the following frequency-domain constraint is applied giving a new signal field

$$\widetilde{S}'_{\mathrm{FROG}}(F,T) = \sqrt{\widetilde{I}_{\mathrm{FROG}}(F,T)}\,\frac{\widetilde{S}^{(k)}_{\mathrm{FROG}}(F,T)}{|\widetilde{S}^{(k)}_{\mathrm{FROG}}(F,T)|} \tag{4.14}$$

by replacing the magnitude of the signal field $\widetilde{S}^{(k)}_{\mathrm{FROG}}(F,T)$ by the square root of the measured FROG trace $\widetilde{I}_{\mathrm{FROG}}(F,T)$. This signal field is then inverse Fourier transformed with respect to $F$ to give the signal function $S'_{\mathrm{FROG}}(t,T)$. The following time-domain constraint is next applied to give a new guess for the pulse envelope

$A^{(k+1)}(t)$ by minimizing the signal field error defined by

$$\hat{\epsilon}_{\mathrm{FROG}}^{(k)} = \sigma\left(S'_{\mathrm{FROG}}(t_i, T_j), A^{(k+1)}(t_i) G_{\mathrm{FROG}}^{(k+1)}(t_i, T_j)\right) \tag{4.15}$$

with respect to $A^{(k+1)}(t_i)$, where the root mean squared (rms) error is defined by

$$\sigma(X_{ij}, Y_{ij}) = \left\{ \frac{1}{N^2} \sum_{j=1}^{N} \sum_{i=1}^{N} |X_{ij} - Y_{ij}|^2 \right\}^{1/2} \tag{4.16}$$

It is noted that $G_{\mathrm{FROG}}^{(k+1)}(t_i, T_j)$ in (4.9) depends on $A^{(k+1)}(t_i)$ implicitly according to (4.13). This process is iterated until convergence is reached. We have assumed here that the measured FROG trace is given on a $N \times N$ grid, where the time separation between two time points equals $\Delta T = T_{n+1} - T_n$.

A good criterion for convergence of the algorithm is given by the error between the measured and reconstructed FROG trace

$$\epsilon_{\mathrm{FROG}}^{(k)} = \sigma\left(\widetilde{I}_{\mathrm{FROG}}(F_i, T_j), \alpha^{(k)} \left|\widetilde{S}_{\mathrm{FROG}}^{(k)}(F_i, T_j)\right|^2\right) \tag{4.17}$$

where $\alpha^{(k)}$ is a scaling parameter that minimizes the error on each iteration [12]. We note that the frequency separation between two frequency points $\Delta F = F_{n+1} - F_n$ is related to $\Delta T$ by

$$\Delta F = \frac{1}{N \Delta T} \tag{4.18}$$

An error $\epsilon_{\mathrm{FROG}}$ on the order of $10^{-3}$ or smaller usually indicates good pulse reconstruction. A schematic diagram of how the pulse reconstruction algorithm converges is show in Fig. 4.7. We start with a random guess which is usually neither a physical solution of the problem nor does it satisfy the frequency-domain constraint. Applying the steps (1)–(3) indicated in Fig. 4.6 to this initial guess, the guess is projected onto the set of solutions that satisfy the frequency-domain constraint; this projection does however not necessarily have to be a physical solution. After applying the steps (4)–(5) indicated in Fig. 4.6, we try and find the physical solution which is the closest to our projection, i.e., we project our new guess which exists in the set of solutions that

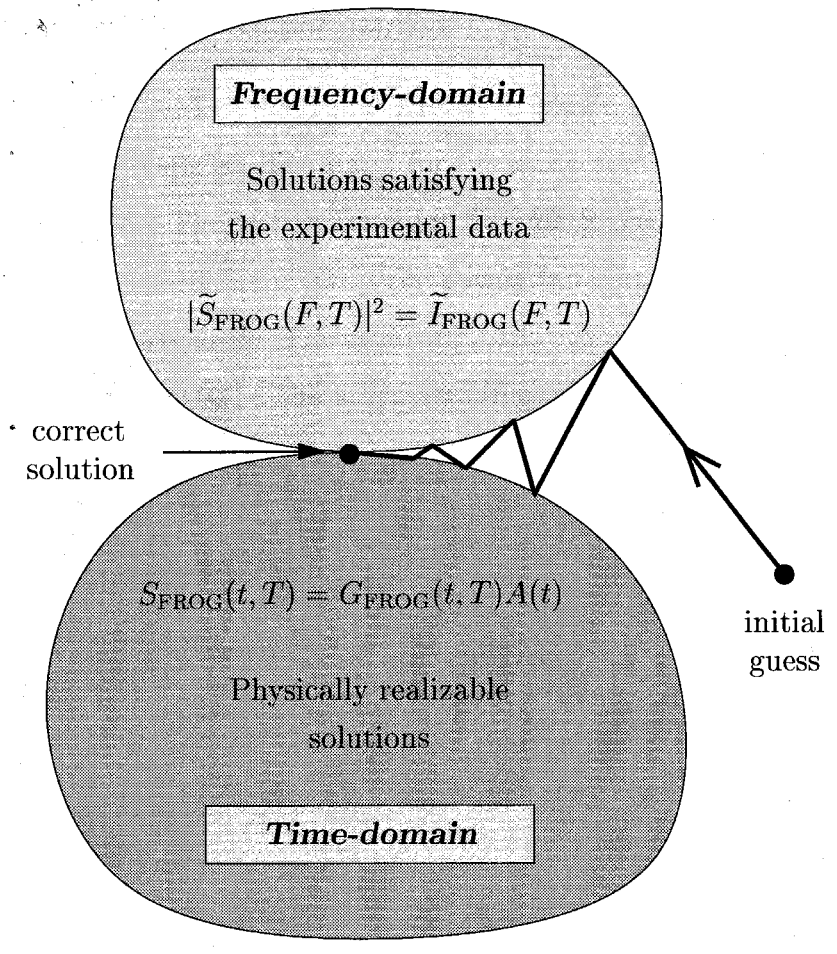


Figure 4.7: Diagram of the convergence of the pulse reconstruction algorithm for FROG.

satisfy the frequency-domain constraint onto the set of physical realizable solutions. This process is then repeated until we reach a solution that satisfies the frequency-domain constraint and that as well is physically realizable. In Fig. 4.7 this solution is indicated by the intersection point between the set of solutions that satisfy the frequency-domain constraint and the set of solutions that are physically realizable. For more information on this method of generalized projections (GP) the reader is referred to [14–17]. The GP method has recently been improved and has resulted in the principal component generalized projections algorithm (PCGPA) [27] which is fast enough to allow real-time inversion of FROG spectrograms [28].

### 4.4.3 FROG based on second harmonic generation (SHG-FROG)

The most commonly used geometry for FROG utilizes a second harmonic generating crystal as its gating element. The setup for the measurement of a SHG-FROG trace is shown in Fig. 4.8. The gating function for this SHG-FROG geometry is given by (4.13a). In the measurement setup the gating function is performed by the SHG crystal in the autocorrelator. The resulting SHG signal is subsequently spectrally analyzed in a spectrometer. The schematic diagram for the SHG-FROG setup is given in Fig. 4.9. Substituting (4.13a) into (4.12) gives the spectogram for this specific setup

$$\widetilde{I}_{\text{SHG-FROG}}(F,T) = \left| \int A(t)A(t-T)\exp(-j2\pi Ft)\,\mathrm{d}t \right|^2 \tag{4.19}$$

Here we have assumed that the resolution of the spectrometer is much smaller than the spectrum of the pulse, i.e., we have made a delta-function approach for the transfer function of the spectrometer. It is noted that experimentally it is a difficult task to try to resolve the spectrum of the SHG signal, especially if the energy of the pulses is limited. Usually a cooled array of photodetectors is needed or the pulses need to be amplified to an appropriate energy level.

Using (4.19) and the definition of our double pulse (4.5), we can calculate the corresponding SHG-FROG trace. The trace has been calculated on a $N \times N$ grid with $N = 128$. The time-step taken is $\Delta T = 0.2t_0$ where $t_0$ is given by (4.6) and the frequency step is given by (4.18). In Fig. 4.10 we have plotted a two-dimensional contour plot of the trace. In order to show the low amplitude features of the trace, we have plotted its square root. The contour lines drawn are at the amplitude levels $1 \cdot 10^{-3}$, $5 \cdot 10^{-2}$ and 0.1 through 1.0 in steps of 0.1. In all of the remaining contour plots in this thesis these levels are used.

Looking at the trace, one can immediately see that the trace is symmetric in the $T = 0$ axis. This brings us to one of the limitations that the measurement of a SHG-FROG trace has. The direction of time for a pulse can not be determined by only measuring the SHG-FROG trace of the pulse. An additional measurement is needed to eliminate this ambuigity in the direction of time. SHG-FROG traces have more

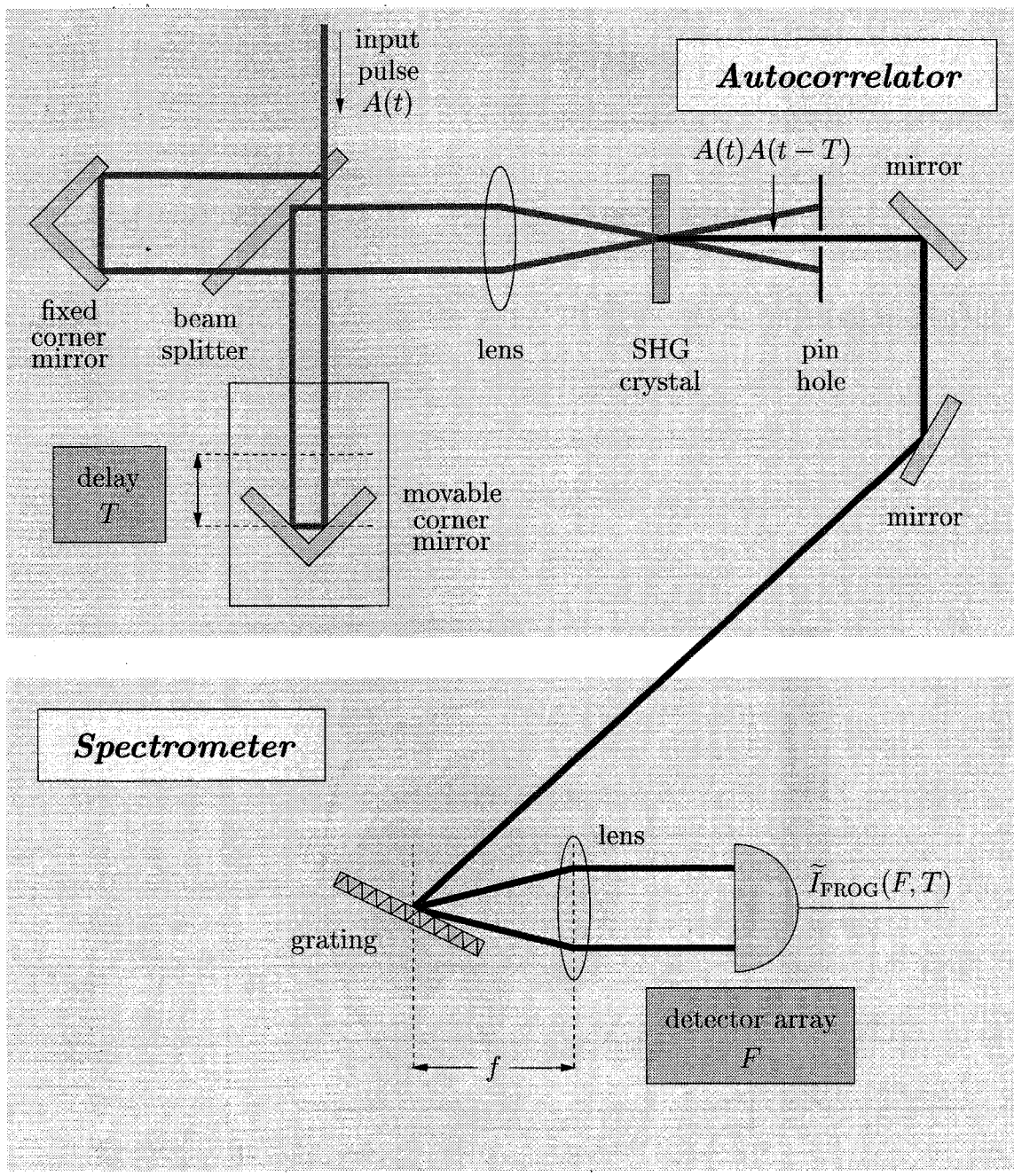


Figure 4.8: SHG-FROG measurement setup consisting of an autocorrelator and a spectrometer.

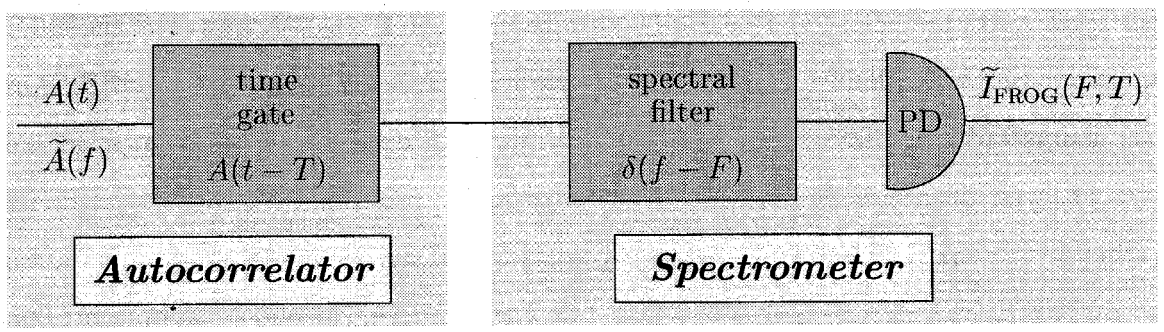


Figure 4.9: Schematic diagram for the SHG-FROG measurement setup consisting of an autocorrelator and a spectrometer.

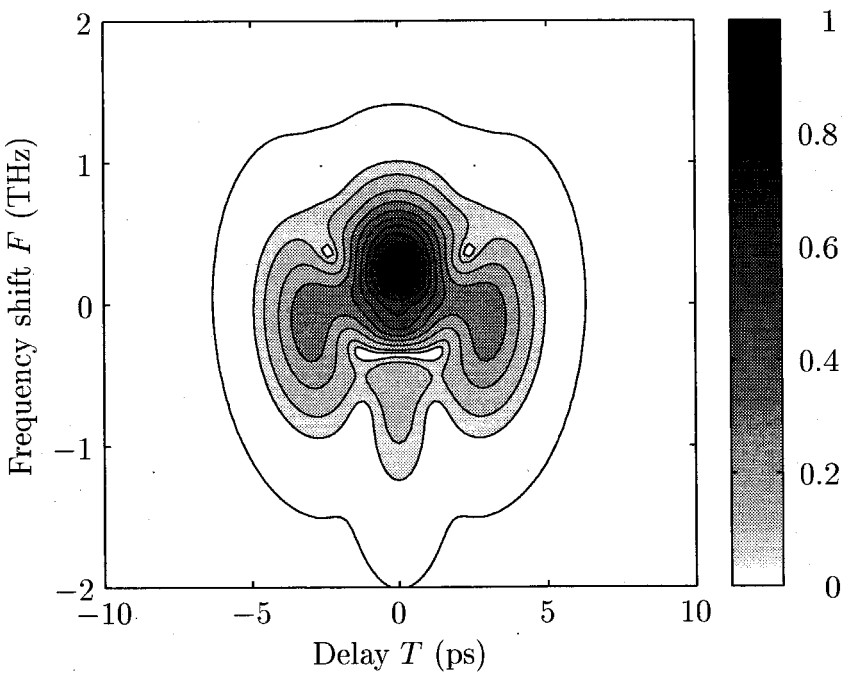


Figure 4.10: Spectrogram $\sqrt{\widetilde{I}_{\text{SHG-FROG}}(F,T)}$ generated from (4.19) for $N = 128$ and $\Delta T = 0.2t_0$.

ambiguities than just an ambiguity in time. These are discussed in Appendix A. In this Appendix it is shown that the reconstruction algorithm can return two possible solutions $A(t)$ and $A^*(-t)$. These two solutions both satisfy (4.19), i.e., they have the same SHG-FROG trace. One can, however, not determine which of the two solutions has been returned by the algorithm and therefore it is not possible to distinguish the direction of time for the pulse. A possible way to overcome this problem is to add a known amount of dispersion to the pulse (in either the time or frequency-domain) and measure a second SHG-FROG trace.

## 4.5 Frequency-domain phase measurement (FDPM)

Another non-interferometric characterization method — frequency-domain phase measurement (FDPM) — was proposed by Chilla and Martinez [29–31]. In this method, a slice of the spectrum of the pulse is selected by a grating and a slit and this spectrally sliced pulse is cross-correlated with the original pulse in a SHG crystal. Cross-correlation traces are then measured for different spectral slices of the pulse. The measurement setup for this method is shown in Fig. 4.11.

This method is similar to the method of frequency-resolved optical gating (FROG) as described in the previous section, except that the role of frequency and time are interchanged: the pulse is first filtered in the frequency domain and then cross-correlation traces of this filtered pulse with the original unfiltered pulse are measured instead of spectra. For FDPM the actual measurements are resolved in the time-domain and it would therefore be more appropriate to put this method in a more general category which we will call time-resolved optical gating (TROG). The method of time-resolved optical gating will be discussed in detail in Chapter 5. In that chapter we show that FDPM can be seen as a measurement setup or geometry for TROG. As we will see in Chapter 5, for the FDPM geometry, the measured traces make up a two-dimensional TROG trace from which the phase and amplitude of the pulse can be retrieved using an iterative algorithm similar to the one that is used for FROG. It is noted that Chilla and Martinez did not use the reconstruction algorithm

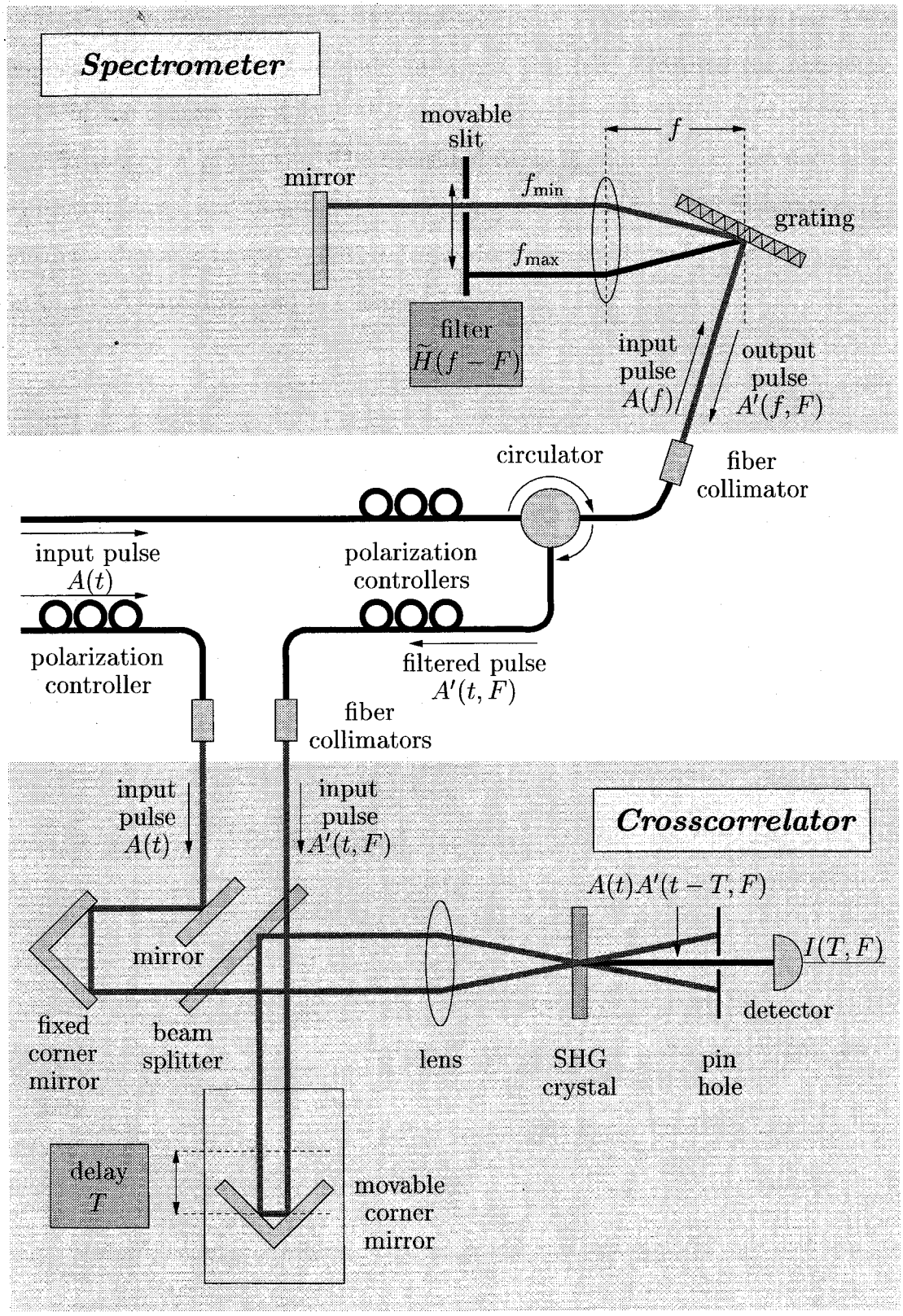


Figure 4.11: FDPM measurement setup consisting of a spectrometer and a crosscorrelator.

as it was not invented yet: it would take two more years before Kane and Trebino established the method [1]. Instead Chilla and Martinez measured the temporal locations of the centers (or delay) of the cross-correlation traces as a function of the center frequency $F$ of the slit. The measured delay is equivalent to the derivative of the spectral phase, and thus the spectral phase can be obtained by integration of the measured delay as a function of frequency. More details of the FDPM method in the light of TROG are discussed in Chapter 5.

## References

[1] D. Kane and R. Trebino, "Characterization of arbitrary femtosecond pulses using frequency-resolved optical gating," *IEEE J. Quantum Electron.*, vol. 29, no. 2, pp. 571–579, 1993.

[2] A. Yariv, *Optical Electronics in Modern Communications.* New York: Oxford University Press, 1997.

[3] K. Sala, G. Kenney-Wallace, and G. Hall, "CW autocorrelation measurements of picosecond laser pulses," *IEEE J. Quantum Electron.*, vol. 16, no. 9, pp. 990–996, 1980.

[4] J. Peatross and A. Rundquist, "Temporal decorrelation of short laser pulses," *J. Opt. Soc. Amer. B*, vol. 15, no. 1, pp. 216–222, 1998.

[5] J. Diels, J. Fontaine, I. McMichael, and F. Simoni, "Control and measurement of ultrashort pulse shapes (in amplitude and phase) with femtosecond accuracy," *Appl. Opt.*, vol. 24, no. 9, pp. 1270–1282, 1985.

[6] K. Naganuma, K. Mogi, and H. Yamada, "General method for ultrashort light-pulse chirp measurement," *IEEE J. Quantum Electron.*, vol. 25, no. 6, pp. 1225–1233, 1989.

[7] C. Yan and J. Diels, "Amplitude and phase recording of ultrashort pulses," *J. Opt. Soc. Amer. B*, vol. 8, no. 6, pp. 1259–1263, 1991.

[8] D. Kane and R. Trebino, "Single-shot measurement of the intensity and phase of an arbitrary ultrashort pulse by using frequency-resolved optical gating," *Opt. Lett.*, vol. 18, no. 10, pp. 823–825, 1993.

[9] K. DeLong and R. Trebino, "Improved ultrashort pulse-retrieval algorithm for frequency-resolved optical gating," *J. Opt. Soc. Amer. A*, vol. 11, no. 9, pp. 2429–2437, 1994.

[10] D. Kane, A. Taylor, R. Trebino, and K. DeLong, "Single-shot measurement of the intensity and phase of a femtosecond UV laser-pulse with frequency-resolved optical gating," *Opt. Lett.*, vol. 19, no. 14, pp. 1061–1063, 1994.

[11] D. Fittinghoff, K. DeLong, R. Trebino, and C. Ladera, "Noise sensitivity in frequency-resolved optical-gating measurements of ultrashort pulses," *J. Opt. Soc. Amer. B*, vol. 12, no. 10, pp. 1955–1967, 1995.

[12] K. DeLong, D. Fittinghoff, and R. Trebino, "Practical issues in ultrashort-laser-pulse measurement using frequency-resolved optical gating," *IEEE J. Quantum Electron.*, vol. 32, no. 7, pp. 1253–1264, 1996.

[13] K. DeLong, R. Trebino, and D. Kane, "Comparison of ultrashort-pulse frequency-resolved-optical-gating traces for 3 common beam geometries," *J. Opt. Soc. Amer. B*, vol. 11, no. 9, pp. 1595–1608, 1994.

[14] J. Fienup, "Phase retrieval algorithms - a comparison," *Appl. Opt.*, vol. 21, no. 15, pp. 2758–2769, 1982.

[15] R. Trebino and D. Kane, "Using phase retrieval to measure the intensity and phase of ultrashort pulses - frequency-resolved optical gating," *J. Opt. Soc. Amer. A*, vol. 10, no. 5, pp. 1101–1111, 1993.

[16] K. DeLong, R. Trebino, J. Hunter, and W. White, "Frequency-resolved optical gating with the use of second-harmonic generation," *J. Opt. Soc. Amer. B*, vol. 11, no. 11, pp. 2206–2215, 1994.

[17] K. DeLong, D. Fittinghoff, R. Trebino, B. Kohler, and K. Wilson, "Pulse retrieval in frequency-resolved optical gating based on the method of generalized projections," *Opt. Lett.*, vol. 19, no. 24, pp. 2152–2154, 1994.

[18] J. Paye, M. Ramaswamy, J. Fujimoto, and E. Ippen, "Measurement of the amplitude and phase of ultrashort light-pulses from spectrally resolved autocorrelation," *Opt. Lett.*, vol. 18, no. 22, pp. 1946–1948, 1993.

[19] J. Paye, "How to measure the amplitude and phase of an ultrashort light-pulse with an autocorrelator and a spectrometer," *IEEE J. Quantum Electron.*, vol. 30, no. 11, pp. 2693–2697, 1994.

[20] T. Tsang, M. Krumbugel, K. DeLong, D. Fittinghoff, and R. Trebino, "Frequency-resolved optical-gating measurements of ultrashort pulses using surface third-harmonic generation," *Opt. Lett.*, vol. 21, no. 17, pp. 1381–1383, 1996.

[21] B. Kohler, V. Yakovlev, K. Wilson, J. Squier, K. DeLong, and R. Trebino, "Phase and intensity characterization of femtosecond pulses from a chirped-pulse amplifier by frequency-resolved optical gating," *Opt. Lett.*, vol. 20, no. 5, pp. 483–485, 1995.

[22] T. Clement, A. Taylor, and D. Kane, "Single-shot measurement of the amplitude and phase of ultrashort laser-pulses in the violet," *Opt. Lett.*, vol. 20, no. 1, pp. 70–72, 1995.

[23] M. Franco, H. Lange, J. Ripoche, B. Prade, and A. Mysyrowicz, "Characterization of ultra-short pulses by cross-phase modulation," *Opt. Commun.*, vol. 140, no. 4-6, pp. 331–340, 1997.

[24] H. Lange, M. Franco, J. Ripoche, B. Prade, P. Rousseau, and A. Mysyrowicz, "Reconstruction of the time profile of femtosecond laser pulses through cross-phase modulation," *IEEE J. Selec. Top. Quantum Electron.*, vol. 4, no. 2, pp. 295–300, 1998.

[25] M. Thomson, J. Dudley, L. Barry, and J. Harvey, "Complete pulse characterization at 1.5 $\mu$m using the Kerr nonlinearity in optical fibers," in *Conference on Lasers and Electro-Optics*, 1998.

[26] J. Dudley, L. Barry, J. Harvey, M. Thomson, B. Thomsen, P. Bollond, and R. Leonhardt, "Complete characterization of ultrashort pulse sources at 1550 nm," *IEEE J. Quantum Electron.*, vol. 35, no. 4, pp. 441–450, 1999.

[27] D. Kane, G. Rodriguez, A. Taylor, and T. Clement, "Simultaneous measurement of two ultrashort laser pulses from a single spectrogram in a single shot," *J. Opt. Soc. Amer. B*, vol. 14, no. 4, pp. 935–943, 1997.

[28] D. Kane, "Real-time measurement of ultrashort laser pulses using principal component generalized projections," *IEEE J. Selec. Top. Quantum Electron.*, vol. 4, no. 2, pp. 278–284, 1998.

[29] J. Chilla and O. Martinez, "Direct determination of the amplitude and the phase of femtosecond light-pulses," *Opt. Lett.*, vol. 16, no. 1, pp. 39–41, 1991.

[30] J. Chilla and O. Martinez, "Analysis of a method of phase measurement of ultrashort pulses in the frequency-domain," *IEEE J. Quantum Electron.*, vol. 27, no. 5, pp. 1228–1235, 1991.

[31] J. Chilla and O. Martinez, "Frequency-domain phase measurement of ultrashort light-pulses - effect of noise," *Opt. Commun.*, vol. 89, no. 5-6, pp. 434–440, 1992.

# CHAPTER 5

# *Time-resolved optical gating based on dispersive propagation: theory*

## 5.1 Introduction

In this chapter we introduce the technique of time resolved optical gating (TROG), a new non-interferometric method for characterizing ultra-short optical pulses in amplitude and phase. TROG is similar to the method of frequency-resolved optical gating (FROG) described in Chapter 4 except that the role of time and frequency is interchanged. We show that frequency-domain phase measurement (FDPM) is a specific measurement setup (also called geometry) for TROG. We introduce a completely new geometry for TROG based on dispersive propagation (DP). This technique can fully characterize an optical pulse in amplitude and phase without the need for a short optical gating pulse. For the DP-TROG geometry we show that measurements of the autocorrelation trace of a pulse after propagation through a medium with variable dispersion together with a single measurement of its intensity spectrum constitute a DP-TROG trace that contains sufficient information to reconstruct the pulse shape in amplitude and phase. The pulse is reconstructed from the measured DP-TROG trace by an iterative algorithm based on generalized projections (GP). The pulse reconstruction for the DP-TROG geometry works very well even for the case of the non-linearly chirped double pulse described in Chapter 4. The DP-TROG geometry makes use of a second order non-linearity that can fully characterize a pulse without

introducing an ambiguity in the direction of time for the pulse. Due to its simplicity and improved sensitivity, DP-TROG is very useful in characterizing low-energy pulses in the $1.3 - 1.5$ $\mu$m wavelength region.

## 5.2 Time-resolved optical gating (TROG)

### 5.2.1 *Basics of TROG*

We now introduce the basics of TROG in a similar fashion as we have done for FROG in Chapter 4. The development of the method of TROG has been inspired by comparing the method of FDPM introduced by Chilla and Martinez [1–3] and the method of FROG introduced by Kane and Trebino [4–9]. If we compare Fig. 4.8 and Fig. 4.11 of Chapter 4 with each other, we see that for the FDPM setup the arrangement of the correlator and the spectrometer is reversed compared to the SHG-FROG setup, i.e., in the FDPM setup we first have a spectral filter (spectrometer) followed by a temporal filter (correlator) while in the FROG setup we have a temporal filter (correlator) followed by a spectral filter (spectrometer); see Fig. 4.5.

In Chapter 4 we have seen that there are various geometries available for FROG; see (4.13). For all these geometries the measurements are performed in the frequency-domain using a spectrometer, hence the name *frequency* resolved optical gating. Looking at the FDPM arrangement, the sequence of the time and frequency elements in the measurement setup is reversed compared to the SHG-FROG setup and the measurements are resolved in the time-domain using a correlator. It thus makes sense to consider the FDPM setup as a specific geometry for a more general category which we will call *time* resolved optical gating. Applying the exchange of the time and frequency elements to Fig. 4.5 gives us the schematic diagram for the measurement of a TROG trace. This schematic diagram is shown in Fig. 5.1.

The first part of the measurement setup is a frequency filter, which can be, for example, a tunable spectral filter or a medium with adjustable dispersion. When the pulse $A(t)$ passes through this element, the complex spectrum of the pulse $\widetilde{A}(f)$ is filtered in the frequency-domain with its filter function $\widetilde{H}_{\mathrm{TROG}}(f, F)$, giving the

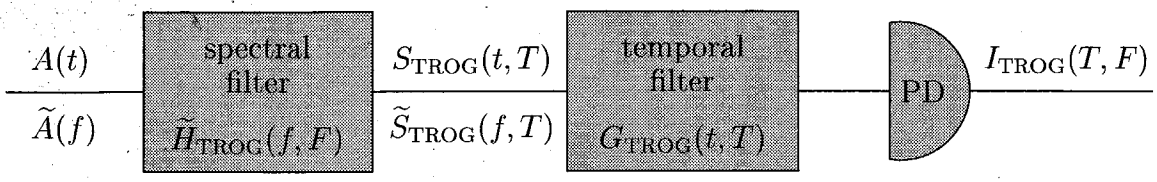


Figure 5.1: Schematic diagram for the TROG measurement setup consisting of a spectral filter followed by a temporal filter and an integrating photo-detector (PD).

signal field at the output of the spectral filter

$$\widetilde{S}_{\mathrm{TROG}}(f,F) = \widetilde{A}(f)\widetilde{H}_{\mathrm{TROG}}(f,F) \tag{5.1}$$

The signal field is next filtered in the time-domain and detected by a square-law and integrating detector. The signal at the output of the detector is given by

$$\begin{aligned} I_{\mathrm{TROG}}(T,F) &= \int |G_{\mathrm{TROG}}(t,T)|^2 \, |S_{\mathrm{TROG}}(t,T)|^2 \, \mathrm{d}t \\ &= \int |G_{\mathrm{TROG}}(t,T)|^2 \left| \int \widetilde{A}(f)\widetilde{H}_{\mathrm{TROG}}(f,F) \exp(j2\pi ft) \, \mathrm{d}f \right|^2 \mathrm{d}t \end{aligned} \tag{5.2}$$

If the temporal filter acts as a time-gate, i.e., we apply the delta-function approach

$$|G_{\mathrm{TROG}}(t,T)|^2 \to \delta(t-T) \tag{5.3}$$

(5.2) can be simplified into

$$I_{\mathrm{TROG}}(T,F) = \left| \int \widetilde{A}(f)\widetilde{H}_{\mathrm{TROG}}(f,F) \exp(j2\pi fT) \, \mathrm{d}f \right|^2 \tag{5.4}$$

This quantity is called the TROG trace or sonogram of the input pulse; if the spectral filter function is narrow enough, it measures the temporal intensity of different spectral components of the pulse. We note the time-frequency duality of (5.1), (5.2) and (5.4) with (4.9), (4.10) and (4.12) respectively. In all these equations the role of time and frequency is exchanged, i.e., $t \longleftrightarrow f$ and $T \longleftrightarrow F$.

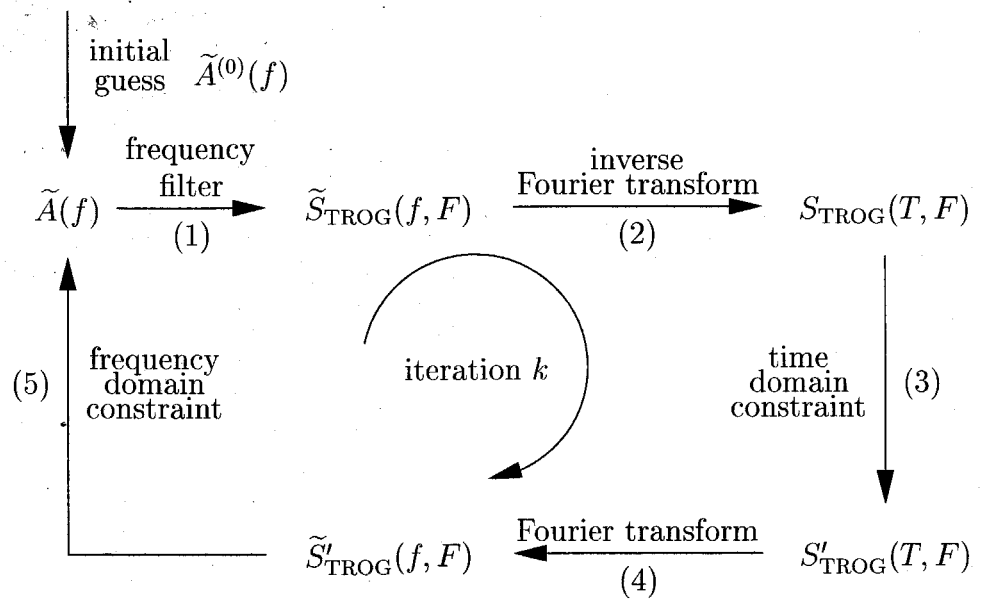


Figure 5.2: Diagram of the pulse reconstruction algorithm for TROG.

### 5.2.2 *Pulse reconstruction algorithm for TROG*

Using the fact that TROG is the time-domain counterpart of FROG, we can design an algorithm which can retrieve the pulse shape and phase from a TROG trace or sonogram similar to the algorithm that FROG uses. A diagram of this new pulse reconstruction algorithm for TROG is shown in Fig. 5.2. This algorithm is derived from the FROG algorithm shown in Fig. 4.6 by applying the time-frequency duality between TROG and FROG. This translates into the following. The algorithm is started from an initial random guess for the complex spectrum of the pulse $\widetilde{A}^{(0)}(f)$ instead of the complex pulse shape $A^{(0)}(t)$. On the $k^{\mathrm{th}}$ iteration, the signal field $\widetilde{S}^{(k)}_{\mathrm{TROG}}(f,F)$ is calculated according to (5.1) from $\widetilde{A}^{(k)}(f)$. It is next inverse Fourier transformed with respect to $f$ to give $S^{(k)}_{\mathrm{TROG}}(T,F)$. At this point, the following time-domain constraint is applied giving a new signal field

$$S'_{\mathrm{TROG}}(T,F) = \sqrt{I_{\mathrm{TROG}}(T,F)}\,\frac{S^{(k)}_{\mathrm{TROG}}(T,F)}{|S^{(k)}_{\mathrm{TROG}}(T,F)|} \tag{5.5}$$

by replacing the magnitude of the signal field $S^{(k)}_{\mathrm{TROG}}(T,F)$ by the square root of the measured TROG trace $I_{\mathrm{TROG}}(T,F)$. This signal field is then Fourier transformed

with respect to $T$ to give the signal function $\widetilde{S}'_{\mathrm{TROG}}(f,F)$. The following frequency-domain constraint is next applied to give a new guess for the pulse envelope $\widetilde{A}^{(k+1)}(f)$ by minimizing the signal field error defined by

$$\hat{\varepsilon}^{(k)}_{\mathrm{TROG}} = \sigma\left(\widetilde{S}'_{\mathrm{TROG}}(f_i,F_j), \widetilde{A}^{(k+1)}(f_i)\widetilde{H}^{(k+1)}_{\mathrm{TROG}}(f_i,F_j)\right) \tag{5.6}$$

with respect to $\widetilde{A}^{(k+1)}(f_i)$. This process is iterated until convergence is reached. A good criterion for convergence of the algorithm is given by the error between the measured and reconstructed TROG trace

$$\varepsilon^{(k)}_{\mathrm{TROG}} = \sigma\left(I_{\mathrm{TROG}}(T_i,F_j), \alpha^{(k)}\left|S^{(k)}_{\mathrm{FROG}}(T_i,F_j)\right|^2\right) \tag{5.7}$$

An error $\varepsilon_{\mathrm{TROG}}$ on the order of $10^{-3}$ or smaller usually indicates good pulse reconstruction.

A schematic diagram of how the pulse reconstruction algorithm for TROG converges is shown in Fig. 5.3. It is noted that this diagram is similar to the diagram shown in Fig. 4.7, but note that the solution sets for the time and frequency-domain have been exchanged. We start again from a random guess which is usually not a physical solution of the problem. It usually does not satisfy the time-domain constraint either. Applying the steps (1)–(3) indicated in Fig. 5.2 to this initial guess, the guess is projected onto the set of solutions that satisfy the time-domain constraint; this projection does not necessarily have to be a physical solution. After applying the steps (4)–(5) indicated in Fig. 5.2, we try to find the physical solution which is the closest to our projection, i.e., we project our new guess which exists in the set of solutions that satisfy the time-domain constraint onto the set of physical realizable solutions which exist in the frequency-domain. This process is then repeated until we reach a solution that satisfies the time-domain constraint and that as well is physically realizable. In Fig. 5.3 this solution is indicated by the intersection point between the set of solutions that satisfy the time-domain constraint and the set of solutions that are physically realizable.

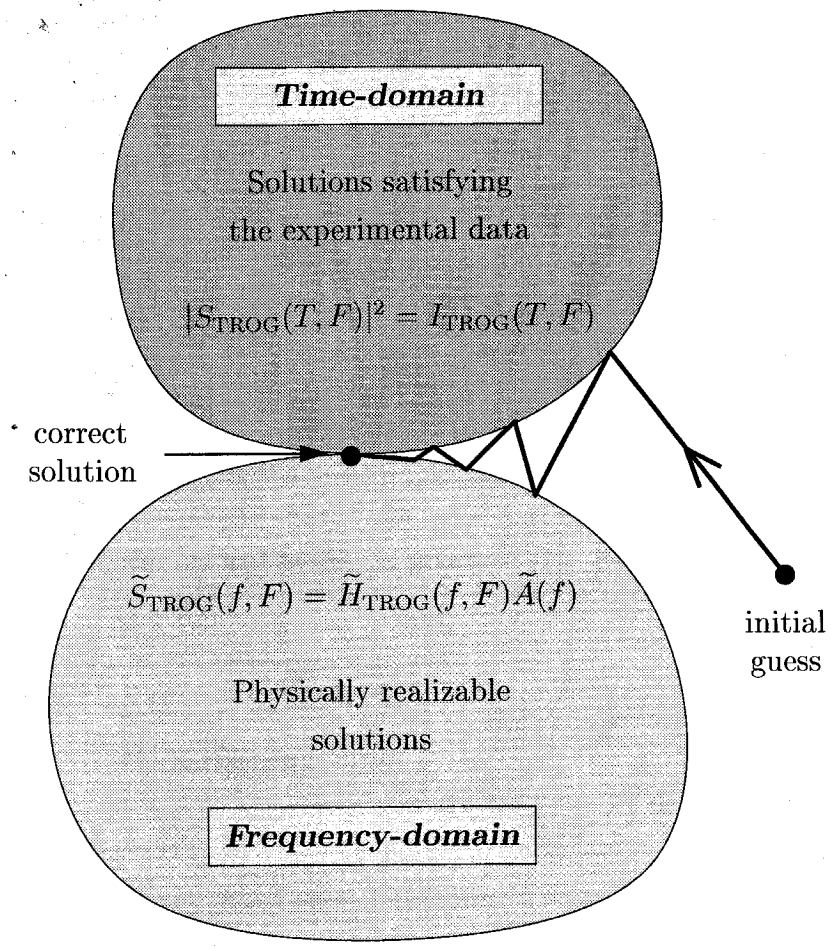


Figure 5.3: Diagram of the convergence of the pulse reconstruction algorithm for TROG.

### 5.2.3 FDPM as a measurement geometry for TROG

To date only one TROG geometry has been demonstrated: frequency-domain phase measurement (FPDM). Its name might be misleading and imply that it is a frequency-resolved measurement, but as explained in the previous section it is actually a time-resolved measurement (correlation traces are measured). In this section we look back on the method of FDPM which has been described in Section 4.5. FDPM can be classified as a specific geometry for TROG. In order to clarify this a bit further, we have drawn a schematic measurement diagram in Fig. 5.4. In the experiment of Chilla and Martinez (see Fig. 4.11), the frequency gating is performed by a grating and a slit [1, 2]. An exact transfer function of this grating/slit pair, taking into account the

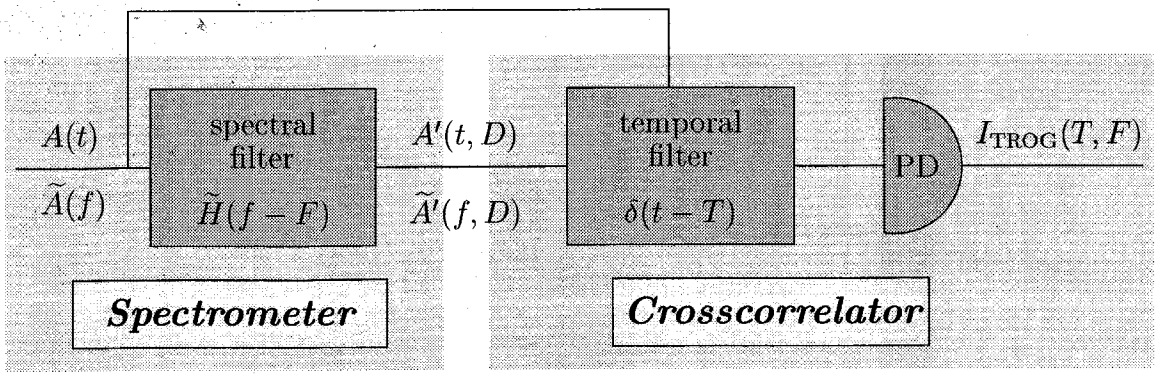


Figure 5.4: Schematic diagram for the FDPM-TROG measurement setup consisting of a spectrometer and a crosscorrelator.

spatial variation of the optical beam, is given in [2]. For a slit size larger than the beam size, this transfer function can be simplified to a rectangle function

$$\widetilde{H}_{\text{FDPM-TROG}}(f,F) = \begin{cases} 1 & \text{for } |f-F| \leq \frac{1}{2}F_0 \\ 0 & \text{for } |f-F| > \frac{1}{2}F_0 \end{cases} \tag{5.8}$$

where $F_0$ is the frequency passband of the slit. The pulse at the output of the slit is crosscorrelated with the original pulse in a SHG crystal. If the width of the slit is small enough so that the duration of the resulting pulse that exits the spectral filter is much longer than the original input pulse $A(t)$, the original pulse $A(t)$ can be considered as a delta-function in comparison to the pulse that exits the spectral filter. In that case the temporal transfer function of the temporal filter (the crosscorrelator) will approach a delta-function, $|G_{\text{FDPM-TROG}}(t,T)|^2 \rightarrow \delta(t-T)$, and the detected signal is given by

$$I_{\text{FDPM-TROG}}(T,F) = \left| \int \widetilde{A}(f)\widetilde{H}_{\text{FDPM-TROG}}(f,F)\exp(j2\pi fT)\,\mathrm{d}f \right|^2 \tag{5.9}$$

where $\widetilde{H}_{\text{FDPM-TROG}}$ is defined according to (5.8). The time-frequency duality of (5.9) and (4.12) is noted again.

Now that we have shown that FDPM can be classified as a TROG geometry, we will refer to FDPM as FDPM-TROG in the rest of this thesis. Using (5.9) and

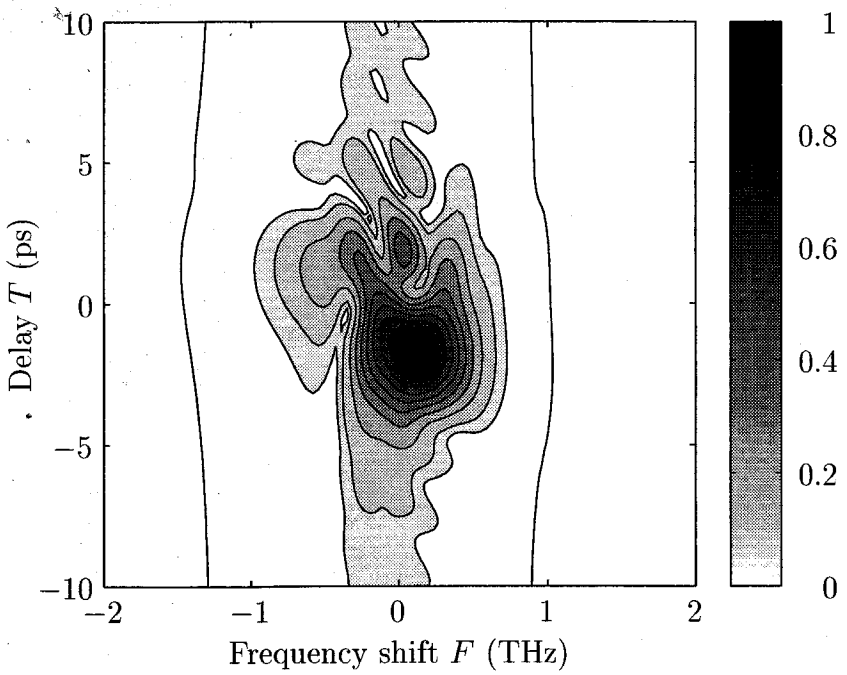


Figure 5.5: Sonogram $\sqrt{I_{\text{FDPM-TROG}}(T,F)}$ trace generated from (5.9) for $N = 128$ and $\Delta T = 0.2t_0$ and $F_0 = 10\Delta F$.

the definition of our double pulse (4.5), we can calculate the corresponding FDPM-TROG trace or sonogram of the pulse. The trace has been calculated on a $N \times N$ grid with $N = 128$. The time-step taken is $\Delta T = 0.2t_0$ where $t_0$ is given by (4.6) and the frequency step $\Delta F$ is given by (4.18). The result is shown in Fig. 5.5. For this particular example we have given the rectangle function of (5.8) a width of $F_0 = 10\Delta F$. It is noted that the FDPM-TROG trace does not contain any symmetry properties. The pulse reconstruction algorithm can only return the solution $A(t)$ and has therefore no ambiguities in the direction of time.

Some remarks with respect to the FDPM-TROG measurement setup are in place here. Although Chilla and Martinez state that better spectral resolution and phase reconstruction is obtained with a narrower slit, it can be shown that this is not necessary if the pulse reconstruction algorithm uses the entire detected signal of (5.9) instead of just the temporal locations of the centers of the crosscorrelation traces. There is an upper limit to the slit width though: the spectrally filtered pulse needs to be much longer in duration than the original pulse in order for the original pulse

to act as a delta-function. It is also noted that the slit size can not be infinitely small. In that case the spectral gating function would behave as a delta-function, $\widetilde{H}_{\text{FDPM-TROG}}(f,F) \rightarrow \delta(f-F)$ and the TROG trace would yield the spectral intensity of the pulse.

$$I_{\text{FDPM-TROG}}(T,F) = |\widetilde{A}(F)|^2 \tag{5.10}$$

Pulse reconstruction is impossible in that case. For this case diffraction effects of the slit can not be neglected either.

## 5.3 Time-resolved optical gating based on dispersive propagation (DP-TROG)

### 5.3.1 *Dispersive propagation: a new TROG geometry (DP-TROG)*

We propose a new measurement setup for TROG. The method makes use of dispersive propagation (DP). A schematic diagram of the DP-TROG geometry is pictured in Fig. 5.6. The setup consists of a spectral filter (the disperser), also called a phase stationary (PS) filter, followed by a temporal filter (the autocorrelator), also called an amplitude non-stationary (ANS) filter, and a square-law integrating detector.

A few comments with respect to previous work are in place here. A linear filter analysis of both interferometric and non-interferometric methods for ultra-short pulse

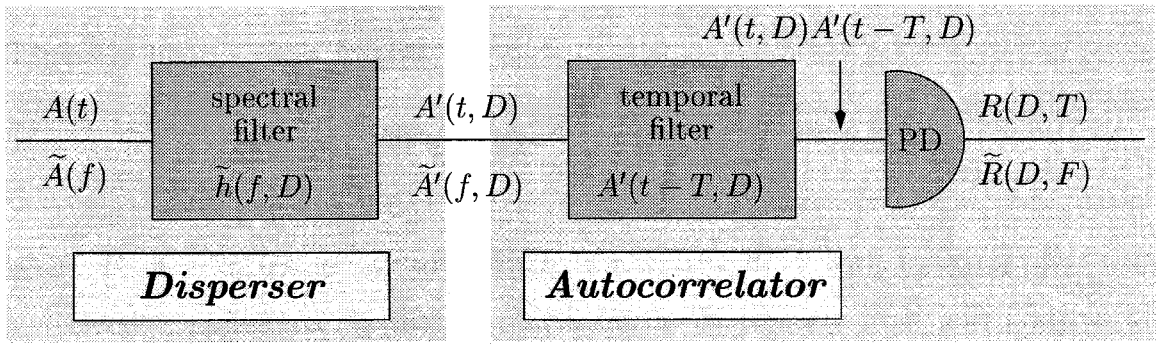


Figure 5.6: Schematic diagram of the measurement setup for DP-TROG consisting of a disperser followed by an autocorrelator and an integrating photo-detector (PD). The functions $\widetilde{h}(f,D)$ and $A'(t,D)$ are defined by (5.11) and (5.18) respectively.

measurement has been described extensively by Wong and Walmsley [10–13]. The key result of their analysis for non-interferometric methods is that a measurement setup with a square-law integrating detector needs to consist of at least one time stationary and one time non-stationary filter in order to reconstruct the pulse shape. In [12] four minimum-filter measurement techniques are described and these devices are indicated with Roman numerals I-IV. Adopting this notation, most FROG geometries are classified as type I devices while the FDPM-TROG geometry is classified as a type II device. According to Wong and Walmsley, our new DP-TROG geometry would fall in the category of type IV (PS-ANS) devices [12]. Wong and Walmsley state that type IV devices require a short time-gate duration in order to be able to reconstruct the pulse with help of the inverse Radon transform (IRT) [12]. The DP-TROG geometry contradicts this requirement, however, as it measures a set of *autocorrelation* traces $A'(t,D)A'(t-T,D)$ of the dispersed pulse instead of *crosscorrelation* traces of the pulse with a short gating pulse. It also uses the TROG algorithm for reconstruction instead of the IRT algorithm.

In the measurement setup of Fig. 5.6, the spectral filter is a medium with variable dispersion. Variable dispersive propagation could, for example, be accomplished by a grating pair disperser [14], a set of prisms [15], or a number of normal/anomalous dispersive fibers each with a different length. Without loss of generality, we will consider the case where the dispersive propagation takes place in a set of fibers each with a different amount of dispersion. The spectral transfer function for a piece of dispersive fiber is given by [16]

$$\widetilde{h}(f,D) = \exp(j\pi f^2 D) \tag{5.11}$$

where $D = -2\pi\beta_2 L$ is the total dispersion of the fiber with length $L$ and with a dispersion parameter $\beta_2$ that is ($\beta_2$) negative for regular fiber and positive for dispersion compensating fiber. The autocorrelator measures the autocorrelation trace of the dispersed pulse $A'(t,D)$. The output of the photodetector (PD) is the integral

of the intensity $|A'(t,D)A'(t,D)|^2$ at its input and is given by [16, 17]

$$R(D,T) = \int |A'(t,D)|^2 |A'(t-T,D)|^2 \,\mathrm{d}t \tag{5.12}$$

where $T$ is the delay of the autocorrelator. The Fourier transform of $R(D,T)$ with respect to $T$ can be written as

$$\widetilde{R}(D,F) = \iint |A'(t,D)|^2 |A'(t-T,D)|^2 \exp(-j2\pi FT)\,\mathrm{d}t\,\mathrm{d}T \tag{5.13}$$

Substituting $\tau = t - T$ gives

$$\begin{aligned}
\widetilde{R}(D,F) &= \int |A'(t,D)|^2 \exp(-j2\pi Ft)\,\mathrm{d}t \int |A'(\tau,D)|^2 \exp(j2\pi F\tau)\,\mathrm{d}\tau \\
&= \left| \int |A'(t,D)|^2 \exp(-j2\pi Ft)\,\mathrm{d}t \right|^2 \\
&= \left| \int A'(t,D)A'^*(t,D) \exp(-j2\pi Ft)\,\mathrm{d}t \right|^2
\end{aligned} \tag{5.14}$$

Using the convolution theorem for Fourier transforms this can be rewritten as

$$\widetilde{R}(D,F) = \left| \int \widetilde{A}'(f,D)\widetilde{A}'^*(f-F,D)\,\mathrm{d}f \right|^2 \tag{5.15}$$

Using

$$\begin{aligned}
\widetilde{A}'(f,D) &= \widetilde{A}(f)\widetilde{h}(f,D) \\
&= \widetilde{A}(f)\exp(j\pi f^2 D)
\end{aligned} \tag{5.16}$$

we can rewrite (5.15) as

$$\begin{aligned}
\widetilde{R}(D,F) &= \left| \int \widetilde{A}(f)\exp(j\pi f^2 D)\widetilde{A}^*(f-F)\exp(-j\pi(f-F)^2 D)\,\mathrm{d}f \right|^2 \\
&= \left| \int \widetilde{A}(f)\widetilde{A}^*(f-F)\exp(j2\pi fFD)\,\mathrm{d}f \right|^2
\end{aligned} \tag{5.17}$$

We note that the pulse shape that exits the spectral filter is given by inverse

Fourier transformation of (5.16)

$$A'(t,D) = \int \widetilde{A}(f)\exp(j\pi f^2 D)\exp(j2\pi ft)\,\mathrm{d}f \tag{5.18}$$

Comparing (5.17) with (5.9) we see that the Fourier transform of the autocorrelation trace $\widetilde{R}(D,F)$ is a scaled version of a DP-TROG trace defined by

$$I_{\text{DP-TROG}}(T,F) = \left|\int \widetilde{A}(f)\widetilde{H}_{\text{DP-TROG}}(f,F)\exp(j2\pi fT)\,\mathrm{d}f\right|^2 \tag{5.19}$$

For

$$\widetilde{H}_{\text{DP-TROG}}(f,F) = \widetilde{A}^*(f-F) \tag{5.20}$$

and $T = FD$, the scaling is given by

$$I_{\text{DP-TROG}}(T,F) = \widetilde{R}(T/F,F) \tag{5.21}$$

It is noted that our new method does not measure the DP-TROG trace directly. Instead it measures the set of autocorrelation traces $R(D,T)$ which can be transformed into the DP-TROG trace defined by (5.19)–(5.20) according to (5.21). Mathematically this transformation entails Fourier transforming the measured set of autocorrelation traces $R(D,T)$ with respect to $T$ to give $\widetilde{R}(D,F)$ and next interpolating this trace at points $(T_i/F_j, F_j)$ such that $\Delta T$ and $\Delta F$ are related by (4.18).

It is noted that interpolation of the trace with $F = 0$

$$\begin{aligned} I_{\text{DP-TROG}}(T,0) &= \left|\int |\widetilde{A}(f)|^2\exp(j2\pi fT)\,\mathrm{d}f\right|^2 \\ &= \left|\int \widetilde{I}(f)\exp(j2\pi fT)\,\mathrm{d}f\right|^2 \end{aligned} \tag{5.22}$$

is not possible. From (5.22) it can however easily be seen that this trace is obtained by measuring the intensity spectrum $\widetilde{I}(f)$ of the original pulse, inverse Fourier transforming it with respect to $f$ and finally taking the norm squared.

The pulse shape can next be retrieved from the TROG trace of (5.21) by the

iterative TROG algorithm depicted in Fig. 5.2. It can thus be concluded that measurement of the autocorrelation traces of dispersed versions of the original pulse intensity together with the spectrum of the original pulse provide enough information to reconstruct the pulse in amplitude and phase. In the next section, we will show how well the pulse reconstruction works in the case of a test pulse which we choose as a non-linearly chirped double pulse.

### 5.3.2 Pulse reconstruction algorithm for DP-TROG

In this section we demonstrate how the pulse reconstruction works for our double pulse introduced in Chapter 4. As a first step, the DP-TROG trace is calculated theoretically according to (5.19) and (5.20) on a $N \times N$ grid with $N = 128$. The time step taken is $\Delta T = 0.2\, t_0$ and the frequency step $\Delta F$ is given by (4.18). The number of points $N$ and the time step $\Delta T$ need to be taken such that the total frequency range covered is large enough to contain the spectrum of the pulse and the total time range covered is large enough to contain the pulse shape. In our case $N = 128$ is sufficient. The calculated DP-TROG trace is shown in Fig. 5.7. In order to show the low amplitude features of the trace, we have plotted its square root. Although the DP-TROG trace has certain ambiguities (see Appendix B), it does not have an ambiguity in the direction of time in contrast to SHG-FROG where the direction of time for the pulse can not be distinguished; see [4] and Appendix A. The sign of the chirp is therefore directly revealed by the orientation of the trace in Fig. 5.7: the frequency decreases for increasing time, i.e., the pulse contains a down-chirp. The algorithm used to reconstruct the pulse from the DP-TROG trace has been discussed in Section 5.3.2. We have both implemented the reconstruction algorithm that is based on the basic method of GP [18–21] as well as the faster PCGPA [22]. For the basic GP algorithm, on each iteration the algorithm finds a new guess for the next iteration by minimizing (5.6) with respect to the real and imaginary parts of $\widetilde{A}(f)$. The minimization method used is a $2N$-dimensional conjugate gradient method. We apply the standard Fletcher-Reeves minimization method [23], which involves a num-

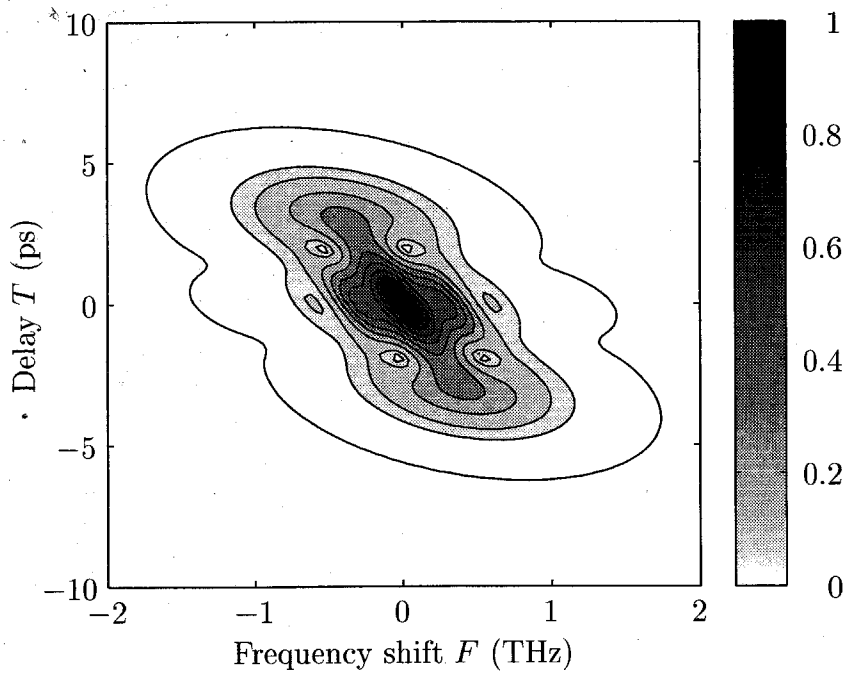


Figure 5.7: Sonogram $\sqrt{I_{\text{DP-TROG}}(T,F)}$ generated from (5.19) and (5.20) for $N = 128$ and $\Delta T = 0.2t_0$

ber of one-dimensional minimizations along directions that are selected with help of the gradient of $\widehat{\varepsilon}_{\text{TROG}}$ defined in (5.6). Although the gradient with respect to the real and imaginary parts of $\widetilde{A}(f)$ can be calculated numerically, the algorithm is sped up considerably by calculating an analytical expression for this gradient in a manner similar as presented in [6]. We note that this analytical expression depends on the form of the signal field $\widetilde{S}_{\text{TROG}}(f,F)$ defined in (5.1) and needs to be calculated individually for a given measurement geometry. When one uses the PCGPA the calculation of the analytical expression for the gradient can be avoided. The algorithm uses a singular value decomposition instead. Typically one iteration takes approximately a second on a 500 MHz Pentium computer.

For the theoretically calculated TROG trace, the algorithm converges to the exact pulse shape (see the triangles in Fig. 5.8 and Fig. 5.9) with a very small residual error $\varepsilon_{\text{TROG}}$ on the order of $10^{-5}$ (see the solid line in Fig. 5.10). For the initial guess, a random amplitude uniformly distributed on $[0,1]$ and a random phase uniformly distributed on $[-\pi,\pi]$ are chosen in the frequency-domain.

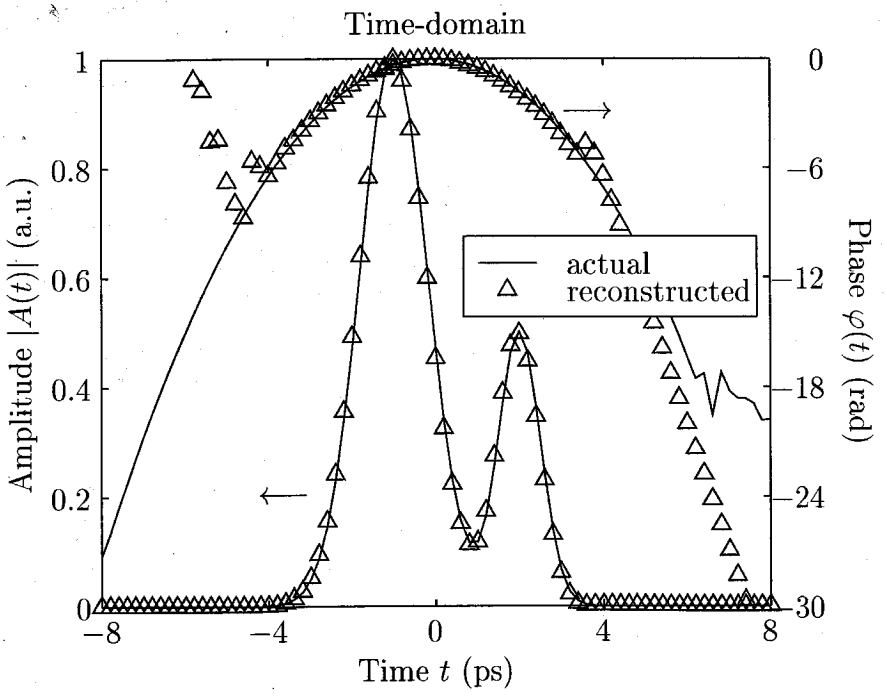


Figure 5.8: Amplitude and phase of the non-linearly chirped double pulse represented in the time-domain: actual pulse (solid line) and reconstructed pulse (triangles) using the sonogram of Fig. 5.7.

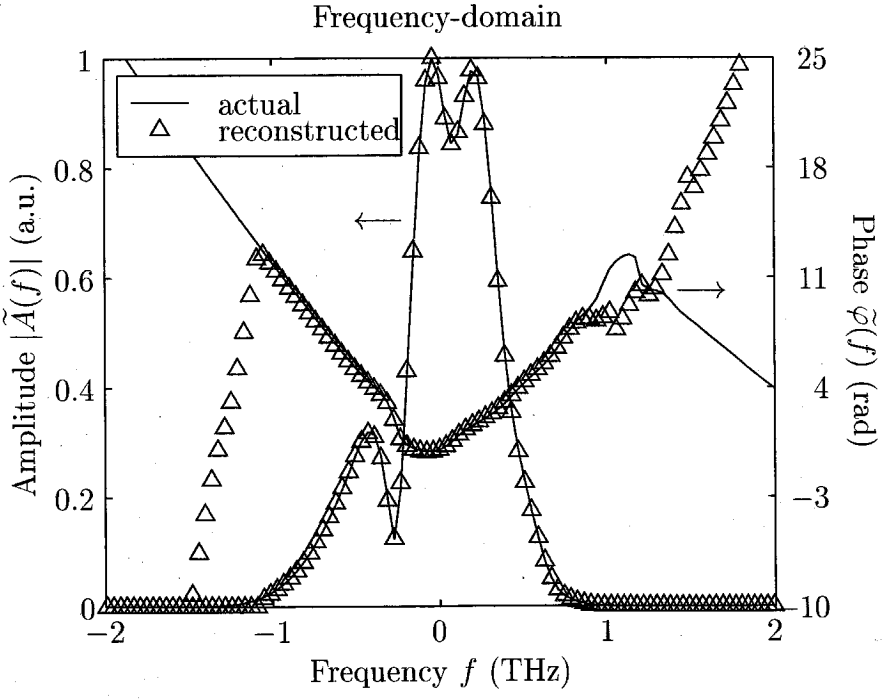


Figure 5.9: Amplitude and phase of the non-linearly chirped double pulse represented in the frequency-domain: actual pulse (solid line) and reconstructed pulse (triangles) using the sonogram of Fig. 5.7.

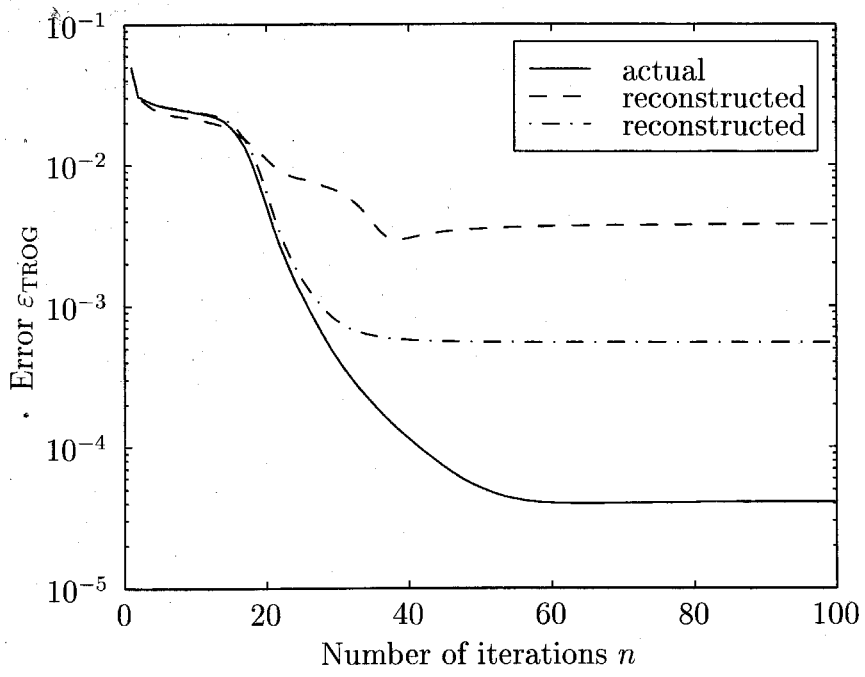


Figure 5.10: The evolution of the convergence error defined in (5.7): the solid line shows the error when the theoretically calculated sonogram of Fig. 5.7 is used as input, the dashed line shows the error when the sonogram of Fig. 5.13 is used, and the dotted-dash line, when the sonogram of Fig. 5.14 is used.

It is noted that the retrieved pulse can be a time-shifted version of the actual pulse as the TROG trace is invariant to time-shifts. A shift in time of $\Delta t$ adds a linear phase $\widetilde{\psi}(f) = -2\pi\Delta t f$ to the pulse in the frequency-domain. If the retrieved pulse needs to be shifted to coincide with the actual pulse in the time-domain (as is done in Fig. 5.8), the linear phase $\widetilde{\psi}(f)$ needs to be subtracted in the frequency-domain in order to obtain the correct phase of the pulse.

As a next step we have constructed the TROG trace from the autocorrelation traces and the intensity spectrum of the dispersed pulse. The autocorrelation trace is calculated from (5.12) for different lengths of fiber. The dispersion parameter for regular fiber is taken as $\beta_2 = -22.6$ ps$^2$km$^{-1}$ while the step size in fiber length equals $\Delta L = 2$ m. The total dispersion is calculated according to $D = -2\pi\beta_2 L$. Negative total dispersion ($D < 0$) can be experimentally obtained by using dispersion compensating fiber ($\beta_2 > 0$). A two-dimensional view of the resulting set of autocorrelation traces is shown in Fig. 5.11. As expected, the pulse can be compressed with dispersion

compensating fiber due to its down-chirp. A minimum pulse width is achieved after propagation through $L = 12$ m of fiber. The spectrum $\widetilde{R}(D, F)$ of the autocorrelation trace is obtained by Fourier transformation of the trace of Fig. 5.11 with respect to $T$. Its result is shown in Fig. 5.12.

The DP-TROG trace is now obtained by scaling the trace in Fig. 5.12 according to (5.21). We have accomplished this by doing $N - 1$ one-dimensional interpolations in the $T$-direction. As stated before, the trace with $F = 0$ can not be interpolated in this way but is replaced with the trace obtained by calculating (5.22). The result of this scaling is shown in Fig. 5.13. Looking at Fig. 5.13, there appears to be data missing in the TROG trace around $F = 0$. This is due to the limited range of the dispersion $D$ over which the autocorrelation trace is calculated. The area of missing data can be decreased by increasing this dispersion range. This might however be impractical in some experimental situations, especially if the range over which the dispersion can be varied is limited. This TROG trace is next used as input to the reconstruction algorithm. The time-domain constraint (5.5) is applied only on the areas of the TROG trace where data are present. The pulse reconstruction results are shown in Fig. 5.15 and Fig. 5.16 by the triangles. The final convergence error is about $\epsilon_{\text{TROG}} \approx 4 \times 10^{-3}$ (see dashed line in Fig. 5.10). It can be seen from Fig. 5.16 (triangles) that although there is a slight deviation in the intensity spectrum of the pulse, the algorithm reconstructs the spectral phase accurately. The mismatch in the intensity spectrum is caused by the limited dispersion range over which the autocorrelation traces are calculated. Running the algorithm on various dispersion ranges, it is found that the spectral phase is retrieved correctly while the mismatch in the intensity spectrum decreases if the dispersion range is increased. The dispersion range over which measurements should be made depends on the characteristics of the pulse that is being measured, but a good rule of thumb is as follows: find the amount of dispersion that compresses the pulse to its minimum autocorrelation width, then keep increasing the dispersion range around this dispersion amount until the measured autocorrelation trace has dropped its peak value to about one-tenth of the peak value that would occur when the pulse is at its minimum autocorrelation width.

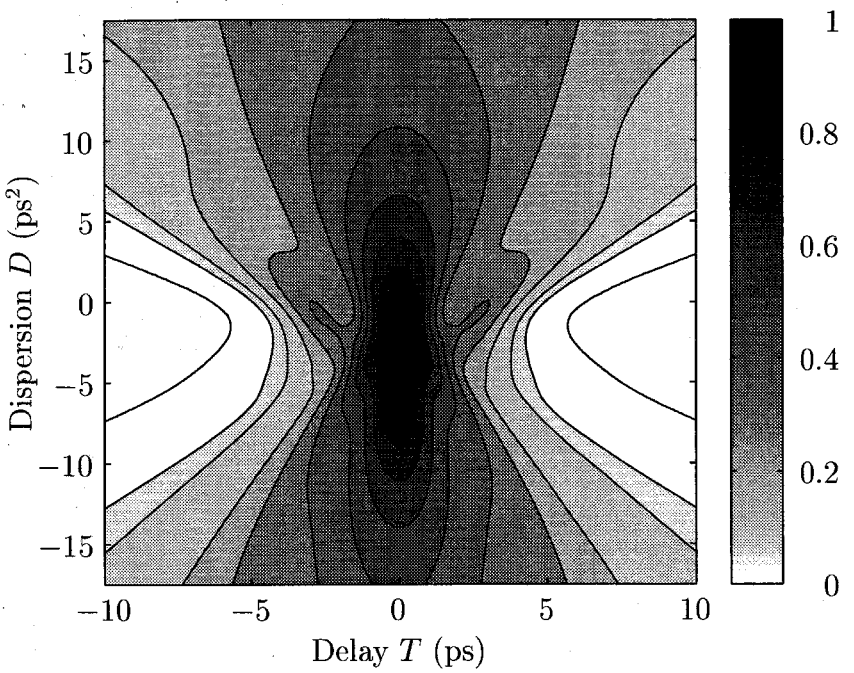


Figure 5.11: Two-dimensional view of the set of autocorrelation traces $\sqrt{R(D,T)}$, theoretically calculated from (5.12).

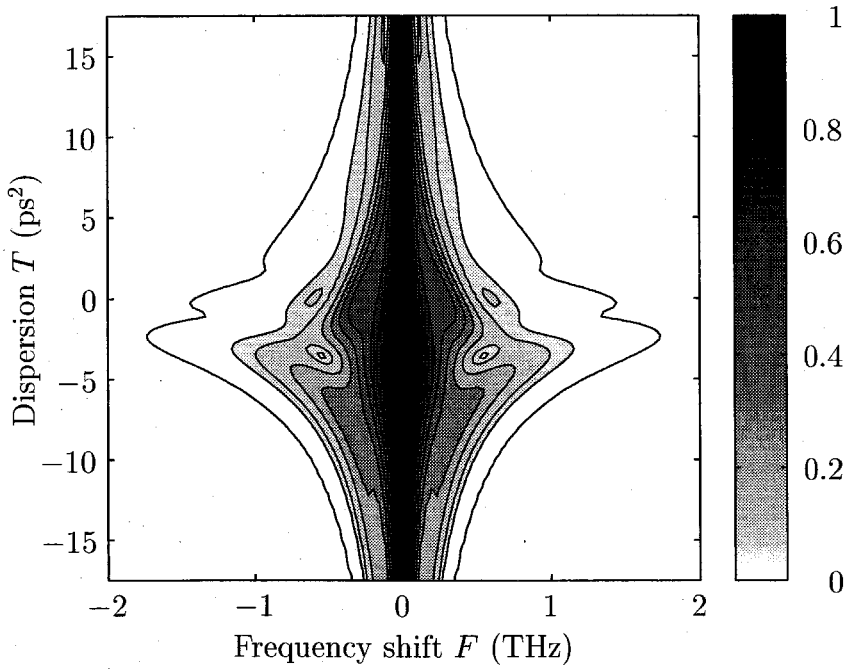


Figure 5.12: Autocorrelation spectrum $\sqrt{\widetilde{R}(D,F)}$ obtained by Fourier transformation of the autocorrelation traces of Fig. 5.11 with respect to $T$.

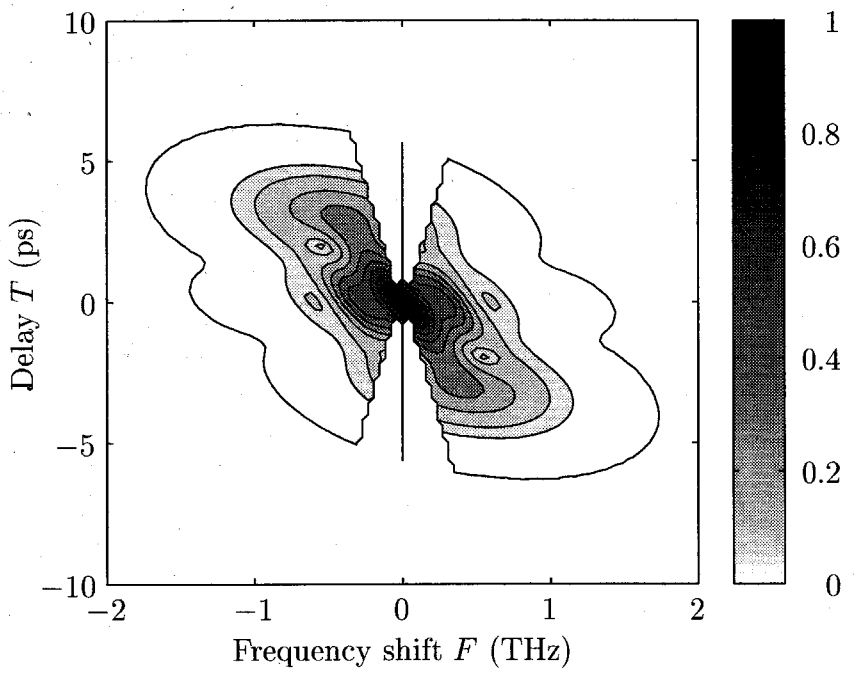


Figure 5.13: Sonogram obtained by interpolating the autocorrelation spectrum of Fig. 5.12 in the $T$-direction according to (5.21) for $F \neq 0$. The trace for $F = 0$ is obtained from (5.22).

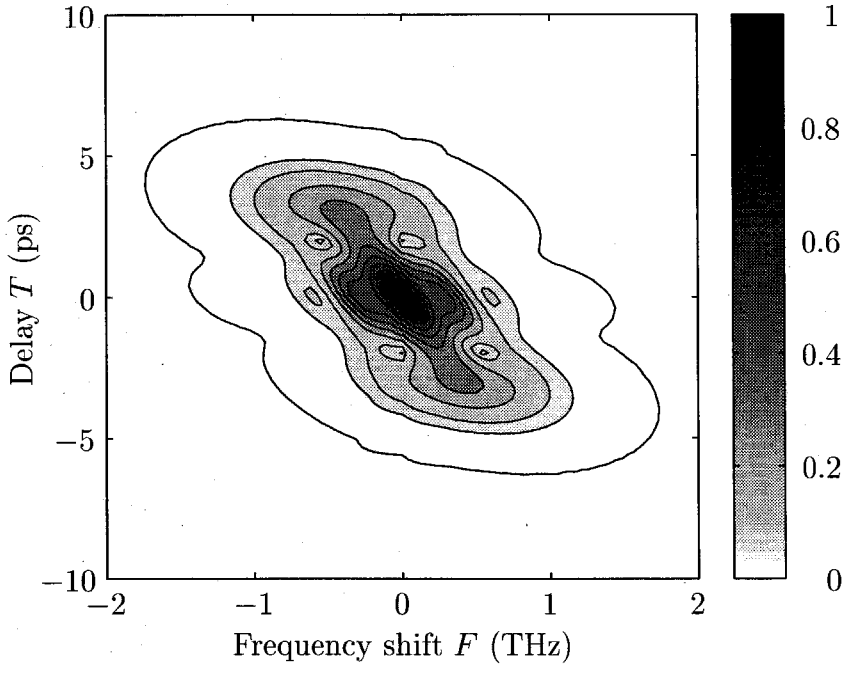


Figure 5.14: Sonogram obtained by interpolating the sonogram of Fig. 5.13 in the $F$-direction.

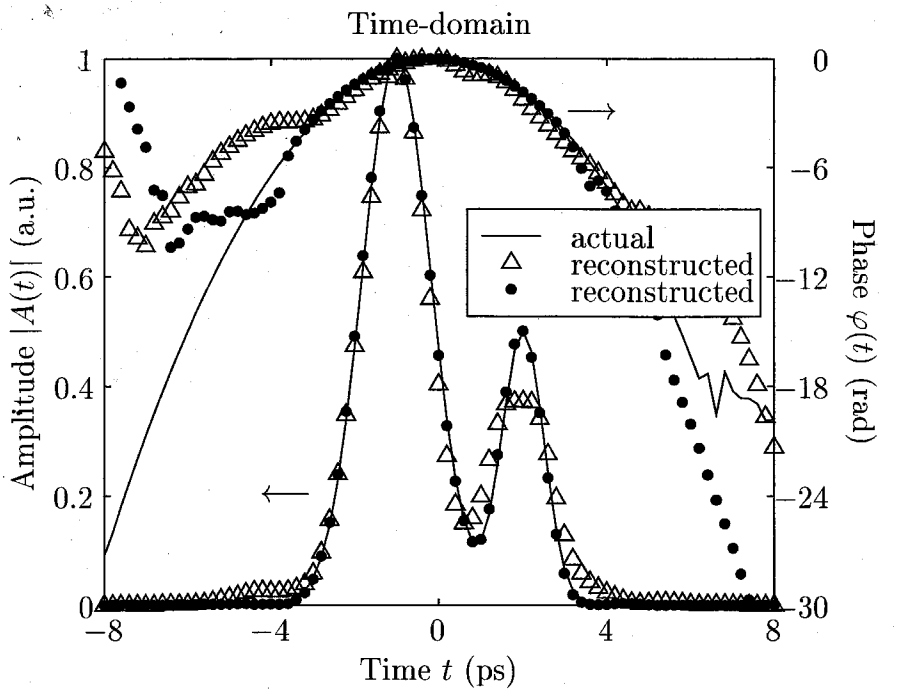


Figure 5.15: Amplitude and phase of the non-linearly chirped double pulse represented in the time-domain: actual pulse (solid line), reconstructed pulse using the sonogram of Fig. 5.13 (triangles) and Fig. 5.14 (dots).

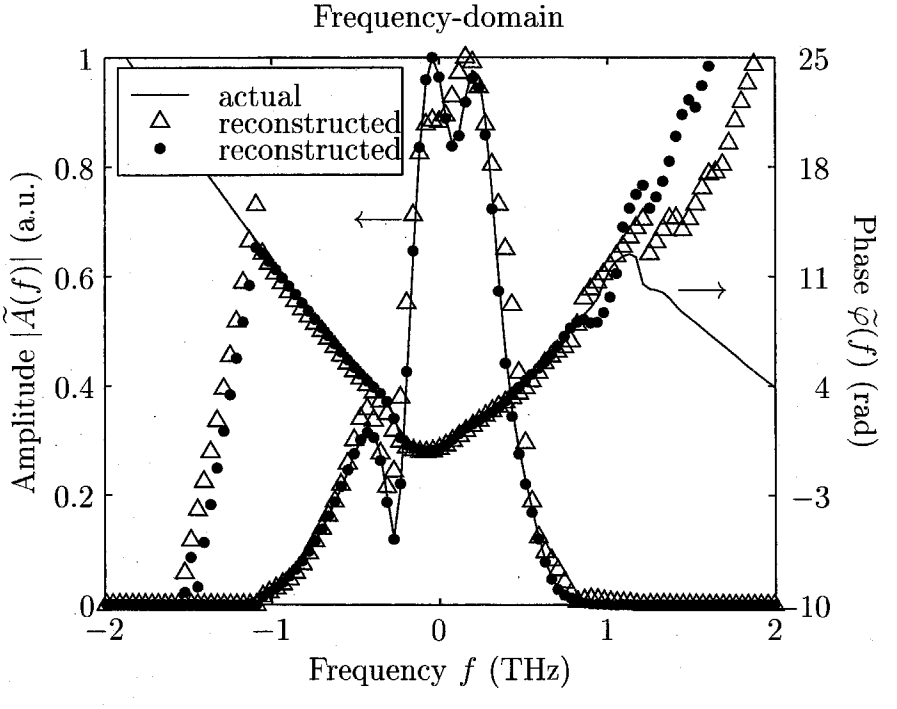


Figure 5.16: Amplitude and phase of the non-linearly chirped double pulse represented in the frequency-domain: actual pulse (solid line), reconstructed pulse using the sonogram of Fig. 5.13 (triangles) and Fig. 5.14 (dots).

It is noted that a TROG trace contains redundant information: it is made up of $N \times N$ data points while the pulse shape is only determined by $2N$ points. One might thus try and exploit the two dimensions $F$ and $T$ of the trace to try to obtain TROG data around $F = 0$: we fill in the gaps of the TROG trace of Fig. 5.13 by doing $N$ one-dimensional interpolations in the $F$-direction. The resulting interpolated TROG trace is shown in Fig. 5.14. Comparing this trace with the trace in Fig. 5.7 shows that the interpolation works very well. In order to find out how much the two traces actually differ, the error between the two traces has been computed. A maximum relative error of a few percent is found for all the points on the $N \times N$ grid.

In order to find out the effects of this interpolation on the pulse reconstruction, we have run the algorithm on the TROG trace of Fig. 5.14. Its convergence is shown in Fig. 5.10 (dotted-dash line) and the amplitude and phase of the retrieved pulse in the time and frequency-domain are shown in Fig. 5.15 and Fig. 5.16 respectively by the dots. Excellent pulse retrieval is accomplished. Convergence occurs within fifty iterations and the final error is approximately $\varepsilon_{\mathrm{TROG}} = 7 \cdot 10^{-4}$. Comparing the dash and dotted-dash line in Fig. 5.10, it is found that the algorithm convergence is approximately sped up by a factor of two. The ability of the algorithm to retrieve the correct spectral phase is not affected (see Fig. 5.16). The ability to retrieve the correct spectral intensity is however strongly improved. It is noted that an accurate time-domain representation of the pulse can be obtained by using the spectral phase retrieved by the algorithm together with the measured intensity spectrum instead of the intensity spectrum retrieved by the algorithm. As an alternative, one can also add an additional intensity spectrum constraint to the algorithm on each iteration by replacing the spectral amplitude $\widetilde{A}(f)$ with the square root of the measured intensity spectrum $\widetilde{I}(f)$, i.e.,

$$\widetilde{A}'(f) = \sqrt{\widetilde{I}(f)} \frac{\widetilde{A}^{(k)}(f)}{|\widetilde{A}^{(k)}(f)|} \tag{5.23}$$

As a final step we have further tested the algorithm for the addition of multiplicative and additive noise to the autocorrelation trace. As TROG is similar to FROG except for the fact that the roles of time and frequency are interchanged, noise reduc-

tion techniques that are available for FROG [8] can also be used for TROG. For more details on these and other noise reduction procedures, the reader is referred to [8]. In Chapter 6 we discuss issues regarding noise and noise-filtering and the application of this technique to an experimentally obtained DP-TROG trace in detail.

## 5.4 Remarks about DP-TROG and comparison with SHG-FROG

In this chapter we have introduced the TROG technique and shown its time-frequency duality with FROG. A new TROG geometry has been introduced based on dispersive propagation. It has been shown that measurements of the autocorrelation traces of dispersed versions of the pulse together with a measurement of its spectrum are sufficient to recover phase and amplitude information. One of the advantages of the DP-TROG geometry is that it is simple to realize: it makes use of a dispersive medium and an autocorrelator. This equipment is usually already present in an optics laboratory. The only restriction of the autocorrelator is that its nonlinear crystal needs to be suited to the wavelength of the pulse, i.e., it needs to be able to generate a SHG signal from the pulse. SHG crystals are usually available for most wavelengths at which pulses are generated nowadays. For a pulse with a wavelength in the optical communication band (1.5 $\mu$m), one usually uses a lithium niobate crystal. Although we use a set of fibers as the dispersive medium in our analysis, this might not be very practical in experiments as a large number of fibers is needed and their length will vary from experiment to experiment depending on the temporal width and chirp of the pulse. A grating or prism pulse stretcher/compressor is more appropriate as long as its dispersion can be adjusted below and above the value for which minimum pulse width (i.e., maximum pulse compression) occurs and as long its optical loss is acceptable. In the experiments of Chapter 6, a dual grating telescope pulse compressor/stretcher is used as the dispersive medium.

The DP-TROG geometry is a sensitive technique as it uses a second-order nonlinearity instead of a higher order one as is for example the case for THG-FROG. It will work for any low energy pulse that contains enough energy for the autocorrelation

trace to be measured. We have also shown that this technique does not require a short gate pulse as is the case with FDPM-TROG. This is in contradiction with the statement of Wong and Walmsley that a short gate pulse is a requirement for a type IV (PS-ANS) device.

The advantage of DP-TROG over SHG-FROG is two-fold. First, more sensitivity is obtained as there is no need to measure the spectrum of the SHG signal. In order to spectrally resolve the SHG-FROG signal, an additional grating would be needed which would introduce more losses in this already weak signal. Secondly, the ambiguity in the direction of time which is inherent in SHG-FROG is not present in DP-TROG (see Appendix B).

We have shown that the TROG reconstruction algorithm works extremely well even for the case of a non-linearly chirped double pulse. Although best reconstruction is accomplished if the autocorrelation traces are measured over a large dispersion range, the two-dimensional interpolation of the measured traces into the TROG trace allows for a smaller dispersion range over which measurements need to be made. Due to the fact that the SHG signal does not need to be spectrally resolved, the DP-TROG method is useful for characterizing low energy pulses in the $1.3 - 1.5$ $\mu$m wavelength range.

## References

[1] J. Chilla and O. Martinez, "Direct determination of the amplitude and the phase of femtosecond light-pulses," *Opt. Lett.*, vol. 16, no. 1, pp. 39–41, 1991.

[2] J. Chilla and O. Martinez, "Analysis of a method of phase measurement of ultrashort pulses in the frequency-domain," *IEEE J. Quantum Electron.*, vol. 27, no. 5, pp. 1228–1235, 1991.

[3] J. Chilla and O. Martinez, "Frequency-domain phase measurement of ultrashort light-pulses - effect of noise," *Opt. Commun.*, vol. 89, no. 5-6, pp. 434–440, 1992.

[4] D. Kane and R. Trebino, "Characterization of arbitrary femtosecond pulses using frequency-resolved optical gating," *IEEE J. Quantum Electron.*, vol. 29, no. 2, pp. 571–579, 1993.

[5] D. Kane and R. Trebino, "Single-shot measurement of the intensity and phase of an arbitrary ultrashort pulse by using frequency-resolved optical gating," *Opt. Lett.*, vol. 18, no. 10, pp. 823–825, 1993.

[6] K. DeLong and R. Trebino, "Improved ultrashort pulse-retrieval algorithm for frequency-resolved optical gating," *J. Opt. Soc. Amer. A*, vol. 11, no. 9, pp. 2429–2437, 1994.

[7] D. Kane, A. Taylor, R. Trebino, and K. DeLong, "Single-shot measurement of the intensity and phase of a femtosecond UV laser-pulse with frequency-resolved optical gating," *Opt. Lett.*, vol. 19, no. 14, pp. 1061–1063, 1994.

[8] D. Fittinghoff, K. DeLong, R. Trebino, and C. Ladera, "Noise sensitivity in frequency-resolved optical-gating measurements of ultrashort pulses," *J. Opt. Soc. Amer. B*, vol. 12, no. 10, pp. 1955–1967, 1995.

[9] K. DeLong, D. Fittinghoff, and R. Trebino, "Practical issues in ultrashort-laser-pulse measurement using frequency-resolved optical gating," *IEEE J. Quantum Electron.*, vol. 32, no. 7, pp. 1253–1264, 1996.

[10] V. Wong and I. Walmsley, "Analysis of ultrashort pulse-shape measurement using linear interferometers," *Opt. Lett.*, vol. 19, no. 4, pp. 287–289, 1994.

[11] V. Wong and I. Walmsley, "Linear filter analysis of methods for ultrashort-pulse-shape measurements," *J. Opt. Soc. Amer. B*, vol. 12, no. 8, pp. 1491–1499, 1995.

[12] I. Walmsley and V. Wong, "Characterization of the electric field of ultrashort optical pulses," *J. Opt. Soc. Amer. B*, vol. 13, no. 11, pp. 2453–2463, 1996.

[13] C. Iaconis, V. Wong, and I. Walmsley, "Direct interferometric techniques for characterizing ultrashort optical pulses," *IEEE J. Selec. Top. Quantum Electron.*, vol. 4, no. 2, pp. 285–294, 1998.

[14] O. Martinez, "3000 times grating compressor with positive group-velocity dispersion - application to fiber compensation in 1.3-1.6 $\mu$m region," *IEEE J. Quantum Electron.*, vol. 23, no. 1, pp. 59–64, 1987.

[15] R. Fork, O. Martinez, and J. Gordon, "Negative dispersion using pairs of prisms," *Opt. Lett.*, vol. 9, no. 5, pp. 150–152, 1984.

[16] A. Yariv, *Optical Electronics in Modern Communications.* New York: Oxford University Press, 1997.

[17] K. Sala, G. Kenney-Wallace, and G. Hall, "CW autocorrelation measurements of picosecond laser pulses," *IEEE J. Quantum Electron.*, vol. 16, no. 9, pp. 990–996, 1980.

[18] J. Fienup, "Phase retrieval algorithms - a comparison," *Appl. Opt.*, vol. 21, no. 15, pp. 2758–2769, 1982.

[19] R. Trebino and D. Kane, "Using phase retrieval to measure the intensity and phase of ultrashort pulses - frequency-resolved optical gating," *J. Opt. Soc. Amer. A*, vol. 10, no. 5, pp. 1101–1111, 1993.

[20] K. DeLong, R. Trebino, J. Hunter, and W. White, "Frequency-resolved optical gating with the use of second-harmonic generation," *J. Opt. Soc. Amer. B*, vol. 11, no. 11, pp. 2206–2215, 1994.

[21] K. DeLong, D. Fittinghoff, R. Trebino, B. Kohler, and K. Wilson, "Pulse retrieval in frequency-resolved optical gating based on the method of generalized projections," *Opt. Lett.*, vol. 19, no. 24, pp. 2152–2154, 1994.

[22] D. Kane, G. Rodriguez, A. Taylor, and T. Clement, "Simultaneous measurement of two ultrashort laser pulses from a single spectrogram in a single shot," *J. Opt. Soc. Amer. B*, vol. 14, no. 4, pp. 935–943, 1997.

[23] W. Press, S. Teukolsky, W. Vetterling, and B. Flannery, *Numerical Recipes in C*. Cambridge University Press, 1992.

# CHAPTER 6

# *Time-resolved optical gating based on dispersive propagation: experiment*

## 6.1 Introduction

In this chapter we demonstrate the use of time resolved optical gating based on dispersive propagation (DP-TROG) to characterize a semiconductor mode-locked laser emitting picosecond pulses at a wavelength of 1.5 $\mu$m. DP-TROG is a new non-interferometric method for characterizing ultra-short optical pulses in amplitude and phase without the need for a short optical gating pulse. We describe the experimental setup and in particular the dual grating telescope pulse stretcher/compressor that is used as the dispersive medium. The linear dispersion as well as higher order dispersion for this dual grating telescope are calculated. The setup is used to characterize the optical pulses emitted by a semiconductor mode-locked laser. In the experiment we measure a number of autocorrelation traces of dispersed versions of the pulse and its intensity spectrum. One can derive the sonogram or DP-TROG trace for the pulse from these measurements and we make recommendations for this procedure and for the reconstruction of the pulse properties from the sonogram. Issues of additive measurement noise and noise reduction and filtering techniques are discussed as well.

## 6.2 The dual grating telescope disperser

The DP-TROG geometry makes use of a medium which has an adjustable amount of dispersion. Although one could use a number of optical fibers with different lengths as the dispersive medium, this is not very practical. Instead we have chosen a dual grating telescope disperser (see Fig. 6.1). The incoming pulse first hits the right grating of the disperser. The grating spatially separates the pulse into its wavelength components which then pass through the telescope and hit the second grating which is placed at the same angle with respect to the telescope axis as the first grating. In order to avoid spatial displacement of the beam, a mirror has been added after the second grating of the telescope so that the pulse is reflected back into the telescope again. This both ensures that the pulse gets spatially reflected back onto itself and it also doubles the amount of dispersion added to the pulse by the disperser.

This kind of disperser has the advantage that both the amount of disperson can be adjusted by simply moving the gratings and also the sign of the dispersion can be changed, depending on whether the gratings are within the focal point of the lenses or outside. The transfer function of the disperser is given by (5.11) where $D$ is the dispersion parameter which will be calculated in the next section. The dispersion can be adjusted by changing the position of either or both of the gratings with respect to the focal point of their respective lenses. The spectrum of the pulse exiting the telescope is given by (5.16).

### *6.2.1 Linear dispersion*

We can calculate the amount of linear dispersion (quadratic phase) added to the pulse upon propagation through the telescope by examining the pathlength difference for rays of different wavelengths. A magnification of the rays hitting the left grating of the telescope in Fig. 6.1 is given in Fig. 6.2. Here $\theta_{in}$ is the angle between the incoming beam and the normal to the first grating; this angle is equal to the angle under which the rays leave the second grating. The angle $\theta_g$ is the angle between the normal to the grating and the telescope axis. The angle $\alpha$ is the angle between the

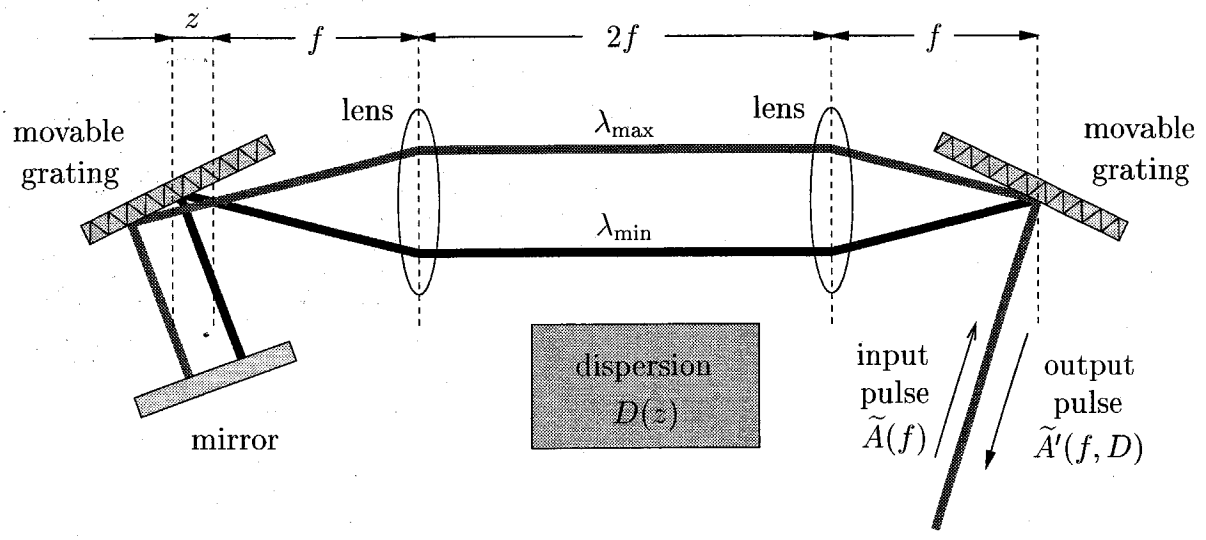


Figure 6.1: Schematic diagram of the dual grating telescope disperser.

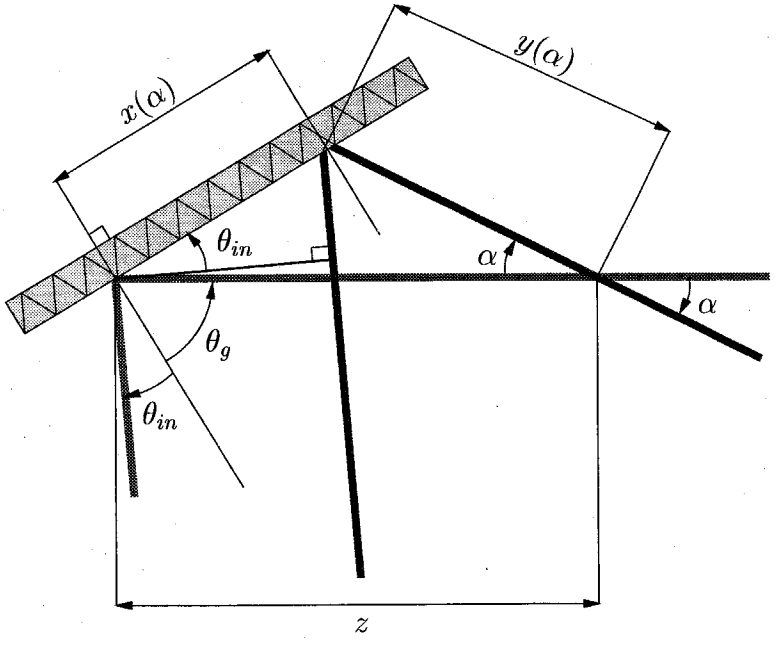


Figure 6.2: View of the pathlength difference for two rays of different wavelengths hitting the second grating of the telescope disperser.

rays leaving the first grating and the telescope axis. This angle $\alpha$ is a function of the wavelength $\lambda$ of the ray and can be calculated from the Bragg condition for the grating

$$\sin(\theta_g - \alpha) - \sin(\theta_{in}) = \frac{\lambda}{d} \equiv \frac{\omega_g}{\omega} \tag{6.1}$$

where $1/d$ is the grating line density, $\omega$ is the optical frequency of the ray and $\omega_g = 2\pi c/d$. Here $c$ is the speed of light. The pathlength as a function of wavelength, or the angle $\alpha$, is given by

$$L(\alpha) = y(\alpha) + x(\alpha)\sin(\theta_{in}) \tag{6.2}$$

where $x(\alpha)$ and $y(\alpha)$ are indicated in Fig. 6.2. We can calculate an effective dispersion parameter $\beta_2$ for the dual grating telescope analogously to the $\beta_2$ parameter for an optical fiber [1] by considering the group delay of the disperser as a function of wavelength or equivalently as a function of the angle $\alpha$. The group delay is given by

$$\tau_g = 2\frac{L(\alpha)}{zc} \tag{6.3}$$

The factor 2 arises from the fact that the pulse passes through the telescope twice. The $\beta_2$ parameter for the disperser is defined as the derivative of the group delay with respect to frequency and is given by

$$\beta_2 \equiv \frac{\mathrm{d}\tau_g}{\mathrm{d}\omega} = \frac{2}{zc}\frac{\mathrm{d}L(\alpha)}{\mathrm{d}\alpha}\frac{\mathrm{d}\alpha}{\mathrm{d}\omega} \tag{6.4}$$

Applying straightforward trigonometry to Fig. 6.2 gives the pathlength

$$L(\alpha) = z\left(\frac{\cos(\theta_g) + \sin(\alpha)\sin(\theta_{in})}{\cos(\theta_g - \alpha)}\right) \tag{6.5}$$

and from (6.1) we can calculate

$$\frac{\mathrm{d}\alpha}{\mathrm{d}\omega} = \frac{\omega_g}{\omega^2}\frac{1}{\cos(\theta_g - \alpha)} \tag{6.6}$$

| Symbol | Units | *Example 1* | *Example 2* |
|---|---|---|---|
| $\theta_{in}$ | – | $-5.4°$ | $-17.4°$ |
| $\theta_g$ | – | $56.0°$ | $78.0°$ |
| $\lambda$ | nm | 1539 | 1539 |
| $1/d$ | lines/mm | 600 | 830 |
| $\beta_2$ | $ps^2/m$ | $-15$ | $-205$ |
| $\beta_3$ | $ps^3/m$ | 0.13 | 15 |

Table 6.1: Typical examples for the linear and non-linear dispersion parameters $\beta_2$ and $\beta_3$ of a telescope grating disperser.

Substitution of (6.5), (6.6) together with (6.1) in (6.4) gives the following value for the effective dispersion constant of the dual grating disperser

$$\begin{aligned}\beta_2 &= -\frac{2}{c}\frac{\omega_g^2}{\omega^3}\frac{\cos(\theta_g)}{\cos^2(\theta_g-\alpha)} \\ &= \frac{-\lambda^3}{\pi c^2 d^2}\frac{\cos(\theta_g)}{\cos^3(\theta_g-\alpha)} \\ &\approx \frac{-\lambda^3}{\pi c^2 d^2 \cos^2(\theta_g)}\end{aligned} \tag{6.7}$$

where in the last approximation we have assumed that the angular dispersion of the gratings is limited to a few degrees.

In Table 6.1 we have calculated the linear dispersion coefficient for two typical grating examples. In order to increase the effective dispersion parameter $\beta_2$ one needs to place the gratings at a large angle with respect to the telescope axis and one needs to maximize the number of lines per mm on the grating. For comparison, the dispersion parameter for a regular single-mode fiber (SMF-28) is $\beta_2 = -22.6$ $ps^2/km$.

### 6.2.2 *Higher order dispersion*

In order to find out what the effect is of higher order dispersion introduced by the telescope disperser, we calculate the nonlinear dispersion similarly as Martinez has done for a standard dual grating disperser in [2]. We define the first next higher order

dispersion parameter $\beta_3$ as

$$\beta_3 \equiv \frac{\mathrm{d}\beta_2}{\mathrm{d}\omega} = \frac{\mathrm{d}}{\mathrm{d}\omega}\left(\frac{\mathrm{d}\tau_g}{\mathrm{d}\omega}\right) \tag{6.8}$$

Using (6.6) and (6.7) we find

$$\begin{aligned}\beta_3 &= \frac{2}{c}\frac{\omega_g^2}{\omega^3}\frac{\cos(\theta_g)}{\cos^2(\theta_g-\alpha)}\frac{3}{\omega}\left\{1+\frac{\omega_g}{\omega}\frac{\sin(\theta_g-\alpha)}{\cos^2(\theta_g-\alpha)}\right\} \\ &= -\frac{3}{\omega}\left\{1+\frac{\omega_g}{\omega}\frac{\sin(\theta_g-\alpha)}{\cos^2(\theta_g-\alpha)}\right\}\beta_2\end{aligned} \tag{6.9}$$

For the examples shown in Table 6.1, we have calculated the magnitude of this nonlinear dispersion term. Comparing the values in Table 6.1 we find that the nonlinear dispersion $\beta_3$ is around 1-10% of the linear disperser $\beta_2$ depending on the angle of the gratings. From simulation results we find that this amount of nonlinear dispersion does not affect the ability of the pulse reconstruction algorithm to reconstruct the pulse correctly. It is noted that a TROG trace contains redundant information. The trace consists of $N \times N$ points while the pulse shape is determined by only $2N$ points ($N$ for the amplitude and $N$ for the phase). The pulse reconstruction algorithm is therefore very stable against not only measurement noise but also discrepancies between the dispersion values used and the ones actually present in the measurement setup. The algorithm uses the data redundancy and is still able to retrieve the correct amplitude and phase as long as these deviations are within a reasonable range (typically up to 10-15%). More important for the measurement is the dispersion range over which measurements are made as this determines how detailed the TROG trace is and how much data redundancy there is. We finally want to remark that if the non-linear dispersion of the telescope disperser becomes too large compared to the linear term, it is also possible to adjust the amount of the nonlinear terms $\beta_3$ and $\beta_4 = \mathrm{d}\beta_3/\,\mathrm{d}\omega$ by changing the azimuth and altitude angles of the gratings. For more details on how this is done for the standard dual grating disperser, the reader is referred to [2].

## 6.3 Experimental setup and measurement results

This section describes the experimental demonstration of the DP-TROG technique to characterize a pulse train emitted from a 2 mm long two-section mode-locked semiconductor laser at a wavelength of 1.5 $\mu$m. The absorber section of the laser is 100 $\mu$m long and is grounded while the gain section is pumped at a current of 170 mA. The pulses are amplified by an erbium doped fiber amplifier (EDFA) after which they enter the measurement setup shown in Fig. 6.3. The pulse to be characterized, with slowly varying complex envelope $A(t)$, first enters a dual grating telescope disperser [3]. The disperser adds a frequency dependent phase to the Fourier transform of the pulse which is quadratic in frequency. The Fourier transform of the pulse leaving the disperser is given by (5.16)

$$\widetilde{A}'(f, D) = \widetilde{A}(f) \exp(j\pi f^2 D) \tag{6.10}$$

where $D(z) = -2\pi\beta_2 z$ is the amount of dispersion added to the pulse which can be varied by adjusting the distance $z$ between the grating and the focal point of the telescope. As calculated in the previous section, the effective dispersion parameter $\beta_2$ of the dual grating telescope is given by (6.7)

$$\beta_2 \approx \frac{-\lambda^3}{\pi c^2 d^2 \cos^2 \theta_g} = 267 \ \frac{\text{ps}^2}{\text{m}} \tag{6.11}$$

where the following experimental values are used: $\lambda = 1539$ nm is the center wavelength of the pulse, $c$ is the speed of light in vacuum, $1/d = 830$ mm$^{-1}$ is the grating line density and $\theta_g = 79.5°$ is the angle between the normal to the grating and the telescope axis. The total insertion loss of the disperser is approximately 10 dB.

The pulse $A'(t)$ leaving the disperser is a compressed/stretched version of the input pulse $A(t)$ depending on the amount of dispersion $D$ added. The pulse is dropped from the incoming fiber with a circulator, and this pulse next enters a background-free autocorrelator consisting of a $LiNbO_3$ SHG crystal generating an optical second harmonic field that is proportional to $A'(t, D)A'(t - T, D)$. The corresponding inten-

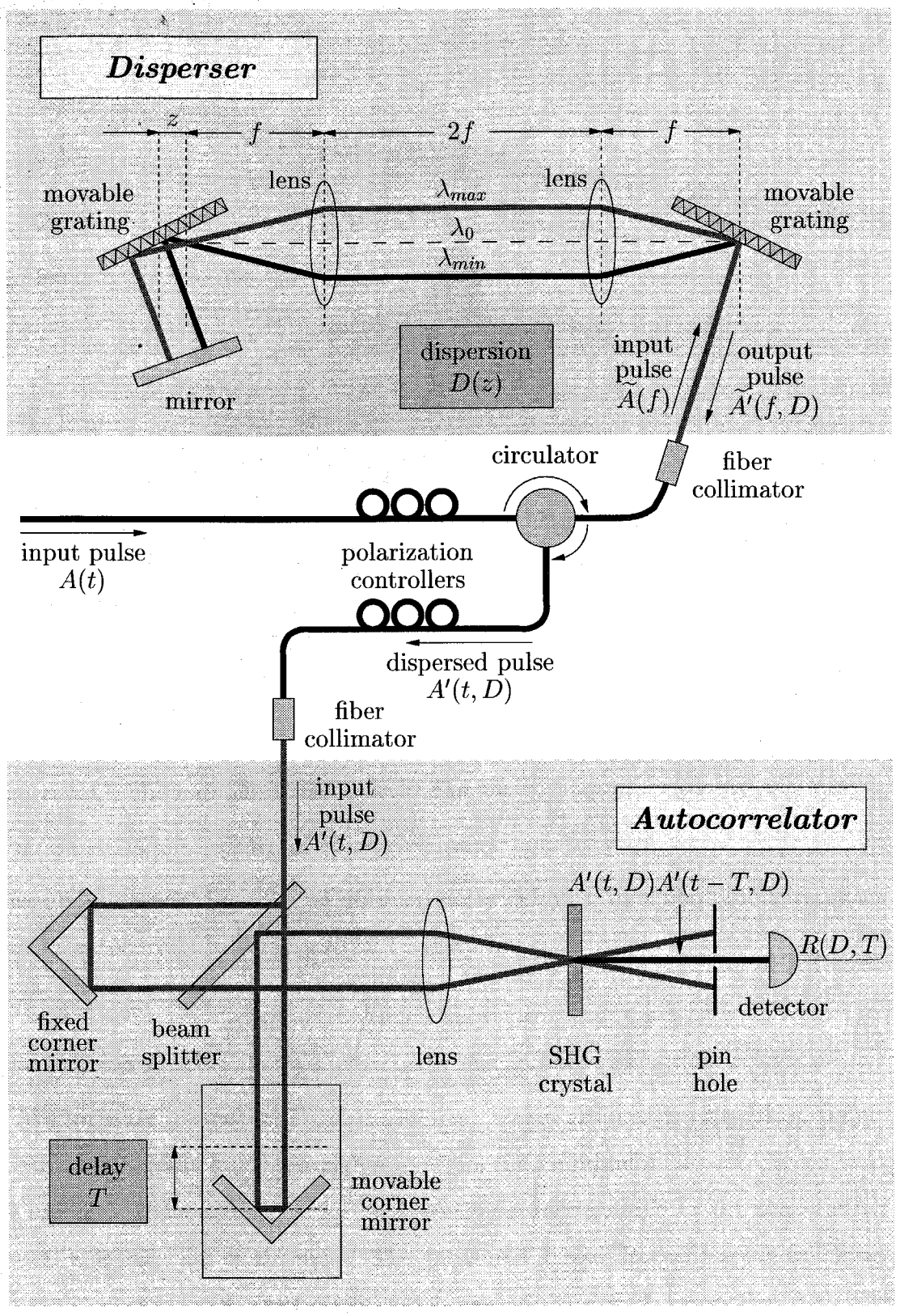


Figure 6.3: DP-TROG measurement setup consisting of a dual grating disperser and a background-free autocorrelator.

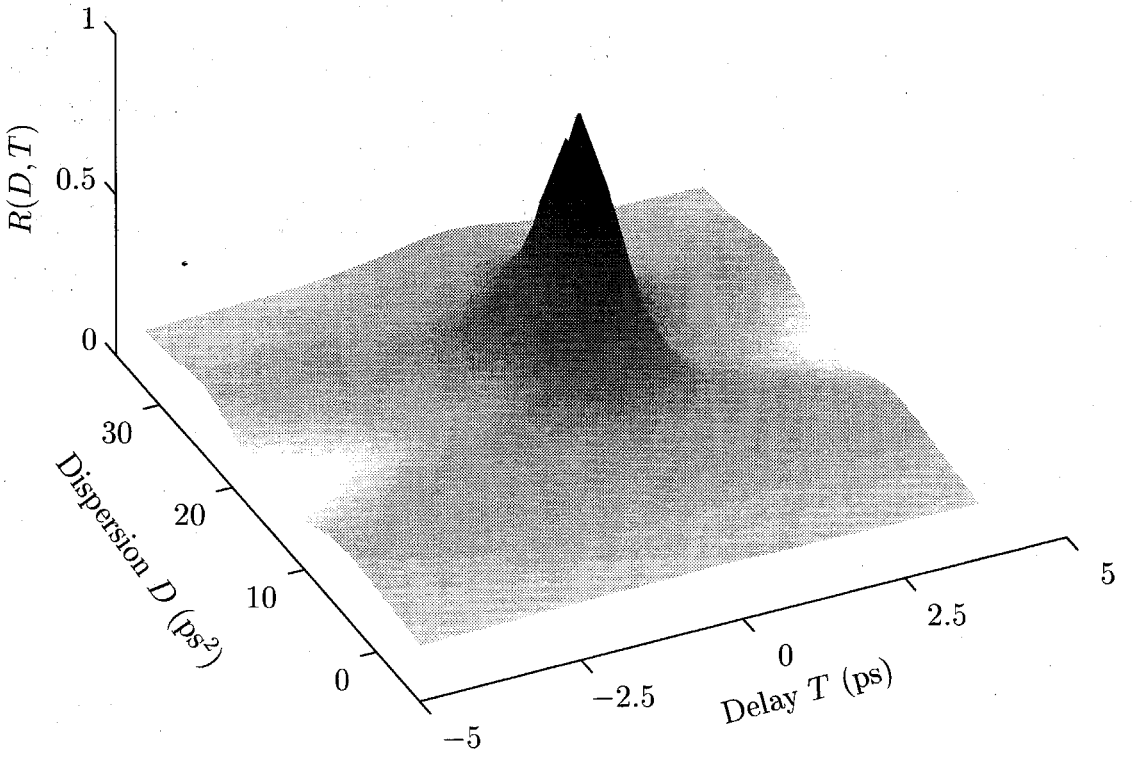


Figure 6.4: Three-dimensional view of the set of measured autocorrelation traces $R(D,T)$.

sities are integrated for different autocorrelator delays $T$ by a photodiode resulting in a set of autocorrelation traces $R(D,T)$ given by

$$R(D,T) = \int |A'(t,D)|^2 |A'(t-T,D)|^2 \, \mathrm{d}t \tag{6.12}$$

We measure a number of autocorrelation traces around the dispersion point $D_0$ for which maximum pulse compression occurs (i.e., minimum autocorrelation width). For each trace the distance $z$ for each grating is incremented by 0.1 mm leading to a total step size $\Delta z = 0.2$ mm. The measured traces $R(D,T)$ are normalized to the same energy and a three-dimensional view of them is shown in Fig. 6.4. A two-dimensional top view of the autocorrelation trace of Fig. 6.4 is shown in Fig. 6.5. In

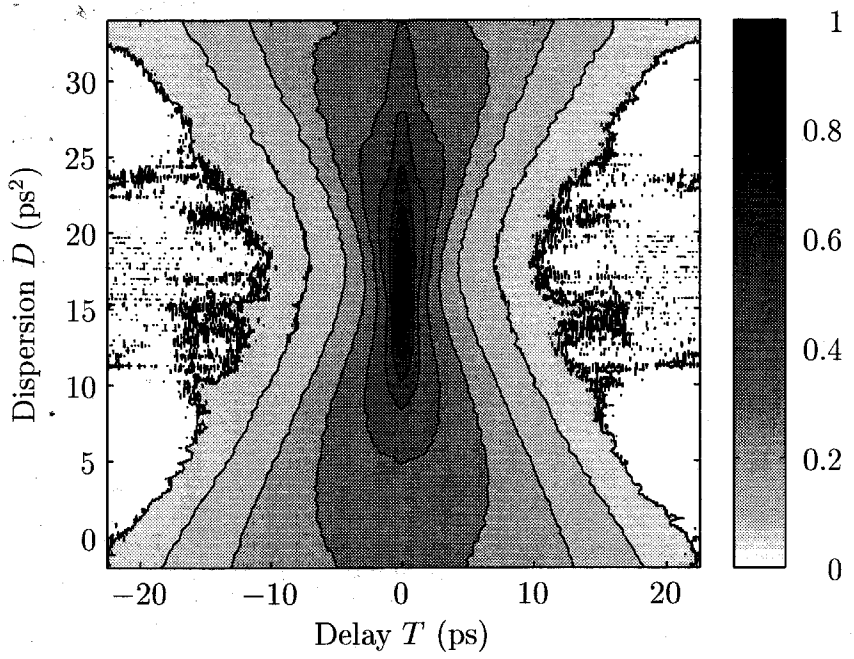


Figure 6.5: Two-dimensional view of the set of measured autocorrelation traces $\sqrt{R(D,T)}$.

order to enhance the low intensity features we have plotted its square root again. As can easily be seen from Fig. 6.5, maximum pulse compression occurs at a value of $D_0 \approx 16$ ps$^2$. In order to make the measured data accessible to our reconstruction algorithm, the measured autocorrelation trace $R(D,T)$ of Fig. 6.5 is next mapped onto an $N \times N$ grid with $N = 128$ and with dispersion step $\Delta D = 0.3$ ps$^2$ and time step $\Delta T = 0.36$ ps. The frequency step is again given by (4.18). A two-dimensional top view of the measured traces $R(D',T)$ is shown in Fig. 6.6. The dispersion range $D'$ for the *compressed* pulse around its maximum compression point $D_0$ is given by $D' = D - D_0$. When the pulse reconstruction algorithm is run on the trace $R(D',T)$, the algorithm will return with the amplitude and phase of the *compressed* pulse. The original (uncompressed) pulse can be calculated from the reconstruction results for the compressed pulse by adding the appropriate amount of dispersion $D_0$ using (6.10)

In addition to the measurement of the autocorrelation trace, the intensity spectrum of the pulse is also measured. Its result is shown in Fig. 6.7.

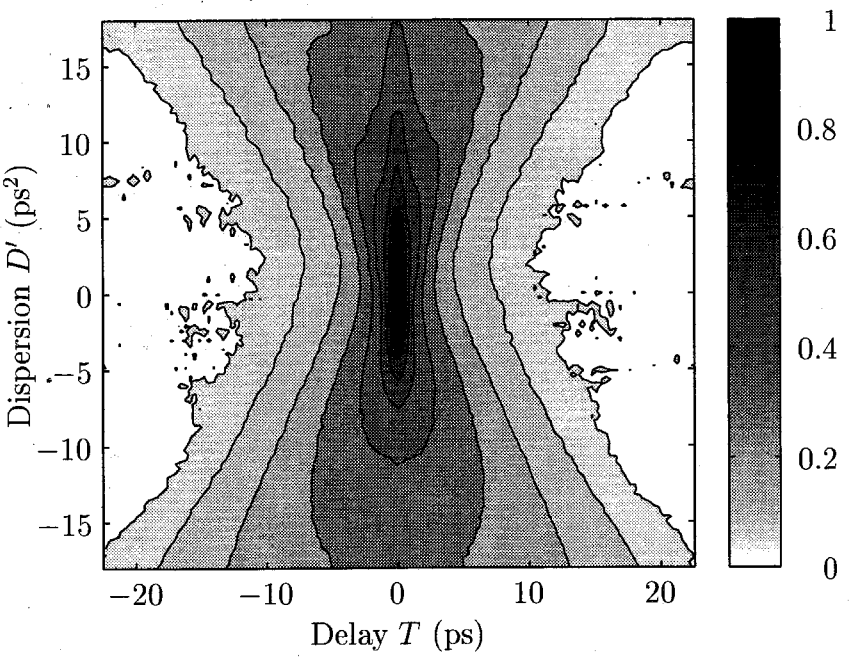


Figure 6.6: Two-dimensional view of the set of measured autocorrelation traces $\sqrt{R(D',T)}$ after mapping onto a $N \times N$ grid with $N = 128$ and with $\Delta D = 0.3$ ps$^2$, $\Delta T = 0.36$ ps and $D_0 = 16$ ps$^2$.

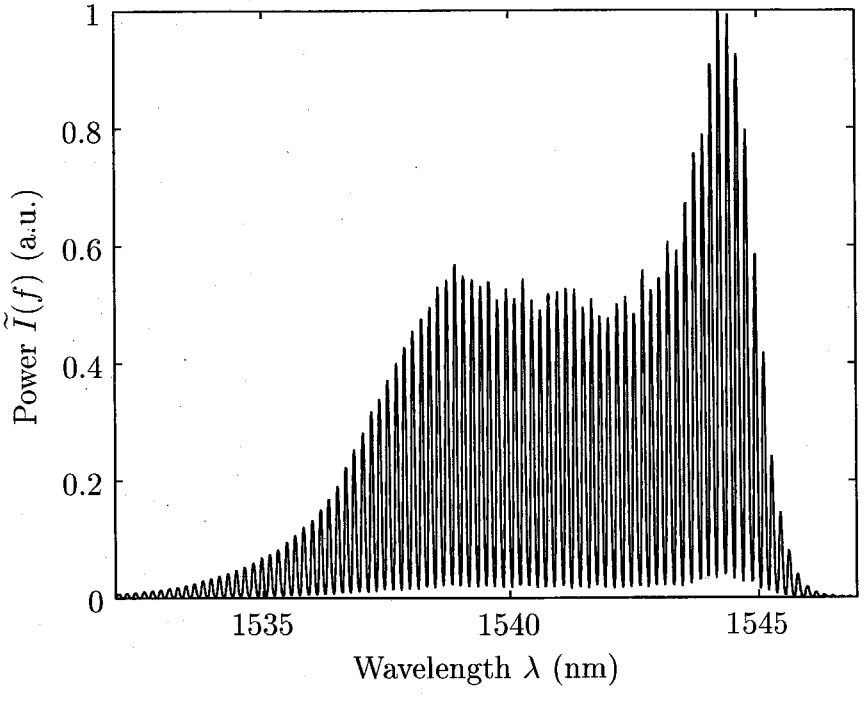


Figure 6.7: Measured intensity spectrum $\widetilde{I}(f)$ of the pulse.

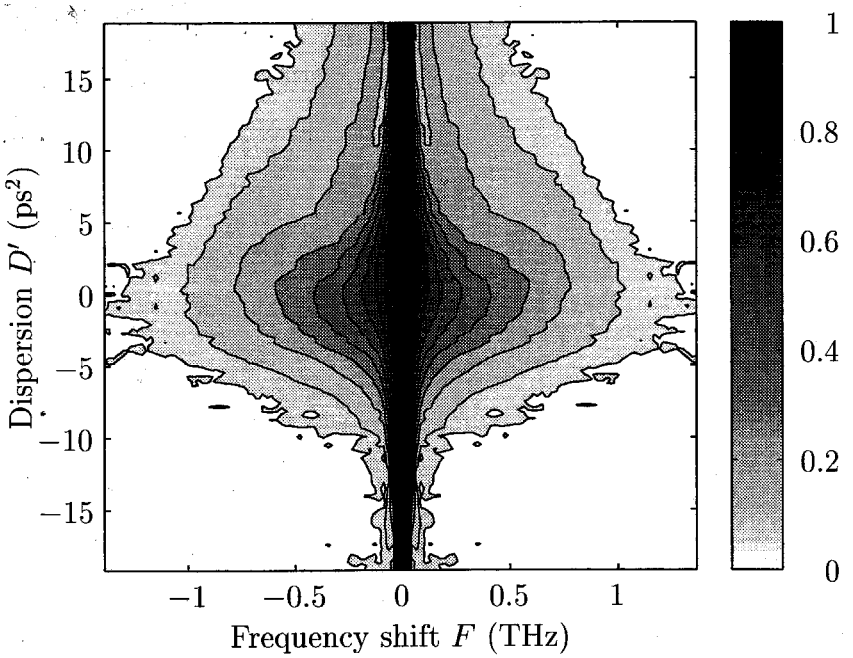


Figure 6.8: Autocorrelation spectrum $\sqrt{\widetilde{R}(D', F)}$ obtained by Fourier transformation of the autocorrelation trace of Fig. 6.6 with respect to $T$.

## 6.4 Experimental DP-TROG pulse reconstruction

We now follow the pulse reconstruction procedure for the *compressed* pulse as described in Chapter 5. We first calculate $\widetilde{R}(D', F)$, the Fourier transform of $R(D', T)$ with respect to $T$. The result is shown in Fig. 6.8. In order to enhance the noise features in this trace we have plotted its square root again. We next transform this trace into the DP-TROG trace or sonogram of the pulse

$$\begin{aligned} I_{\text{DP-TROG}}(T, F) &= \left| \int \widetilde{A}(f)\widetilde{A}^*(f - F) \exp(j2\pi fT)\, \mathrm{d}f \right|^2 \\ &= \widetilde{R}(T/F, F) \end{aligned} \tag{6.13}$$

by evaluating the trace $\widetilde{R}(D', F)$ at points $(T_i/F_j, F_j)$. The trace with $F = 0$ can not be evaluated in this way but is given by

$$I_{\text{DP-TROG}}(T, 0) = \left| \int \widetilde{I}(f) \exp(j2\pi fT)\, \mathrm{d}f \right|^2 \tag{6.14}$$

and is constructed from the measured intensity spectrum $\widetilde{I}(f)$ of the pulse by inverse Fourier transforming it and taking the norm squared. The result is shown in Fig. 6.9 and the resulting DP-TROG trace is shown in Fig. 6.10.

In order to speed up and improve algorithm convergence, we interpolate the resulting trace of Fig. 6.10 in the $F$-direction as described in Chapter 5. The result is shown in Fig. 6.11. We next apply a noise reduction technique to the DP-TROG trace of Fig. 6.11 to limit the influence of additive noise during the pulse reconstruction. Several techniques for noise reduction have been discussed previously [4]. We use a median threshold filtering technique. In determining whether to keep the value of a pixel in the trace or set it to zero, we determine the average pixel value over a square of size $2p+1$ around the pixel of interest. If this average pixel value is smaller than a certain threshold $s$, we set the current pixel to zero. Our noise filtering technique uses the values $p = 2$ and $s = 1.5 \cdot 10^{-3}$.

The resulting filtered DP-TROG trace is shown in Fig. 6.12. This trace is next used as input to the pulse reconstruction algorithm described in Section 5.3.2. The algorithm is started with an initial random guess in the frequency-domain for the amplitude uniformly distributed on $[0, 1]$ and an initial random guess for the phase in the frequency-domain uniformly distributed on $[-\pi, \pi]$. During the pulse reconstruction process we monitor the following three errors:

$$\varepsilon_{I(T,F)} = \sigma\left(I^{meas}_{\mathrm{TROG}}(T_i, F_j), \alpha^{(k)}_I I^{(k)}_{\mathrm{TROG}}(T_i, F_j)\right) \tag{6.15a}$$

$$\varepsilon_{R(D',T)} = \sigma\left(R^{meas}(D'_i, T_j), \alpha^{(k)}_R R^{(k)}_{\mathrm{FROG}}(D'_i, T_j)\right) \tag{6.15b}$$

$$\varepsilon_{\widetilde{R}(D',F)} = \sigma\left(\widetilde{R}^{meas}(D'_i, F_j), \alpha^{(k)}_{\widetilde{R}} \widetilde{R}^{(k)}_{\mathrm{TROG}}(D'_i, F_j)\right) \tag{6.15c}$$

The evolution of each of these errors is shown in Fig. 6.13. The algorithm converges after about 60 iterations with an error in $I(T, F)$ of approximately $\varepsilon_{I(T,F)} = 2.5 \cdot 10^{-3}$. For comparison of the traces $I(T, F)$, $R(D', T)$ and $\widetilde{R}(D', F)$ with the measured ones in Fig. 6.6, Fig. 6.8 and Fig. 6.10, we have plotted them in Fig. 6.14–Fig. 6.16. The very good agreement between all of the traces is noticed.

The amplitude and phase of the retrieved compressed pulse in the time and

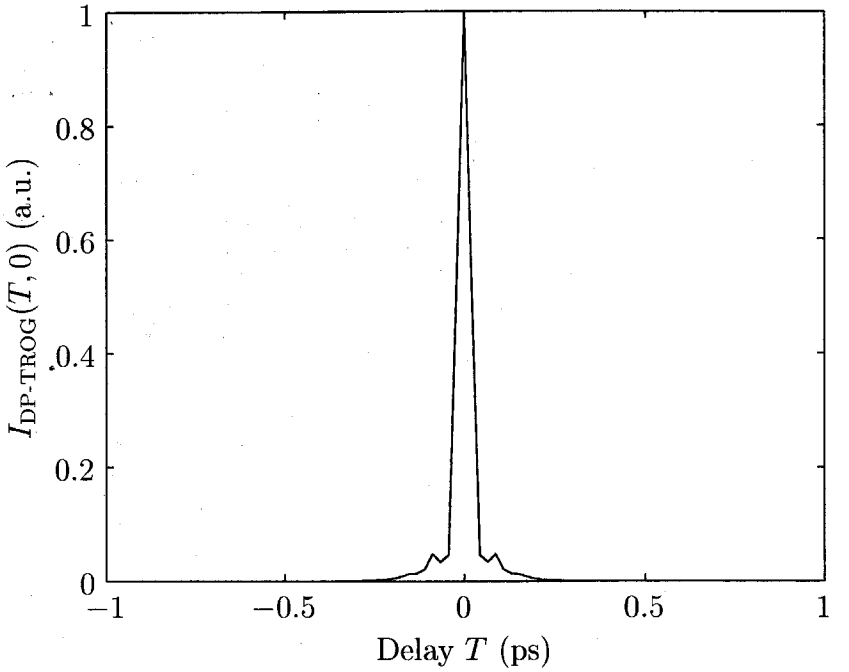


Figure 6.9: Sonogram $\sqrt{I_{\text{DP-TROG}}(T,0)}$ calculated from the envelope of the measured spectrum of Fig. 6.7 according to (6.14).

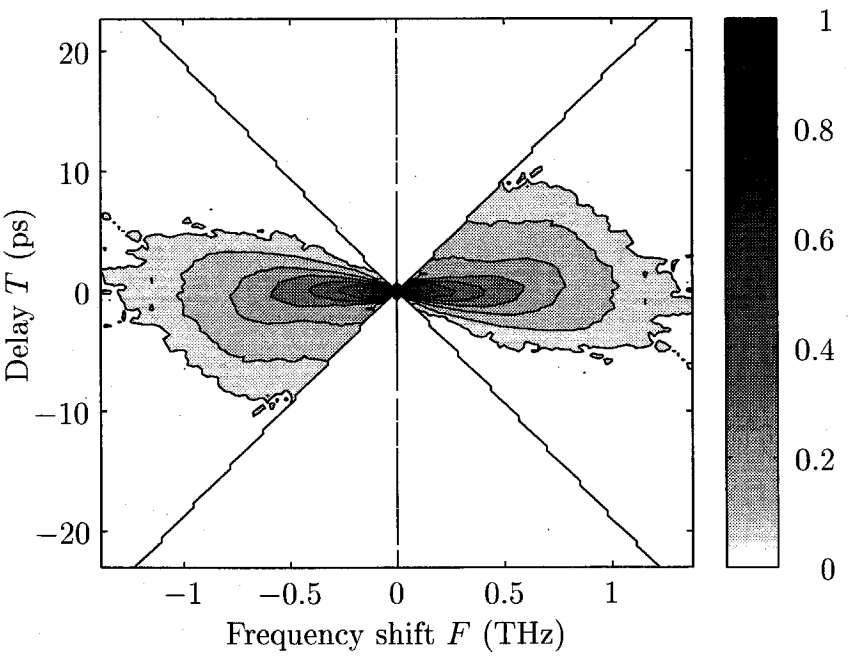


Figure 6.10: Sonogram $\sqrt{I_{\text{DP-TROG}}(T,F)}$ for the pulse reconstructed from $\widetilde{R}(D',F)$ shown in Fig. 6.8 according to (6.13).

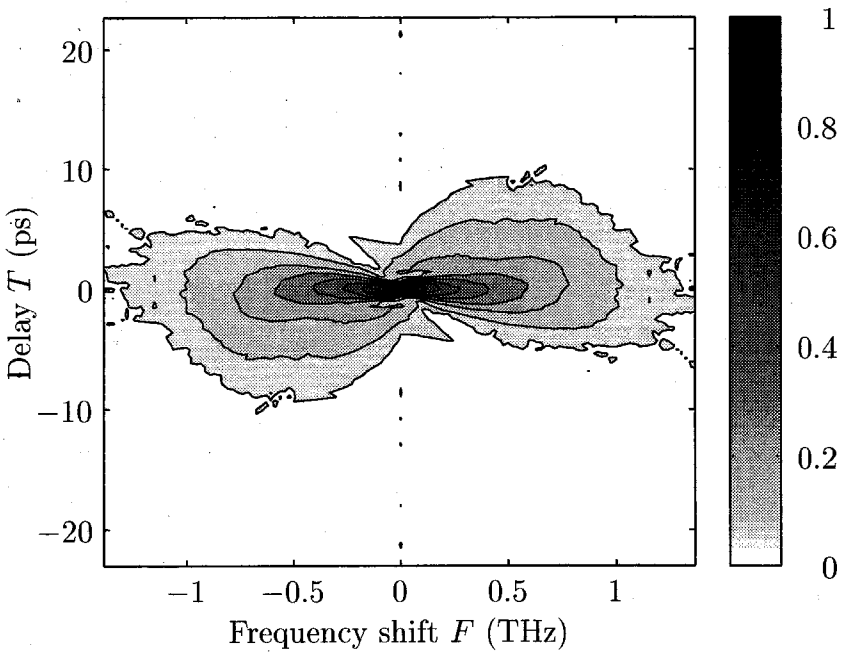


Figure 6.11: Sonogram $\sqrt{I_{\text{DP-TROG}}(T,F)}$ for the pulse after interpolation of the trace of Fig. 6.10 in the $F$-direction.

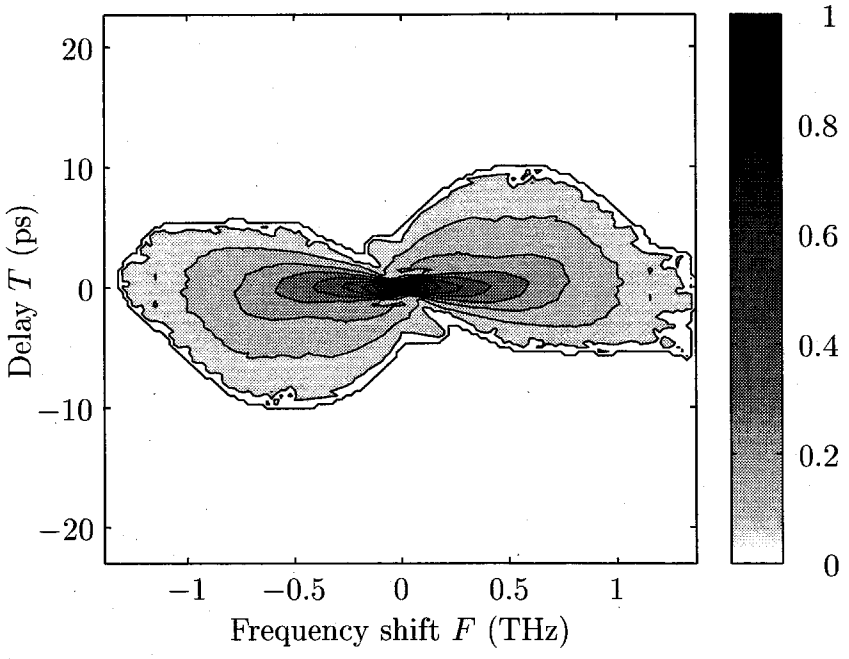


Figure 6.12: Sonogram $\sqrt{I_{\text{DP-TROG}}(T,F)}$ for the pulse after noise filtering of the trace of Fig. 6.11 with a median filtering technique with filtering parameters $p = 2$ and $s = 1.5 \cdot 10^{-3}$.

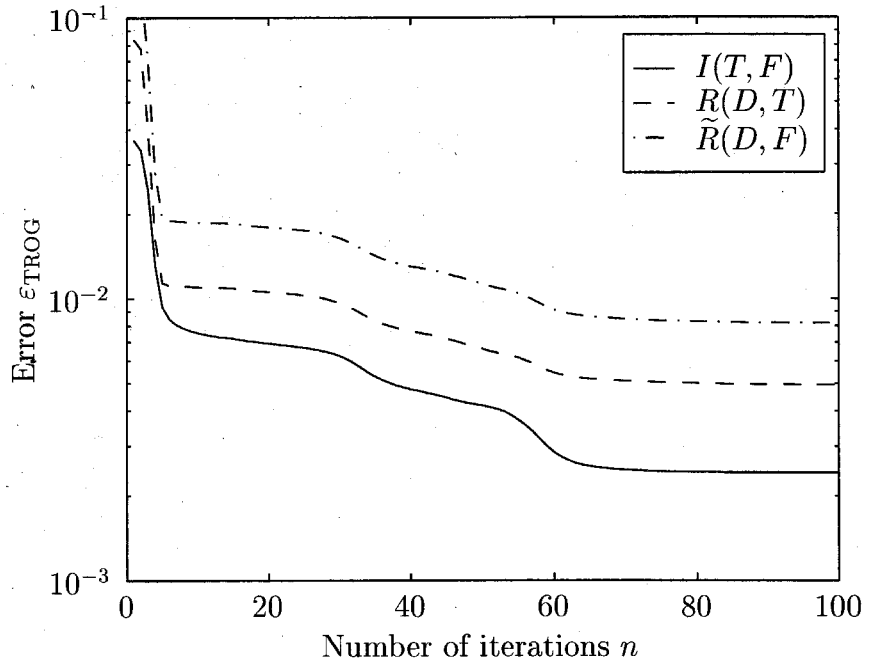


Figure 6.13: Evolution of the different error measures defined according to (6.15).

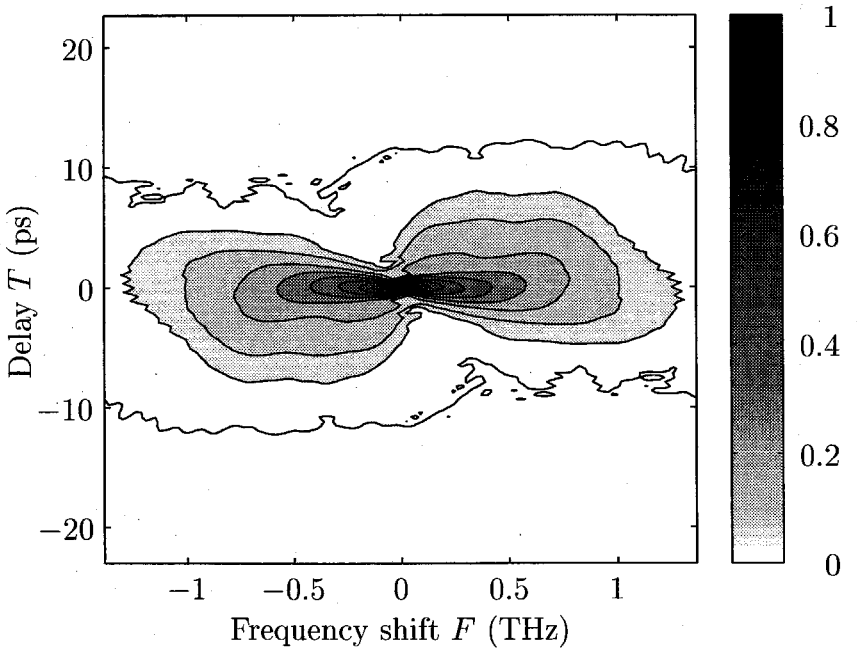


Figure 6.14: Sonogram $\sqrt{I_{\text{DP-TROG}}(T,F)}$ for the pulse returned by the pulse reconstruction algorithm.

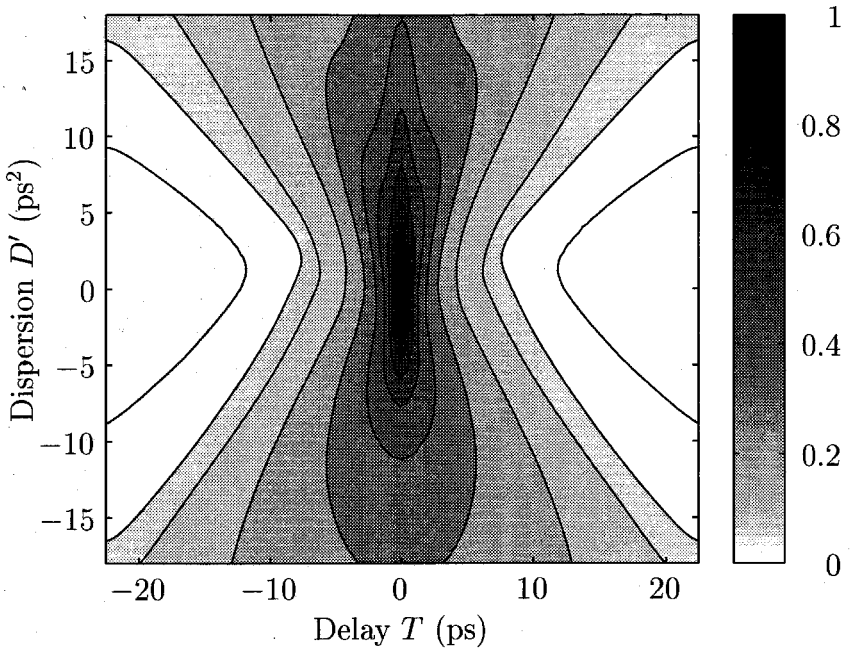


Figure 6.15: Autocorrelation trace $\sqrt{R(D,T)}$ for the pulse returned by the pulse reconstruction algorithm.

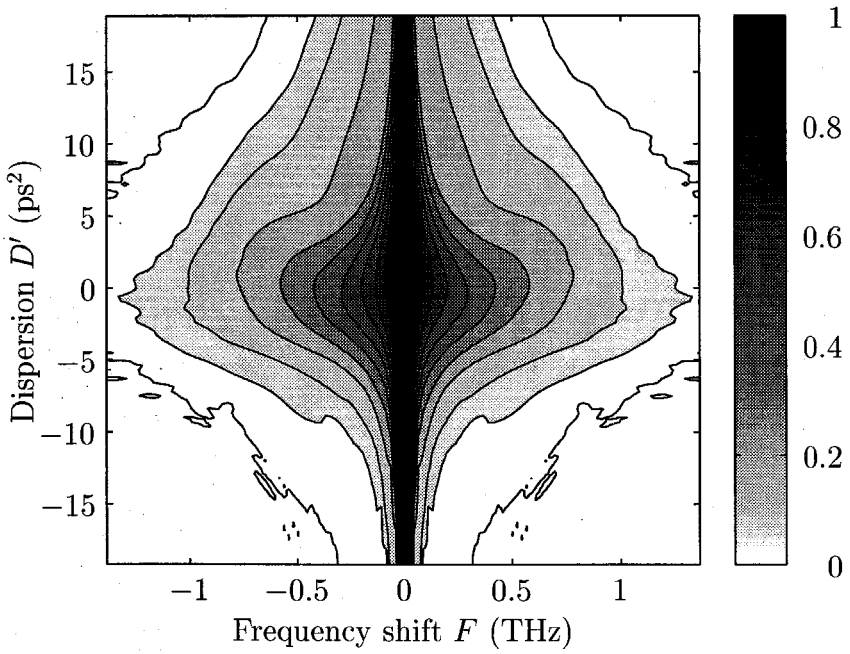


Figure 6.16: Autocorrelation spectrum $\sqrt{\widetilde{R}(D,F)}$ for the pulse returned by the pulse reconstruction algorithm.

frequency-domain are shown in Fig. 6.17 and Fig. 6.18 respectively (dots). The amplitude and phase profile of the original uncompressed pulse can be calculated from the retrieved compressed pulse by adding the amount of dispersion $D_0 \approx 16$ ps$^2$ needed to get to the maximum compression point using the inverse of (6.10). Its result can also been seen in Fig. 6.17 and Fig. 6.18 and is indicated with the dots. We have also plotted the measured spectrum $\sqrt{\widetilde{I}(f)}$ in Fig. 6.18. Agreement of the retrieved spectrum with the measured one is very good. From Fig. 6.18 it can be clearly seen that the original uncompressed pulse contains a non-linear chirp. The linear part of the chirp can be compensated by adding an amount of dispersion $D_0$. The resulting compressed pulse has a residual cubic spectral phase dependence. Upon transformation to the time-domain this cubic phase causes ringing (phase jumps of $\pi$) on the leading edge of the pulse (see Fig. 6.17). This ringing behavior on the leading edge of a pulse has also been observed in SHG-FROG measurements [5]. The full width half maximum (FWHM) of the main peak in the compressed pulse is approximately $\tau_p = 1.3$ ps.

The sonogram of the original uncompressed pulse can be calculated as well. Its result is shown in Fig. 6.19. From the orientation of the trace in Fig. 6.19 it can be easily seen that the original uncompressed pulse contains an almost linear up-chirp. The amount of linear chirp can be eastimated from the slope of the trace with respect to the $F = 0$ axis and is around 62 GHz/ps which is in agreement with the observed value $D_0 \approx 16$ ps$^2$ that is needed to compress the pulse to its minimum width. It is finally noted that the aliasing at the top left and bottom right corner of the sonogram occurs as the number of points $N = 128$ is insufficient to contain the uncompressed pulse which has a FWHM of $\tau_p^{ucp} = 19$ ps.

We finally would like to add a few remarks. As described in Chapter 5 interpolation of the TROG trace is not necessary for correct spectral *phase* retrieval. This is also true for our measurements. The spectral phase of the pulse is reconstructed correctly even if we omit the interpolation of the DP-TROG trace. Without the interpolation there is a larger error between the retrieved spectral amplitude and the measured one. This is however of no concern as the exact spectral amplitude is avail-

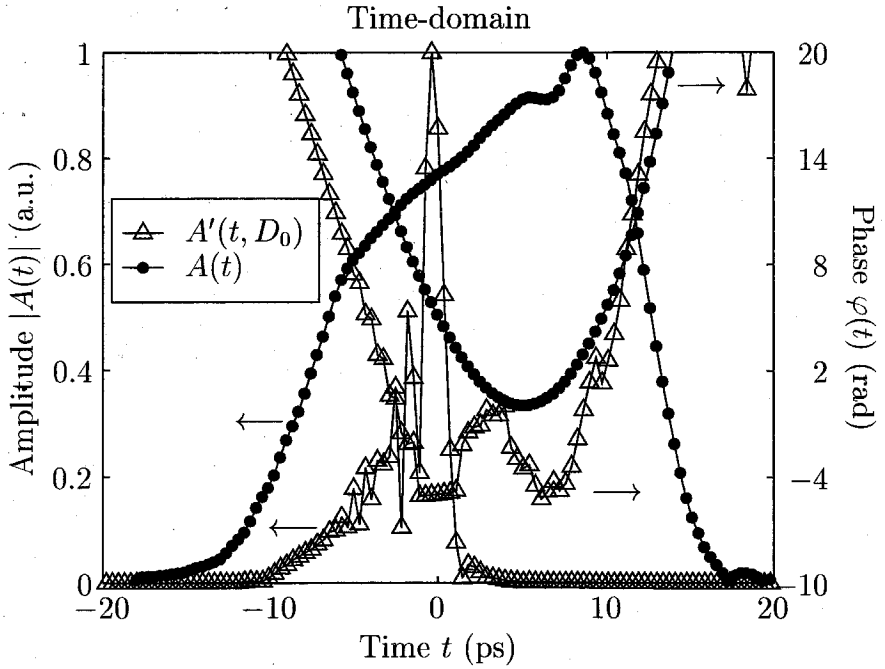


Figure 6.17: Amplitude and phase represented in the time-domain: compressed pulse $A'(t, D_0)$ (triangles) and original uncompressed pulse $A(t)$ (dots).

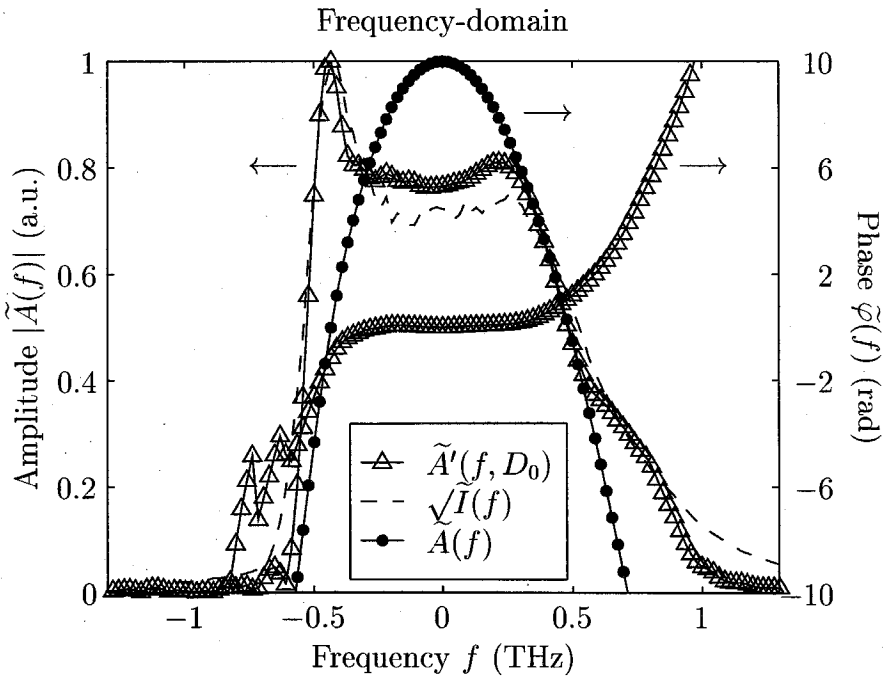


Figure 6.18: Amplitude and phase represented in the frequency-domain: compressed pulse $\widetilde{A}'(f, D_0)$ (triangles) and original uncompressed pulse $\widetilde{A}(f)$ (dots). Also shown is the measured intensity spectrum of the pulse $\sqrt{\widetilde{I}(f)}$ (dashed line).

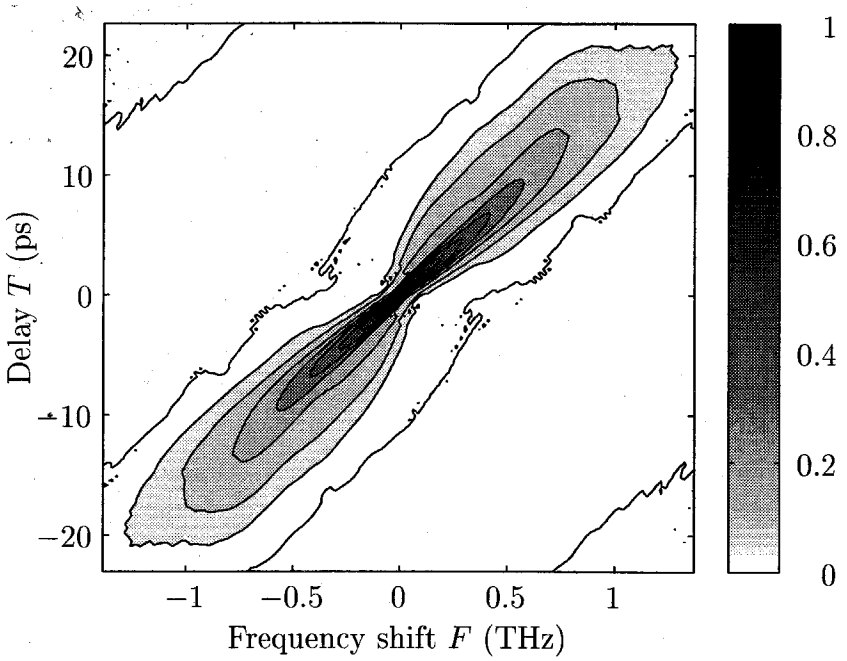


Figure 6.19: Sonogram $\sqrt{I_{\text{DP-TROG}}(T,F)}$ for the original uncompressed pulse calculated by the pulse reconstruction algorithm.

able from the measurement, and an accurate time-domain representation of the pulse can be obtained by using the spectral phase retrieved by the algorithm together with the measured spectral amplitude.

## References

[1] A. Yariv, *Optical Electronics in Modern Communications.* New York: Oxford University Press, 1997.

[2] C. Inchauspe and O. Martinez, "Quartic phase compensation with a standard grating compressor," *Opt. Lett.*, vol. 22, no. 15, pp. 1186–1188, 1997.

[3] O. Martineż, "3000 times grating compressor with positive group-velocity dispersion - application to fiber compensation in 1.3-1.6 $\mu$m region," *IEEE J. Quantum Electron.*, vol. 23, no. 1, pp. 59–64, 1987.

[4] D. Fittinghoff, K. DeLong, R. Trebino, and C. Ladera, "Noise sensitivity in frequency-resolved optical-gating measurements of ultrashort pulses," *J. Opt. Soc. Amer. B*, vol. 12, no. 10, pp. 1955–1967, 1995.

[5] B. Kohler, V. Yakovlev, K. Wilson, J. Squier, K. DeLong, and R. Trebino, "Phase and intensity characterization of femtosecond pulses from a chirped-pulse amplifier by frequency-resolved optical gating," *Opt. Lett.*, vol. 20, no. 5, pp. 483–485, 1995.

# APPENDIX A

## *Ambiguities in SHG-FROG*

The SHG-FROG geometry has a number ambiguities. By an ambiguity we mean that a certain change of the envelope $A(t)$ has no effect on the SHG-TROG trace and the algorithm could thus converge to this solution. The following ambiguities are present and can be easily verified upon substitution into (4.19).

A phase offset by $\varphi_0$

$$A(t) \rightarrow A(t)\exp(j\varphi_0) \tag{A.1}$$

A shift in time by $t_s$

$$A(t) \rightarrow A(t - t_s) \tag{A.2}$$

A complex mirror image of $A(t)$

$$A(t) \rightarrow A^*(-t) \tag{A.3}$$

The first two ambiguities are trivial and of no concern in ultra-short pulse measurements as they represent a constant phase offset and a delay in time. The third ambiguity reverses the direction of time for the pulse and it returns the wrong sign on the phase of the pulse. Due to the fact that there is no difference in the spectogram, the pulse reconstruction algorithm can converge to either $A(t)$ or $A^*(-t)$. There is no way to identify this ambiguity, not even by looking at the spectrum of the pulse as the spectrum that goes with $A^*(-t)$ is given by $\widetilde{A}^*(f)$. Only if one would know the spectral phase, it would be possible to distinguish whether the pulse reconstruction

algorithm has returned $A(t)$ or $A^*(-t)$. This information is however not available from a measurement of the intensity spectrum $\widetilde{I}(f) = |\widetilde{A}(f)|^2$. One way to eliminate this ambiguity in the direction of time and in the sign of the phase is by adding a known amount of dispersion to the pulse and remeasuring the SHG-FROG trace.

For completeness, we calculate the FROG trace $I'_{\text{SHG-FROG}}(F,T)$ that results from the transformations

$$A(t) \rightarrow A^*(t) \tag{A.4}$$

and

$$A(t) \rightarrow A(-t) \tag{A.5}$$

The FROG trace for both transformation can be shown to equal

$$\begin{aligned} \widetilde{I}'_{\text{SHG-FROG}}(F,T) &= \widetilde{I}_{\text{SHG-FROG}}(-F,T) \\ &= \widetilde{I}_{\text{SHG-FROG}}(-F,-T) \end{aligned} \tag{A.6}$$

where $\widetilde{I}_{\text{SHG-FROG}}(F,T)$ is the FROG trace that would be obtained for $A(t)$. In the last equality we have used the fact that the SHG-FROG trace is symmetric in $T$

$$\widetilde{I}_{\text{SHG-FROG}}(F,T) = \widetilde{I}_{\text{SHG-FROG}}(F,-T) \tag{A.7}$$

which can be easily verified.

The transformations of (A.4) and (A.5) thus lead to a TROG trace that is a flipped version in both the $T$ and $F$ direction of the TROG trace for $A(t)$. Due to the fact that these transformations lead to a different TROG trace, the algorithm will never converge to either $A^*(t)$ or $A(-t)$.

# APPENDIX B

## *Ambiguities in DP-TROG*

The DP-TROG geometry has a number ambiguities. By an ambiguity we mean that a certain change of the envelope $\widetilde{A}(f)$ has no effect on the DP-TROG trace and the algorithm could thus converge to this solution. The following ambiguities are present and can be easily verified upon substitution together with (5.20) into (5.19).

A phase offset by $\varphi_0$

$$\widetilde{A}(f) \rightarrow \widetilde{A}(f)\exp(j\varphi_0) \tag{B.1}$$

A shift in frequency by $f_s$

$$\widetilde{A}(f) \rightarrow \widetilde{A}(f - f_s) \tag{B.2}$$

A mirror image of $\widetilde{A}(f)$

$$\widetilde{A}(f) \rightarrow \widetilde{A}(-f) \tag{B.3}$$

The first two ambiguities are trivial and of no concern in ultra-short pulse measurements as they represent a constant phase offset and an effective shift of the carrier frequency $f_0$. The third ambiguity reverses the direction of time for the pulse upon inverse Fourier transformation. This ambiguity can however easily be identified by comparing the reconstructed intensity spectrum with the measured one. If one is the mirror image of the other, the algorithm retrieved $\widetilde{A}(-f)$ and $A(-t)$ and the pulse would have to be flipped in the time- and frequency-domain to obtain the correct one. So for the DP-TROG method there is no ambiguity in the direction of time in contrast to SHG-FROG.

For completeness, we calculate the TROG trace $I'_{\text{DP-TROG}}(T,F)$ that results from the transformations

$$\widetilde{A}(f) \rightarrow \widetilde{A}^*(f) \tag{B.4}$$

and

$$\widetilde{A}(f) \rightarrow \widetilde{A}^*(-f) \tag{B.5}$$

The TROG trace for both transformation can be shown to equal

$$\begin{aligned} I'_{\text{DP-TROG}}(T,F) &= I_{\text{DP-TROG}}(-T,F) \\ &= I_{\text{DP-TROG}}(T,-F) \end{aligned} \tag{B.6}$$

where $I_{\text{DP-TROG}}(T,F)$ is the TROG trace that would be obtained for $\widetilde{A}(f)$. In the last equality we have used the fact that the DP-TROG trace is centro-symmetric in $T$ and $F$

$$I_{\text{DP-TROG}}(T,F) = I_{\text{DP-TROG}}(-T,-F) \tag{B.7}$$

which can be easily verified.

The transformations of (B.4) and (B.5) thus lead to a TROG trace that is a flipped version in either the $T$ or $F$ direction of the TROG trace for $\widetilde{A}(f)$. Due to the fact that these transformations lead to a different TROG trace, the algorithm will never converge to either $\widetilde{A}^*(f)$ or $\widetilde{A}^*(-f)$.